Max-Planck-Institut für Meteorologie

MAX PLANCK GESELLSCHAFT

International Max Planck Research School on Earth System Modelling

Observations of Meso-scale Circulation and its Relationship with Cloudiness in the Tropics

Geet George

Hamburg 2021

Berichte zur Erdsystemforschung
Reports on Earth System Science

246
2021

Hinweis

Die Berichte zur Erdsystemforschung werden vom Max-Planck-Institut für Meteorologie in Hamburg in unregelmäßiger Abfolge herausgegeben.

Sie enthalten wissenschaftliche und technische Beiträge, inklusive Dissertationen.

Die Beiträge geben nicht notwendigerweise die Auffassung des Instituts wieder.

Die "Berichte zur Erdsystemforschung" führen die vorherigen Reihen "Reports" und "Examensarbeiten" weiter.

Notice

The Reports on Earth System Science are published by the Max Planck Institute for Meteorology in Hamburg. They appear in irregular intervals.

They contain scientific and technical contributions, including Ph. D. theses.

The Reports do not necessarily reflect the opinion of the Institute.

The "Reports on Earth System Science" continue the former "Reports" and "Examensarbeiten" of the Max Planck Institute.

Anschrift / Address

Max-Planck-Institut für Meteorologie
Bundesstrasse 53
20146 Hamburg
Deutschland

Tel./Phone: +49 (0)40 4 11 73 - 0
Fax: +49 (0)40 4 11 73 - 298

name.surname@mpimet.mpg.de
www.mpimet.mpg.de

Layout

Bettina Diallo and Norbert P. Noreiks
Communication

Copyright

Observations of Meso-scale Circulation and its Relationship with Cloudiness in the Tropics

Geet George

Hamburg 2021

Geet George
aus Ahmedabad, Indien

Max-Planck-Institut für Meteorologie
The International Max Planck Research School on Earth System Modelling
(IMPRS-ESM)
Bundesstrasse 53
20146 Hamburg

Tag der Disputation: 03. September 2021

Folgende Gutachter empfehlen die Annahme der Dissertation:
Prof. Dr. Bjorn Stevens
Prof. Dr. Felix Ament

Vorsitzender des Promotionsausschusses:
Prof. Dr. Dirk Gajewski

Dekan der MIN-Fakultät:
Prof. Dr. Heinrich Graener

Title Cover: Courtesy of Bjorn Stevens, photo was captured during the NARVAL2 campaign on flight RF07.

Thesis Template: developed by André Miede and Ivo Pletikosic available at: https://bitbucket.org/amiede/classicthesis/wiki/Home

Berichte zur Erdsystemforschung / Max-Planck-Institut für Meteorologie 246
Reports on Earth System Science / Max Planck Institute for Meteorology 2021

ISSN 1614-1199

Geet George

Observations of Meso-scale Circulation and its Relationship with Cloudiness in the Tropics

पुरखों ने यह बात बताई
उल्टा करके देख सके तो
अम्बर भी है गहरी खाई

- वरुण ग्रोवर
(मन कस्तूरी)

Purkho ne ye baat batai
Ulta kar ke dekh sakey to
Ambar bhi hai gehri khhai

- Varun Grover
(*Mann Kasturi*)

(loosely translated)

People of yore have told us
If you can reform your perspective
The sky becomes a bottomless abyss

ACKNOWLEDGMENTS

This dissertation owes a lot to the support and encouragement of many people. Before all the thanks though, I apologise in advance for any names that I missed out on.

Words fail me in expressing how amazingly Bjorn supported me throughout my PhD time as a brilliant supervisor and a very understanding friend at the same time. In the true sense of the word, he has been my *guru*. Despite in-person meetings being rare with Sandrine, interactions with her have always been a joy, wherein I learnt not only how to stimulate ideas but also how to express them. It is an absolute privilege to learn how to do science in such proximity to Bjorn and Sandrine. I am indebted to Marcus for his help, especially in the beginning of my PhD. He helped me not just with day-to-day questions about my research, but also with the technical aspects of data, analysis and programming. Although in no official capacity, but Raphaela has been like a guide to me. She is a great teacher and I have benefited immensely from her clarity of thought. Thanks also to Felix for being such a well-rounded panel chair, and making the panel meetings actually a joy to look forward to. I could not have asked for better people to guide me into the world of scientific research.

I thank all the Tropical Cloud Observations group members, in particular Lutz, Friedel & (though not officially a member) Heike, for all the support, and especially for helping me learn the practicalities that go behind organising a field campaign. Special thanks to Hauke & Tobi, who could easily have been so intimidating with their vast know-how on so many different matters, but it is to their credit that I always feel I can approach them with any silly query. Thanks to Anna Lea, Hauke & Theresa, with whom I felt I was in the same boat with my PhD and could share very thought-provoking discussions. Thanks also to Ann Kristin, Cathy (and her group), Claudia S., Felix A., Florian E., Hans, Jessica, Jiawei, Jule, Julia W., Kerry, Kevin W., Louise N., Marc, Marek, Nicolas, Robert P., Sabrina, Theresa L., Thibaut & Tobias B., for the discussions about and feedback on my work.

Thanks are also due to Antje, Connie and Michaela, without whose incredible support, my transition to and my stay in Hamburg would have been a complete mess. Massive thanks and a big hug to Angela – whom my mother very rightly recognises as my 'mother in Germany' – for the fun chats and for her unending support.

I was lucky to have a lovely office-mate in Katherine and an awesome roommate in Kerstin, both of whom were not just confined to these roles and are now two of my most cherished friends. Not enough thanks can be expressed to my dear friend Theresa for being such an absolute angel of a person. Thanks to David for being such a wonderful friend all along since almost my first day in Hamburg. The importance of sharing conversations, often over food & drinks, is not lost on me thanks to Pinhsin, Leonie, Diego, Laura, Zoe, Clara, Mateo & others. I owe a lot of my happiness (and maybe a few beers) during the PhD to friends like Elliot, Arjun, George, Kalrav, Kushal, Lukas, Rajvi, Sebastian, Suman & many many others. Thanks a tonne also to everyone in the football group. And a special thanks for all the remote support I got from friends like Sandeep & Sujit.

I cannot begin to express my thanks to everyone in my family (which also got officially extended a month ago), and especially to Pappa, Mummy and Vinu, whose unwavering support and love has been there for me every single day. Lastly, thank you Devanshi, for being there with me every step of the way. Your constant support and understanding and just the fact that you tolerate me is something I don't take for granted.

ABSTRACT

One of the seven Grand Challenges listed by the World Climate Research Programme is Clouds, Circulation and Climate Sensitivity which, as per them, is "a specific barrier preventing progress in a critical area of climate science". At the heart of this challenge lies the problem of feedback of marine low-level clouds to climate change, which arises mainly from a poor understanding of how clouds couple to circulation. This dissertation builds upon recent advances in measurements of atmospheric vertical motion to investigate through observations how circulation impacts cloudiness and to characterise circulation in the trade-wind regions, thus confronting the core of clouds-circulation coupling.

A long-standing lack of measurements of meso-scale circulation has been filled by two recent field campaigns in the northern tropical Atlantic – the *Next Generation Remote Sensing for Validation Studies* campaign (NARVAL2), which took place in August, 2016 and *ElUcidating the RolE of Cloud-Circulation Coupling in ClimAte* (EUREC^{4}A) field campaign, which took place in January-February, 2020. Both campaigns employed aircraft to launch dropsondes along a circular path, and estimate key circulation parameters such as area-averaged horizontal mass divergence ($\mathcal{D}$), vorticity (ζ) and subsidence rate (ω).

From NARVAL2, I analyse case-studies of co-located measurements of both ω and cloudiness. I show that at the meso scale, ω more effectively regulates shallow clouds' area fraction, liquid water path and rain water path, compared to cloud-controlling factors that are effective at the climate scale. For this, I use a simplistic mass-flux estimate and in the process, also reveal that the response of clouds to meso-scale circulation is non-linear. This has major implications on the current strategy of climate models to simulate clouds using large-scale parameters instead of ones at the meso scale.

I produce a dataset called *Joint dropsonde Observations of the Atmosphere in tropical North atlaNtic meso-scale Environments* (with the backronym JOANNE) out of the EUREC^{4}A dropsonde measurements. Courtesy of the extensive measurements, the dataset provides rich statistics of the meso-scale circulation parameters and thus, facilitates understanding the trade-wind atmosphere in terms of both thermodynamics and kinematics. JOANNE not only includes quality control of the data, but also data products which are synthesised for much easier use by the larger scientific community. The uniformly gridded data and the circle estimates of area-averaged quantities are especially proving to be helpful tools in studies that target shallow cumulus cloud processes and their interaction with the atmospheric variables.

Using the estimates of area-averaged quantities from the JOANNE dataset, I describe the meso-scale circulation in the trades. This addresses a critical gap in current knowledge, because the lack of observations had rendered the nature of atmospheric meso-scale circulation unknown. I describe the mean vertical structure of $\mathcal{D}$, ζ and ω and the variability in these parameters across days as well as within a few hours. Moreover, I propose a shallow-circulation mechanism whose persistence in the trades explains a negative association observed between the mean sub-cloud and cloud $\mathcal{D}$ anomalies, as well as the influence of $\mathcal{D}$ on other parameters such as humidity and temperature.

Thus, gaining from the measurements of the NARVAL2 and EUREC^{4}A field campaigns, this dissertation not only describes the nature of meso-scale circulation and how it influences clouds, but also opens pathways for future investigations of clouds-circulation coupling.

ZUSAMMENFASSUNG

Eine der sieben großen Herausforderungen (Grand Challenges), die das Weltklimaforschungsprogramm benennt, ist das Thema Wolken, Zirkulation und Klimasensitivität (Clouds, Circulation and Climate Sensitivity). Es heißt, dass dieses Thema "eine spezifische Barriere darstellt, die den Fortschritt in einem kritischen Bereich der Klimawissenschaft verhindert". Im Kern dieser Herausforderung liegt das Problem der Rückkopplung von marinen flachen Cumuluswolken auf ein verändertes Klima, welches sich hauptsächlich aus einem mangelnden Verständnis der Kopplung von jenen Wolken mit der Zirkulation ergibt. Diese Dissertation baut auf den jüngsten Fortschritten in der Messung der atmosphärischen Vertikalbewegung auf. Basierend auf Beobachtungen wird der Einfluss der Zirkulation auf die Bewölkung untersucht und die Zirkulation in den Passatwindregion charakterisiert, um sich so dem Kern der Kopplung von Wolken und Zirkulation zu nähern.

Ein langjähriger Mangel an Messungen der mesoskaligen Zirkulation wurde durch zwei kürzlich durchgeführte Feldmesskampagnen im nördlichen tropischen Atlantik behoben - die *Next Generation Remote Sensing for Validation Studies*-Kampagne (NARVAL2), welche im August 2016 statt fand und die *ElUcidating the RolE of Cloud-Circulation Coupling in ClimAte* (EUREC^{4}A) Kampagne, die im Januar-Februar 2020 statt fand. Bei beiden Kampagnen wurden Flugzeuge eingesetzt, um Dropsonden entlang einer Kreisbahn zu starten und wichtige Zirkulationsparameter wie die flächengemittelte horizontale Massendivergenz ($\mathcal{D}$), die Wirbelstärke (ζ) und die Absinkrate (ω) zu bestimmen.

Anhand von NARVAL2 Daten analysiere ich in Fallstudien kombinierte Messungen von ω und Bewölkung. Ich zeige, dass ω auf der Mesoskala den Flächenanteil der flachen Wolken und deren Flüssigwasserpfad und Regenwasserpfad effektiver reguliert als Einflussfaktoren auf Wolken, die auf der Klimaskala wirksam sind. Dazu verwende ich eine vereinfachte Schätzung des Massenflusses und zeige dabei auch, dass die Reaktion der Wolken auf die mesoskalige Zirkulation nichtlinear ist. Letzteres hat große Auswirkungen auf die derzeitige Strategie der Klimamodelle, welche Wolken mit großskaligen Parametern simulieren statt mit jenen auf der Mesoskala.

Ich erstelle einen Datensatz namens *Joint dropsonde Observations of the Atmosphere in tropical North atlaNtic meso-scale Environments* (mit dem Backronym JOANNE) aus den EUREC^{4}A-Dropsondenmessungen. Dank der umfangreichen Messungen liefert der Datensatz reichhaltige Statistiken der mesoskaligen Zirkulationsparameter und erleichtert so das Verständnis der Passatwindatmosphäre sowohl in Bezug auf die Thermodynamik als auch auf die Kinematik. JOANNE umfasst nicht nur die Qualitätskontrolle der Daten, sondern auch synthetisiert Datenprodukte für eine einfachere Nutzung durch die größere wissenschaftliche Gemeinschaft. Die Daten auf einheitlichem Gitter und auch die flächengemittelten Größen auf der Kreis-Skala erweisen sich als besonders hilfreiche Werkzeuge bei Studien, die auf Prozesse der flachen Cumuluswolken und deren Wechselwirkung mit den atmosphärischen Variablen abzielen.

Unter Verwendung der flächengemittelten Größen aus dem JOANNE-Datensatz beschreibe ich die mesoskalige Zirkulation in der Passatwindregion. Dies schließt eine kritische Lücke im derzeitigen Wissen, da die Natur der atmosphärischen mesoskaligen Zirkulation aufgrund fehlender Beobachtungen bisher unbekannt war. Ich beschreibe die mittlere vertikale Struktur von $\mathcal{D}$, ζ und ω und die Variabilität dieser Parameter sowohl

über mehrere Tage hinweg als auch innerhalb weniger Stunden. Darüber hinaus schlage ich einen Mechanismus zur Beschreibung der flachen Zirkulation vor. Dieser Mechanismus ist vorherrschend in der Passatwindregion und erklärt eine beobachtete negative Korrelation zwischen den mittleren $\mathcal{D}$ Anomalien in der bodennahen Grenzschicht und in der darüber liegenden Wolkenschicht. Weiterhin erklärt der Mechnismus den Einfluss von $\mathcal{D}$ auf weitere Parameter wie Feuchtigkeit und Temperatur.

Ausgehend von den Messungen der Feldkampagnen NARVAL2 und EUREC^{4}A beschreibt diese Dissertation nicht nur die Natur der mesoskaligen Zirkulation und deren Einfluss auf die Wolken, sondern eröffnet auch Wege für zukünftige Erforschung der Kopplung von Wolken und Zirkulation.

PUBLICATIONS RELATED TO THIS DISSERTATION

Appendix A:

George, Geet, Bjorn Stevens, Sandrine Bony, Robert Pincus, Chris Fairall, Hauke Schulz, Tobias Kölling, Quinn T. Kalen, Marcus Klingebiel, Heike Konow, Ashley Lundry, Marc Prange, and Jule Radtke. (2021). "JOANNE : Joint dropsonde Observations of the Atmosphere in tropical North atlaNtic meso-scale Environments". *Earth Syst. Sci. Data Discuss.* [preprint], in review, doi:10.5194/essd-2021-162

Appendix B:

George, Geet, Bjorn Stevens, Sandrine Bony, Marcus Klingebiel, and Raphaela Vogel. (2021). "Observed impact of meso-scale vertical motion on cloudiness". *Journal of the Atmospheric Sciences*. doi:10.1175/JAS-D-20-0335.1.

Appendix C:

George, Geet, Bjorn Stevens, Sandrine Bony and Raphaela Vogel. (2021). "Mesoscale circulation : Structure, variability and interplay with other environmental factors". (*in preparation*)

PREFACE

The main part of this dissertation is a unifying essay which provides an overview of the three studies that form this cumulative thesis. The studies are added as appendices.

All three studies come out of measurements taken from two field campaigns that took place in the tropical north Atlantic – NARVAL2[1] and EUREC^{4}A. The first study (Appendix A) describes a dataset of dropsonde measurements which contain a rich sampling of trade-wind atmospheric variables including, importantly, measurements of mesoscale circulation. The second study (Appendix B) uses colocated measurements of cloudiness and atmospheric vertical motion to investigate the influence of circulation on clouds at the mesoscale. The third study (Appendix C) characterises the properties of mesoscale circulation in the trade-wind regions by describing the mean vertical structure and the variability of quantities such as horizontal divergence and vertical velocity. The sequence of the first two studies here are swapped from how they were carried out chronologically, so as to provide the reader first with information about how measurements of the vertical motion are made.

In the unifying essay, I start with providing background on the clouds-circulation problem and list my research questions. Then, I summarise the three studies and place them in the overarching theme of the dissertation, i.e. the observations of circulation and its influence on clouds. At the end, I give the major implications of the studies and how they fit into the larger picture of understanding the clouds-circulation problem. To do this, I use the results of the studies and answer the research questions posed in the beginning of the essay.

[1] Acronyms for field campaigns and instruments are usually more familiar terms than their long forms. Therefore, to smoothen the flow of reading, all field campaign and instrument name acronyms are introduced in a separate list following this preface instead of at their first mentions in the text. A couple of model names and products are also part of the list.

ACRONYMS

ACTIVATE . . . . . Aerosol Cloud Meteorology Interactions over the Western Atlantic Experiment

AFLUX . . . . . Arctic Amplification: Fluxes in the Cloudy Atmospheric Boundary Layer

ASPEN . . . . . Atmospheric Sounding Processing Environment

ATEX . . . . . Atlantic Tradewind Experiment

AVAPS . . . . . Airborne Vertical Atmospheric Profiling System

BCO . . . . . Barbados Cloud Observatory

BOMEX . . . . . Barbados Oceanographic and Meteorological Experiment

DYAMOND-Winter . Second phase of the Dynamics of the Atmospheric General Circulation Modeled On Non-hydrostatic Domains

ECMWF . . . . . European Centre for Medium-Range Weather Forecasts

ERA5 . . . . . Fifth-generation ECMWF Atmospheric Reanalysis

EUREC^{4}A . . . . . Elucidating the Role of Clouds–Circulation Coupling in Climate

GATE . . . . . GARP (Global Atmospheric Research Program) Atlantic Tropical Experiment

GOES-13 . . . . . Geostationary Operational Environmental Satellite Program - 13

HALO . . . . . High-Altitude and Long Range

HALO-(AC)^3 . . . . . HALO Arctic Amplification: Climate relevant atmospheric and surface processes and feedback mechanisms

HAMP . . . . . HALO Microwave Package

IFS . . . . . Integrated Forecasting System

NARVAL2 . . . . . Second Next Generation Remote Sensing for Validation Studies

RICO . . . . . Rain in Cumulus over the Ocean

TOGA-COARE . . . . Tropical Ocean-Global Atmosphere (TOGA) Coupled Ocean Atmosphere Response Experiment

WALES . . . . . Water-vapor Lidar Experiment in Space

WP-3D . . . . . Lockheed WP-3D Orion (N43RF / "Miss Piggy")

CONTENTS

Part I

UNIFYING ESSAY

1

BACKGROUND

An experiment is a question which science poses to Nature, and a measurement is the recording of Nature's answer.

- Max Planck (1949)

1.1 CLOUDS-CIRCULATION COUPLING

Clouds can be perceived as the visual embodiment of the circulation[1] of the atmosphere. This seems especially obvious when the global distribution of clouds is viewed through satellite imagery, such as in Fig. 1.1a. The circulation of the tropical atmosphere is dictated by the Hadley cell, and can be described briefly as mean, ascending motion of air near the thermal equator and relatively larger adjacent regions experiencing a compensating subsidence. A schematic is shown in Fig. 1.1b. Clouds are deeper in the ascending branch of the Hadley cell and often reach the top of the tropopause, whereas much shallower clouds like cumuli and stratocumuli are observed in the subsiding branch. Just outside the tropics, the subsidence can sometimes be strong enough to maintain climatological high pressure regions, thus completely preventing cloud formation. This association of clouds, and subsequently precipitation, with the Hadley cell is the reason why rainforests are persistent near equatorial latitudes and major deserts are located at the edge of the sub-tropics.

Before going further, I define the terms *meso scale* and *large scale*, as they will be appearing frequently in the text. The meso scale can be thought of as the timescale of the evolution of clouds themselves, whereas the large scale is the timescale thought to be relevant for determining the mean, synoptic environmental state and thus controls the climatology of clouds. Environmental conditions in the meso scale (20-200 km) can change within a few hours to a day, whereas over the large-scale ($O(1000)$ km), conditions can be expected to persist from a few days to over a month. Although the term 'environment' (or 'atmospheric state') is generally inclusive of clouds, I use the term here to mean the surroundings inhabited by clouds and the atmospheric conditions that shape the clouds.

Clouds are integral participants in shaping the climate, because of their interaction with radiation in both the longwave and shortwave spectra. However in terms of feedback, i.e. their response to a warming climate, clouds are still a major source of uncertainty (Zelinka et al., 2020). Particularly important in this respect are marine, low-level clouds such as shallow cumuli found in the trade-wind regions. This is because of their relative abundance on the planet, as well as current climate models' inability to arrive at robust estimates of their feedbacks (Vial et al., 2016).

In addition to the clouds-circulation coupling at the planetary scale discussed in the beginning, the coupling of these low-level clouds with circulation at large and meso scales is also important for cloud feedbacks (Bony et al., 2015). The interplay between clouds and circulation is therefore crucial to improving our understanding of the climate in its

[1] In this dissertation, I use circulation as a blanket term to mean the kinematic parameters of the atmosphere, especially the vertical motion and terms associated with it.

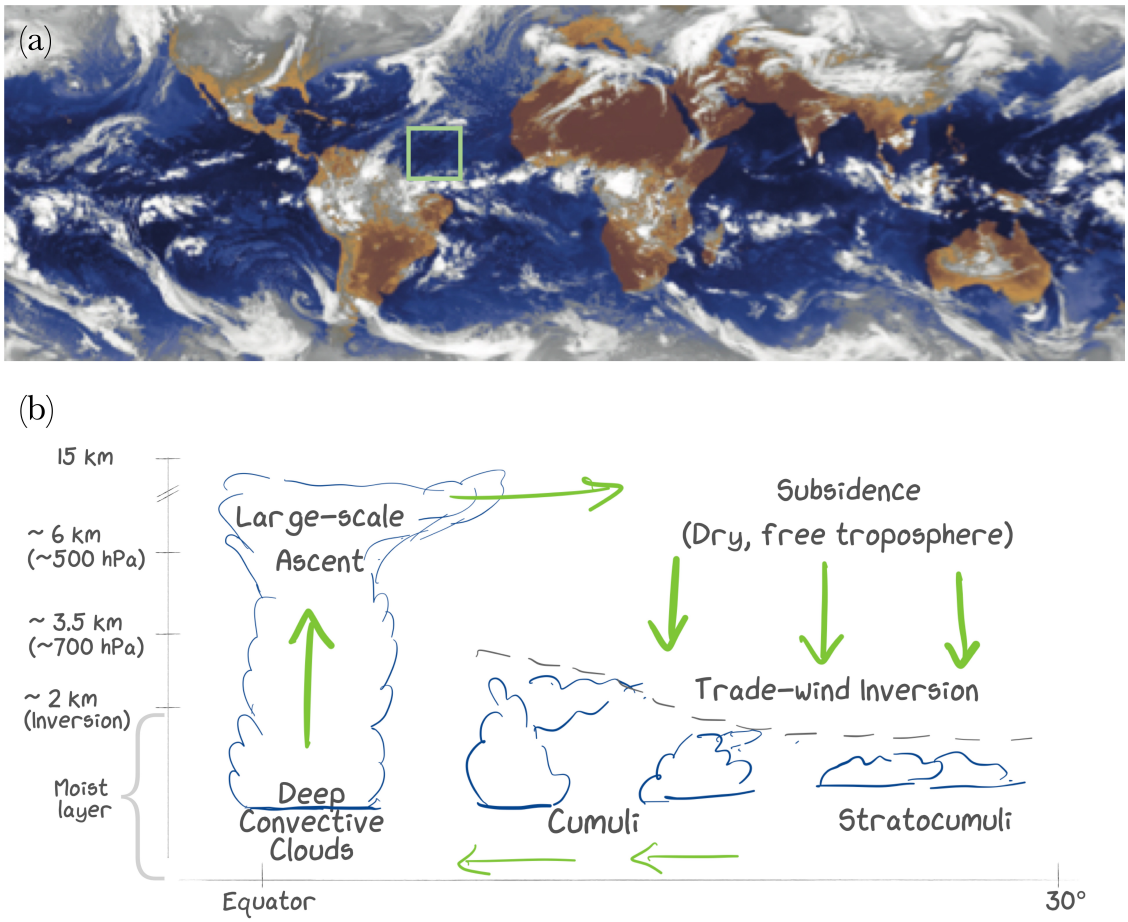

Figure 1.1: (a) Infrared composite of geostationary satellite data taken on March 29th 2004 at 12:00 GMT, inspired by Bony et al. (2015) and is courtesy of Météo-France/CMS/SATMOS/Lannion. The overlain green box shows the north Atlantic trade-wind region – the area in focus for this dissertation and (b) A not-to-scale schematic view of the atmospheric circulation in the tropics and the often-occuring cloud types in the regimes is shown. Some important processes, precipitation among them, have been excluded in the schematic.

present form as well as for models to predict future climate scenarios more accurately. However, an accurate coupling of clouds to circulation is an important missing piece of the puzzle in current models (Stevens and Bony, 2013).

1.1.1 *Current reliance on large scale parameters*

Previous studies, owing to observational challenges, have relied on reanalysis products to study the link between clouds and circulation. Due to reanalysis products being more reliable over the large scale, such studies have focused on the environment's control of clouds at the large scale (e. g. Bony et al., 2004; Stevens et al., 2007; Myers and Norris, 2013, among others). Conventionally accepted cloud-controlling factors that we are confident of (e.g. Klein et al., 2017) are also ones that are applicable on the large-scale, such as lower tropospheric stability (Klein and Hartmann, 1993), sea surface temperature (Qu et al., 2015), relative humidity (Slingo, 1980), and others.

Therefore, it is no surprise, that current climate models (typically general circulation models or GCMs) currently predict cloudiness in the tropics using relationships that are only known at the large scale, e.g. by using values of subsidence (ω) at 500 hPa (ω_{500}) to separate shallow from deep convection. Negative values of ω indicate rising motion. Models thus simulate deep convection for regions with negative ω_{500}, and conversely, simulate shallow clouds for regions with positive values. ω_{500} has consistently been shown as a reliable parameter for this purpose in the past decades (Slingo, 1987; Bony et al., 2004; Myers and Norris, 2013). Additional constraints from another large-scale parameter, atmospheric stability, is further used to distinguish between shallow-cloud regimes of cumulus and stratocumulus (Medeiros and Stevens, 2009). Thus, large-scale parameters such as ω and stability dictate important aspects of cloudiness in current climate models.

1.1.2 *The need to understand meso-scale circulation*

Observations show that more than 50% and 75% of the variability in shallow clouds occur over time scales of 1 and 5 days, respectively (Nuijens et al., 2015b), thus highlighting the importance of the meso scale. However, what controls tropical clouds at the meso scale is not as well-investigated as that at the large scale. For the large-scale we have answers about how clouds are linked to some aspects of circulation, but none at the meso scale. This is due to there not being enough understanding about the state of atmospheric circulation at the meso scale, which in turn can be blamed on the lack of observations.

Klein (1997) and Brueck et al. (2015) show that the relationships observed at the large scale often do not hold over scales of 5-days or shorter. Moreover observations show that whilst factors such as humidity, stability and ω_{850} explain ~56% of the monthly variance in trade-wind cloud cover, the same factors fail to explain any more than 24% of the daily variance (Nuijens et al., 2015a). Thus, large scale parameters are not capable of sufficiently representing cloudiness at the meso scale, which is also roughly the same scale as the grid-box sizes of climate models today.

The reliance on large scale cloud-environment relationships also points to an inherent assumption in climate models' parameterisation of clouds – that the effects of the meso-scale perturbations should average out over the large scale. However, this assumption is only valid if the response of clouds to meso-scale conditions is linear. We do not know if this response is linear, primarily because we do not know the nature of the meso-scale circulation and therefore, we do not know how clouds respond to it.

Limited-area models that do not resolve the global circulation, such as large eddy simulations (LES) and some cloud-resolving models (CRMs), need the vertical motion profile to be prescribed as part of the forcing to the model. Such models show that clouds are very sensitive to the prescribed circulation (Bony et al., 2015; Dussen et al., 2016). Currently, models use forcings that are either not constrained by any observations (Sobel and Bretherton, 2000; Romps, 2012) or if they use observations, then they are large-scale estimates and not really reflective of the conditions at the meso scale, e.g. TOGA-COARE forcings from Johnson et al. (2002) and RICO forcings from VanZanten et al. (2011). Thus, along with how circulation couples to clouds, it is also important to know the meso scale structure and variability of circulation itself.

1.2 MEASURING VERTICAL MOTION

There has been a long standing agreement in literature that the role of ω in cloud prediction is not negligible (e.g. Yanai et al., 1973; Bony et al., 2004; Brueck et al., 2015).However, measuring the meso-scale circulation is very difficult. Thus, ω has thus always been in the game, but never really in the grasp.

Early attempts to compute area-averaged vertical motion of the atmosphere were with field campaigns in the Atlantic trade-wind regions such as the Atlantic Expedition of 1965 , ATEX in 1969 (Augstein et al., 1974) and BOMEX in 1969 (Holland, 1970). These field campaigns deployed large-scale networks of research vessels, and via simultaneous radiosonde soundings from these platforms, computed the horizontal divergence ($\mathcal{D}$) and thus, the mass, heat and moisture budgets at several levels in the atmosphere. Later, several other campaigns such as GATE and TOGA-COARE also successfully implemented similar sounding arrays to compute the divergence and vertical motion over large-scale areas, with dimensions ranging between 800 $-$1000 km. Lenschow et al. (1999, 2007), although not the first to demonstrate, solidified the use of airplane measurements to measure area-averaged divergence ($\mathcal{D}$) using the line-integral and regression method. The advantage here was that the spatial scale could be made smaller than in previous field campaigns; however, information about vertical motion was missing, because $\mathcal{D}$ was only estimated at one level.

Overcoming the limitation of aircraft to sample a single level in the atmosphere, Bony and Stevens (2019) recently used dropsondes launched along a circular path of roughly 180 km diameter to estimate area-averaged horizontal mass divergence and, consequently, vertical motion in a field campaign called NARVAL2 (details of the method and the field campaign in Section 2). They demonstrated the robustness of the method by making repeated measurements in the same airmass, and found that estimates of the divergence profile thus computed showed robust area-averaged signals rather than noise. The repetition also allowed them to experimentally check if the regression error is consistent with the measurement error. The major breakthrough of Bony and Stevens (2019) was indeed the measurements of ω at the meso scale. However, their use of the regression method provides the added advantage that an estimate of the standard error of regression is also available, thus letting us know what the confidence in these measurements of ω are.

1.3 RESEARCH QUESTIONS

Following Bony and Stevens (2019) area-averaged, meso-scale measurements of horizontal mass divergence ($\mathcal{D}$) and subsidence rate (ω) are now possible and available thanks to field campaigns such as NARVAL2 and EUREC^{4}A (both described in Section 2). Improving the current understanding of clouds-circulation coupling at the meso scale can thus be targeted via two approaches:

(a) the study of relationships that are apparent in observations by using colocated measurements of clouds and circulation

(b) the study of simulated relationships of clouds with circulation, by providing accurate forcings of the meso-scale circulation to LES and CRMs

However, we do not currently have accurate forcings because, as discussed in section 1.1.2, we do not know what the atmospheric circulation looks like in the meso scale.

Therefore, for approach (b) a pre-requisite needs to be met, i.e. first, a characterisation of the meso scale circulation is needed in terms of its mean vertical structure and variability. Approach (a) and the pre-requisite for approach (b) form the basis of this dissertation. The research questions are listed more explicitly with the relevant sub-questions as follows.

1. **Given the state of the atmosphere in the meso scale, what can be said about the cloudiness?**
    a) How well do conventional cloud-controlling factors perform in predicting cloudiness at the meso scale?
    b) What is the influence of meso-scale vertical motion on clouds?
    c) Could extending meso-scale relationships to the large scale potentially affect cloud and climate processes, i.e. Can we comment on the linearity of the cloud response to meso-scale conditions?
2. **What are the characteristics of the meso-scale circulation?**
    a) What is the mean vertical structure?
    b) What is the variability in the circulation parameters and how does this compare with that of thermodynamic quantities on the meso scale?
    c) What is the interplay between the meso-scale circulation and other environmental quantities thought to influence cloudiness?

2

MEASUREMENTS OF VERTICAL MOTION

I have still another concern. How are younger, less known, less well-funded meteorologists going to obtain access to the data?

- Joanne Simpson (1976)
(writing about data collected during the GATE field experiment)

2.1 DROPSONDES TO DESCRIBE THE STATE OF THE ATMOSPHERE

2.1.1 *The instrument*

Measurements from dropsondes are at the core of all three studies that form this dissertation and therefore, the instrument warrants a detailed introduction. Dropsondes hold sensors for measurement of pressure (p), temperature (T), relative humidity (RH) and Global Positioning System (GPS) signals, from which horizontal winds are derived. Thus, a dropsonde sounding provides fundamental quantities for describing the state of the atmosphere. After dropsondes are launched from an aircraft, they slowly sink down through the atmosphere with an open parachute, and on their way provide the aforementioned measurements. Dropsondes are essentially the same as radiosondes, except the former come down to Earth's surface after being released from an aircraft and the latter rise up through the atmosphere, while attached to a weather balloon. The studies in this dissertation benefit from Vaisala's RD-92 (for NARVAL2) and RD-41 (for EUREC^{4}A) dropsondes. The details about the sensors on the dropsondes are available in Table A.1.

Despite the lack of information about condensates, essential thermodynamic quantities such as density, geopotential height, measures of stability and column water vapour can be derived from the dropsonde measurements. Additionally, the high sampling rate of the dropsondes also resolves the vertical gradients in the atmosphere, that are often missed by remote-sensing instruments (Stevens et al., 2017). These vertical gradients help derive important features of the atmosphere's vertical structure such as the mixed layer depth and the inversion layer. Dropsondes thus provide important in-situ measurements for the characterisation of the atmospheric environment.

2.1.2 *Measuring vertical motion*

Individual dropsonde soundings provide local horizontal wind measurements from the GPS tracking of the sondes. However, vertical wind measurements – which are a few orders of magnitude lower than horizontal wind values – cannot be estimated reliably from individual soundings.

Bony and Stevens (2019) demonstrated the method of regression to obtain area-averaged estimates of divergence and vorticity, by launching dropsondes in circular paths of diameter ∼200 km. We simply refer to such dropsonde-circles as circles hereafter. If time-steadiness over roughly the period of one hour and linearity in horizontal space are

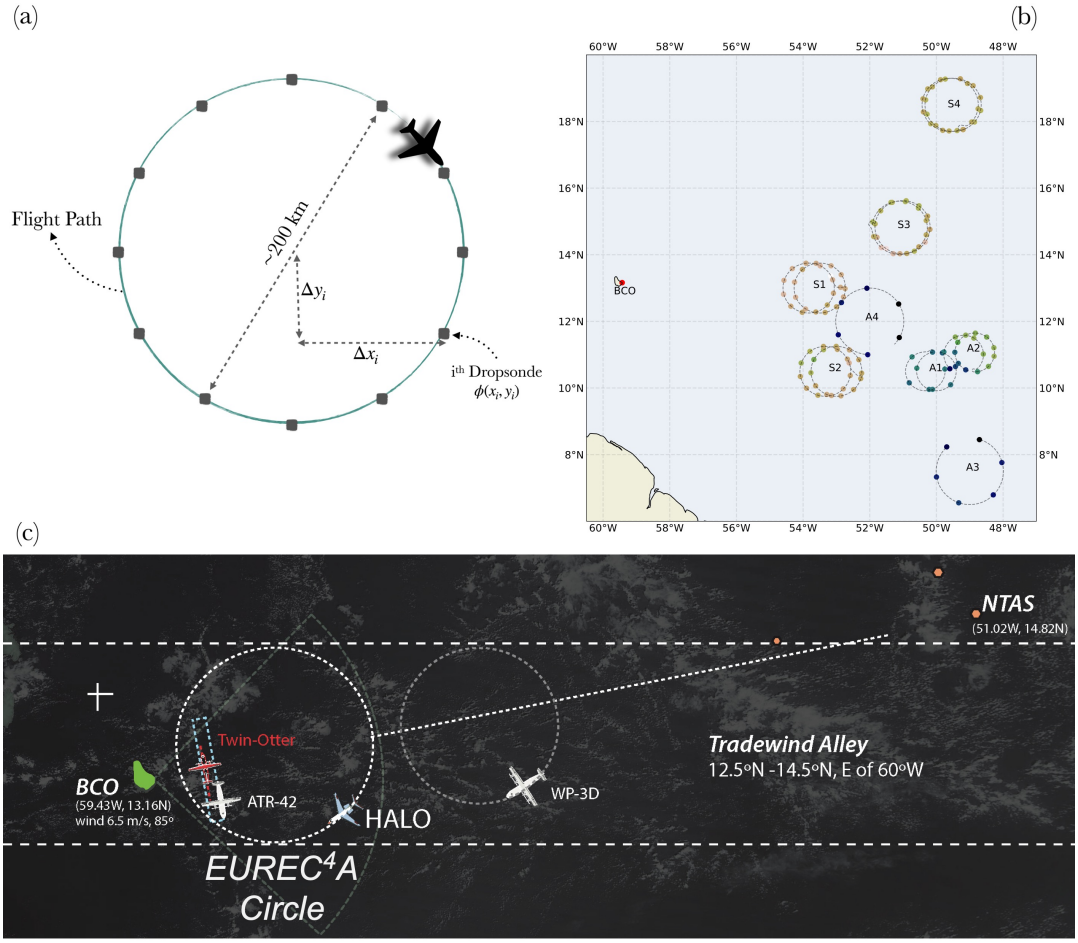

Figure 2.1: (a) Schematic of dropsonde measurements taken across a circular flight path, (b) Location of dropsonde launches made during NARVAL2 and (c) Schematic showing the area of aircraft operations during EUREC^{4}A. HALO is shown along with other participant aircraft.

assumed, the measurement of any parameter ϕ taken at position (x_i, y_i) can be related to the area-averaged mean of ϕ as,

$$\phi(x_i, y_i) \approx \phi_o + \frac{\partial \phi}{\partial x}\Delta x_i + \frac{\partial \phi}{\partial y}\Delta y_i, \tag{2.1}$$

where ϕ_o is the meso-scale mean value, and Δx_i and Δy_i are the eastward and northward distances, respectively of the i^{th} dropsonde from the mean center-point of all observed points included in the regression (see Fig. 2.1a). Equation 2.1 is solved for the system of all dropsondes launched in the circle such that the least-squared errors for the fit are minimised. This provides the regression coefficients, i.e. the horizontal gradients in the eastward ($\frac{\partial \phi}{\partial x}$) and northward ($\frac{\partial \phi}{\partial y}$) direction, along with the intercept value, i.e. the mean meso-scale value (ϕ_o).

Using gradients obtained from equation 2.1, the meso-scale divergence ($\mathcal{D}$) and vorticity (ζ) can thus be estimated as,

$$\mathcal{D} = \frac{\partial u}{\partial x} + \frac{\partial v}{\partial y} \quad \text{and} \quad \zeta = \frac{\partial v}{\partial x} - \frac{\partial u}{\partial y} \tag{2.2}$$

where u and v are the eastward and northward components of the horizontal wind, respectively. Thus, from continuity, it becomes possible to estimate the area-averaged vertical velocity as,

$$W(z) = -\int_0^z \mathcal{D} dz \tag{2.3}$$

and subsequently, subsidence (or pressure velocity) can be estimated as,

$$\omega(z) = -\rho(z) \cdot g \cdot W(z), \tag{2.4}$$

where ρ is density, g is the gravitational acceleration.

These circle measurements of $\mathcal{D}$ and ω were first successfully demonstrated at the meso scale by Bony and Stevens (2019) during the NARVAL2 campaign, and then, implemented extensively during the EUREC^{4}A campaign.

2.2 THE FIELD CAMPAIGNS AND THEIR CIRCLES

2.2.1 *HALO*

The German HALO aircraft, described aptly as an airborne "cloud observatory" by Stevens et al. (2019a), was integral to measurements in both field campaigns NARVAL2 and EUREC^{4}A. The aircraft served as a platform for making cloud measurements from advanced remote-sensing instruments and for launching dropsondes, thus simultaneously quantifying cloudiness and measuring the state of the atmosphere.

The positioning and configuration of instruments aboard HALO is shown in Fig. 2.2a. Dropsondes are first initialised by connecting them to the AVAPS computer (see Fig. 2.2b) at the rear side of the aircraft, and after successful initialisation, they are launched out of the aircraft from a pneumatic launch chute (see Fig. 2.2c), which forces the sonde out of the aircraft due to the difference in cabin and ambient pressure. Details about the other instruments on board HALO are provided by Stevens et al. (2019a) and references therein.

2.2.2 *NARVAL2 Campaign*

The field campaign NARVAL2 was carried out from August 8 −28 , 2016. The campaign primarily involved ten research flights across the tropical north Atlantic region east of Barbados, of which four flights included circles (diameter ∼180 −200 km), in line with the strategy explained in section 2.1.2. Each flight had two circles, and the launch locations of the dropsondes along these eight circles are shown in Fig. 2.1b. The circles typically consisted of circle pairs, i.e. once flown clockwise and then the second flown anti-clockwise in the 'same' location as the first, but shifted to account for the mean wind. The idea behind this flight strategy was to test the measurements within the same airmass. More details about the flights are provided by Stevens et al. (2019a).

2.2.3 *EUREC^{4}A Campaign*

During my time as doctoral student, I had the immense privilege of participating in EUREC^{4}A and was primarily responsible for the dropsonde operations aboard HALO.

Figure 2.2: (a) Figure from Stevens et al. (2019a), showing the setup of instruments aboard HALO for the NARVAL2 and EUREC^{4}A field campaigns, in addition to HALO's default configuration. The thermal imager was available only for EUREC^{4}A. (b) Photograph taken during a dropsonde's initialisation a few minutes before its launch. The unpacked dropsonde is connected to the AVAPS computer whose screen is seen above the dropsonde rack and (c) Photograph of the pneumatic launch-chute located on the starboard side of HALO, oriented downwards and facing away from the fuselage. Photographs (b) and (c) were taken during EUREC^{4}A flight HALO-126 and are from Konow et al. (2021).

EUREC^{4}A was a field experiment focused on understanding shallow cumulus cloud processes and their environment with a multitude of land-based, sea-based and airborne platforms in the north Atlantic trade-wind region over January-February, 2020 (Bony et al., 2017; Stevens et al., 2021).

A total of 1216 dropsondes were launched from HALO and the US-American WP-3D aircraft during EUREC^{4}A over 26 flights. The campaign employed the circle strategy as its core activity, and roughly 85% of the total sondes were launched in one of the 85 circles flown during EUREC^{4}A. Of these 85 circles, HALO flew 70 circles of ~222 km diameter with fixed center coordinates (57.67°W, 13.31°N), to facilitate synergy with other platforms in the campaign. We call these circles EUREC^{4}A-circles. Fig. 2.1c shows a schematic of the EUREC^{4}A strategy for measurements with participant aircraft. HALO is shown flying the EUREC^{4}A-circle just upwind of the Barbados Cloud Observatory (BCO; Stevens et al., 2016).

A typical HALO flight consisted of 6 circles per flight, usually arranged with an excursion of one hour between two sets of 3 circles, and flown at an altitude of ∼9.5 km. From that altitude, it took around 12 minutes for a dropsonde to land. Considering a mean easterly wind of ∼8 m/s, the air mass sampled by HALO would move from the eastern boundary to the western boundary (diameter ∼222 km) in roughly 8 hours. Thus, with 6 circles spread across 7-8 hours over 13 flight-days, it becomes possible to study the intra- and inter-day variability of the environmental parameters.

For both NARVAL2 and EUREC^{4}A, it took roughly 55 minutes to an hour for HALO to complete one circle, and dropsondes were launched at regular intervals of every 4-5 minutes. Therefore the cloudiness and environments characterised by these circles are representative of conditions over time-scales of 1-2 hours. The diameter of the circles in both campaigns also fall within the 160-220 km range, and therefore, with respect to both the time and space dimension, the circles fit our objectives of characterizing the meso scale suitably (see definition of meso scale in section 1.1). For reference, the circles fall into the ∼20-200 range or the *meso-β* scale, as per Orlanski (1975).

2.3 JOANNE

EUREC^{4}A's rich dropsonde measurements and in particular, the circles, present a unique opportunity for the meso-scale trade-wind conditions to be studied in a statistical manner, and at a scale on which observations were not available previously. Thus, a quality-controlled, uniformly gridded dataset with circle products such as $\mathcal{D}$ and ω can be immensely useful for the research community. With these objectives in mind, the EUREC^{4}A dropsondes dataset was made available. The dataset is called *Joint dropsonde Observations of the Atmosphere in tropical North atlaNtic meso-scale Environments*, and has the backronym JOANNE, as an ode to one of the most influential researchers in the field of tropical meteorology, Joanne Simpson.

An overview schematic of the data levels and the processes involved in JOANNE is shown as a flowchart in Fig. 2.3. A more detailed description of the dataset is available in the publication added as Appendix A. In this essay, I only touch upon the quality control, the dry bias encountered in HALO sondes and a brief description of the different data products that are part of JOANNE.

2.3.1 *Quality control*

Dropsonde data are collected on the aircraft using the AVAPS system (UCAR/NCAR, 1993) system, which receives the radio signals transmitted from in-flight dropsondes. These raw data are processed using the state-of-the-art software ASPEN (Martin and Suhr, 2021) and provides sounding data after applying standard quality-control algorithms and corrections. More details about the ASPEN processing and the primary data processing it performs can be found in Martin and Suhr (2021).

After processing raw data with ASPEN, I apply an additional round of quality-control (QC) to the data. A key objective of this QC is to provide data that do not contain any obviously erroneous measurements with regard to the conditions expected in the trade-wind regions. I also aim to keep missing data to a minimum in the dataset, to have more efficiency and minimise troubleshooting during data analyses.

With these objectives in mind, I devised three QC tests. Every sounding passes through these tests and its performance in each of the tests is collectively recorded in a parameter

called the *qc_flag*, which decides the sounding's success or failure in the QC process. The possible values for *qc_flag* are *good*, *bad* and *ugly*, which stand for fully-usable, non-usable and partially-usable data, respectively. The three QC tests are briefly described below:

1. Launch Detection Test: Most dropsonde instrument failures during EUREC^{4}A were due to a fault in their automatic detection of launch. This test looks for such failures in soundings and removes them.

2. Profile Fullness Test: This test checks if data is available for at least 80 % of the measured profile.

3. Low-altitude Measurements Test: This test checks if data in the moist layer falls within the expected bounds of the respective parameter's values.

Details about how the collective performance in these tests decides the *qc_flag* for a sounding is provided in the study in Appendix A.

Overall, 1067 sondes passed the QC tests and were flagged *good*, while 41 were flagged *bad* and provided no data. An additional 98 contained partial data and were flagged *ugly*, i.e. even though they are not included in JOANNE from Level-2 onwards, there are still measurements for some parameters or for some parts of the atmospheric profile that can be salvaged.

2.3.2 *Dry bias in HALO Dropsondes*

An advantage of the EUREC^{4}A campaign is the abundance of measurements from different platforms of several atmospheric quantities, among which water vapour is an important one. Although not exactly colocated, the proximity of these different measurements in space and time makes it possible to make reasonable comparisons and also create synergistic products. One such comparison of relative humidity (RH) from HALO dropsondes with measurements in the vicinity revealed a potential dry bias in the HALO soundings, i.e. RH values from HALO sondes were underestimated. After eliminating other possibilities, the most plausible reason for this dry bias was found to be the improper reconditioning of dropsondes during their initialisation procedure before launch. The dry bias is suspected to have been caused due to contaminant retention on the moisture sensor, which should otherwise have been removed in case of a regular reconditioning.

The current understanding of how sensor contamination affects moisture measurements is quite poor and hence, an adequate correction based on physical reasoning is not possible. Nevertheless, the dry bias could have unintentional, far-reaching influences on further analyses via quantities such as precipitable water, area-averaged subsidence rate and density among many others. Therefore, I took an empirical approach to obtain a correction for the HALO sondes. I compared the HALO RH measurements with radiosonde launches from the neighbouring research vessel Meteor and the BCO (Stevens et al., 2016). Comparing the three RH distributions over different altitude windows in the atmosphere, I found the bias in the HALO measurements to have a scaled offset (see Fig. A.5 in Appendix A). Applying a multiplicative factor of 1.06 to the HALO humidity measurements shows much better agreement among the compared RH distributions. It is strongly recommended to apply the correction to the HALO humidity measurements.

Although the correction stems from an empirical analysis, it is currently the best approach to such a dry bias in dropsondes. This correction can also guide approaches for

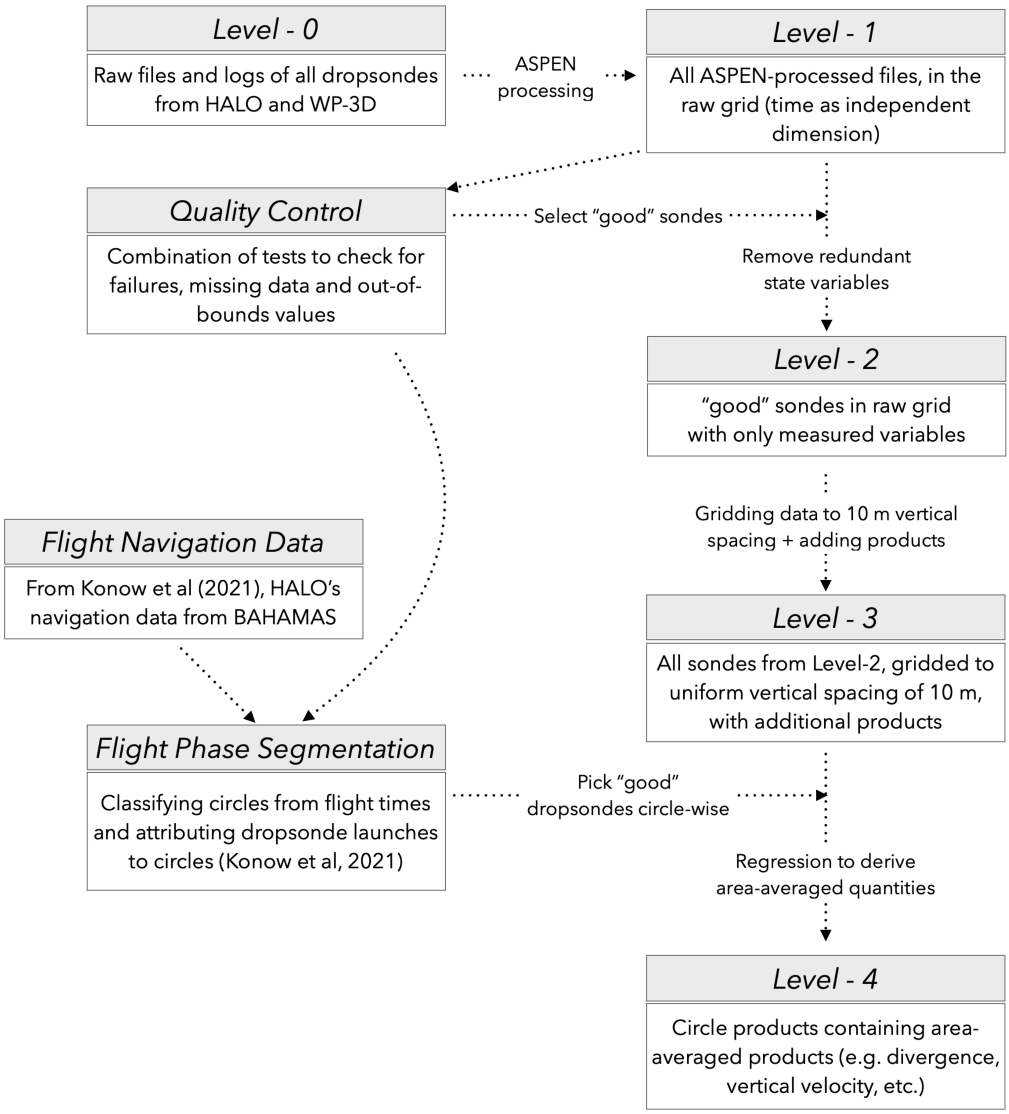

Figure 2.3: Flowchart outlining the processes and data products involved in JOANNE. Details of the processes and products are provided in Appendix A.

other datasets that have experienced a similar dry bias, e.g. the dropsonde measurements from Polar 5 during AFLUX 2019 (Becker et al., 2020).

2.3.3 *JOANNE Data Levels*

JOANNE is divided into five levels of data products, each with added layers of processing and synthesis. Level-0 contains the raw data files and logs of the dropsonde instruments, whereas Level-1 contains the output of the ASPEN processing run on the Level-0 raw files. Starting Level-1 onwards, all files in JOANNE are of the netCDF format.

The quality control, described in section 2.3.1, is run on the Level-1 files, and the soundings flagged as *good* are included in Level-2, after removing redundant state variables. Only quantities measured by dropsondes are kept as variables in Level-2. Level-3 comprises all soundings from Level-2, gridded on a uniform vertical spacing of 10 m with additional products such as potential temperature and specific humidity. Level-4

includes circle products and thus contains area-averaged quantities estimated from the circles flown during EUREC^{4}A.

JOANNE, in tandem with measurements from other platforms of EUREC^{4}A, such as the data from the radiosondes network (Stephan et al., 2020), is already being used by several research studies for characterising different aspects of the trade-wind atmosphere. For example, the divergence, vorticity and subsidence variables available from Level-4 form the core of the third study in this dissertation (see Appendix C), where the meso-scale circulation is characterised. The study is summarised in chapter 4.

3

THE INFLUENCE OF VERTICAL MOTION ON CLOUDINESS

It does not say in the Bible that all laws of nature are expressible linearly!

- Enrico Fermi (Gleick, 1987)

3.1 THE NARVAL2 CASE STUDIES

The NARVAL2 circles are the first set of measurements in the trade-wind regions, wherein both the cloudiness and the environment – in terms of the thermodynamics and the kinematics – are well-characterised. In a sense, these data can be thought of as coming from a cloud chamber experiment where the tuning parameters and the results, although completely in Nature's control, are known to us. Therefore, it presents the opportunity to understand the meso-scale environment's control on tropical clouds, in particular the influence of vertical motion.

The measurements taken during NARVAL2 were not limited to trade-wind conditions, but extended to conditions closer to the moist tropics, or the inter-tropical convergence zone (ITCZ). Inspired by the bimodal distribution of column moisture in the tropics (Mapes et al., 2018), I divided the eight NARVAL2 circles into four S-circles and four A-circles. The 'S' and 'A' stand for *suppressed* (or shallow-convective) and *active* (or deep-convective) cases, respectively. We investigate these eight case-studies to determine how the environment controls cloudiness at the meso scale.

3.2 CHARACTERISING THE ENVIRONMENT AND CLOUDINESS

3.2.1 *The environment*

I used dropsonde measurements as the primary tool for characterising environmental quantities. These can be separated into (a) thermodynamic quantities such as static energy, precipitable water (PW), free tropospheric humidity, lifting condensation level (LCL), lower tropospheric stability (LTS), inversion height and (b) kinematic quantities such as the surface wind speed, the area-averaged divergence ($\mathcal{D}$) and subsidence (ω). Fig. 3.1 gives a quick visualisation of the thermodynamic (left panel) and kinematic (right panel) aspects of the environment for the S-circles (shown row-wise).

The vertical structure of the static energy profiles does not vary much among the S-circles. The thermodynamic structure varies more among days than among circles far away, but flown on the same day. This indicates that such variations occur rather over the large scale than the meso scale. Conventional cloud-controlling factors such as SST, PW and LTS also do not show significant changes among the S-circles, despite there being variations in cloudiness as we shall see in the following subsection.

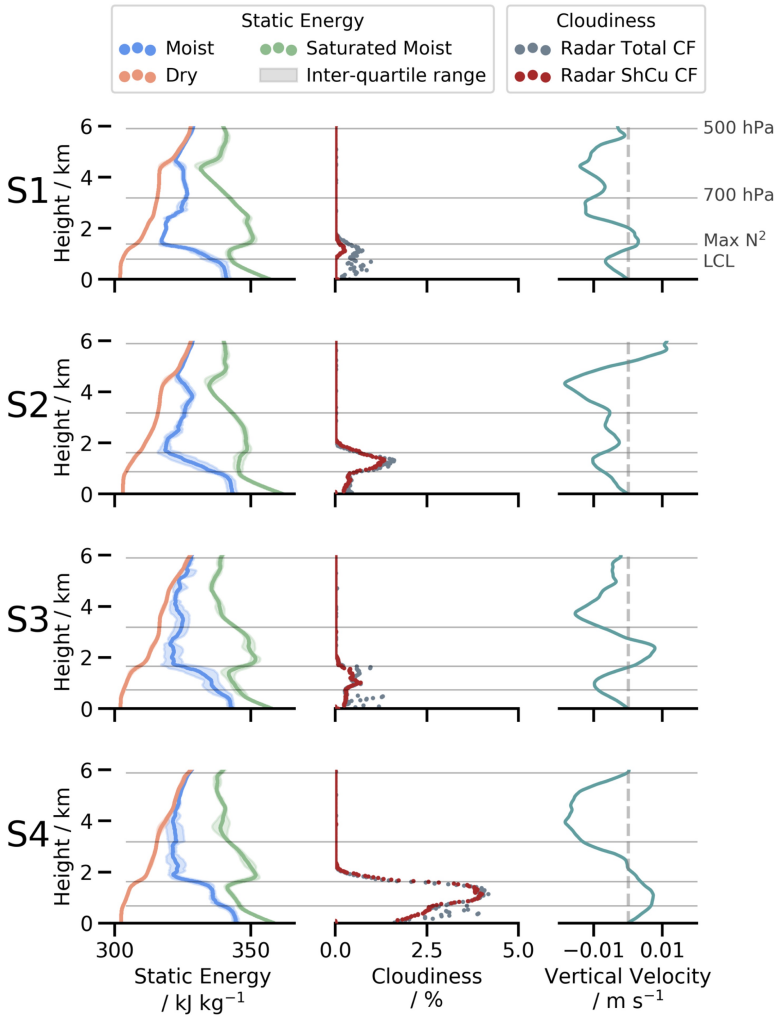

Figure 3.1: For the S-circles in NARVAL2, the static energy profiles (left), cloudiness profiles (centre) and the meso-scale vertical motion profiles (right) are shown. The grey lines, cutting horizontally across all profiles are, from bottom to top, levels of LCL, maximum N^2, 700 hPa and 500 hPa, for the particular circle. The static energy values, ω and vertical velocity are determined from dropsonde measurements, and the cloudiness profiles are obtained from the HAMP radar as echo fractions of total cloud fraction (grey) and shallow cumulus cloud fraction (dark red).

3.2.2 *Cloudiness*

To characterise the cloudiness in the circles, I mainly use HALO's suite of remote-sensing instruments (see Fig. 2.2a). Measurements from the HAMP radar are used to estimate total cloud fraction. Additionally, with some restraints on cloud base height (<1km) and cloud top height (<4km), I extract the shallow cumulus cloud fraction (see middle column in Fig. 3.1) from the total cloud fraction. The HAMP microwave radiometer provides estimates of liquid water path (LWP) and rain water path (RWP), used to quantify cloud activity and precipitation in the circles, respectively. The WALES (Wirth et al., 2009) lidar provides cloud top height values from its measured backscatter profile. I estimate the cloud cover in the circle using the fraction of WALES profiles that encountered clouds.

Since the aircraft only samples the circumference, satellite observations from GOES-13 (Knapp, 2017) are used to quantify cloudiness within the circle. As the satellite and lidar

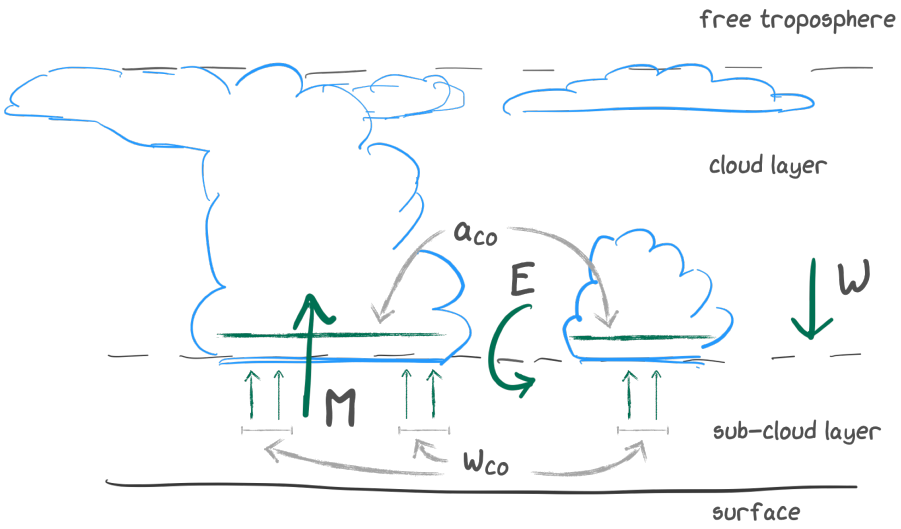

Figure 3.2: Schematic shows terms involved in the estimation of mass flux (M) by equations 3.1 and 3.2. The terms are explained in the text.

profiles only provide information about cloud tops, cumulative profiles of cloud cover going from top to the surface are obtained from both instruments, as opposed to vertical profiles of cloud fraction obtained from the radar.

Among the S-circles, the radar cloud fraction profiles show S4 to have a significantly larger cloud fraction compared to the remaining three S-circles (Fig. 3.1). S4 also has relatively greater values of LWP and RWP, showing that there is more liquid water content and precipitation in circle-S4 compared to the others. Satellite observations show that S4 also had higher cloud tops (~3.5 km) compared to the other S-circles, wherein clouds had their tops at ~2 km. The characterisation of cloudiness in the A-circles and how they compare to the S-circles has been detailed in Appendix B and has not been discussed here for brevity.

3.3 Influence of vertical motion on cloudiness

A key difference in the circles with the largest occurences of shallow clouds (S4 and A2) is that both show converging airmasses in their sub-cloud layer. I assert this as a crucial factor responsible for the higher measures of cloudiness, especially among the S-circles since they vary little in terms of their thermodynamic conditions.

A hypothesis that provides a possible explanation is how the influence of vertical motion on the convective mass flux increases cloud core area fraction. Fig. 3.2 provides a simplistic schematic which shows the terms associated with this hypothesis. A simple description of the convective mass flux velocity (M) is the rate of air ventilated out of the sub-cloud layer via the base of clouds through updrafts of air. Since all parts of a cloud do not experience updrafts, the parts that do are called the cores of clouds. Thus, M can, by definition, be estimated as

$$M(z) = a_{co}(z) \cdot w_{co}(z) \tag{3.1}$$

where a_{co} is the area of cloud cores and w_{co} is the mean updraft velocity at cloud base. Another way of estimating M as an area-averaged quantity is by calculating it as a residual of the sub-cloud layer mass budget including the entrainment rate E and the meso-scale

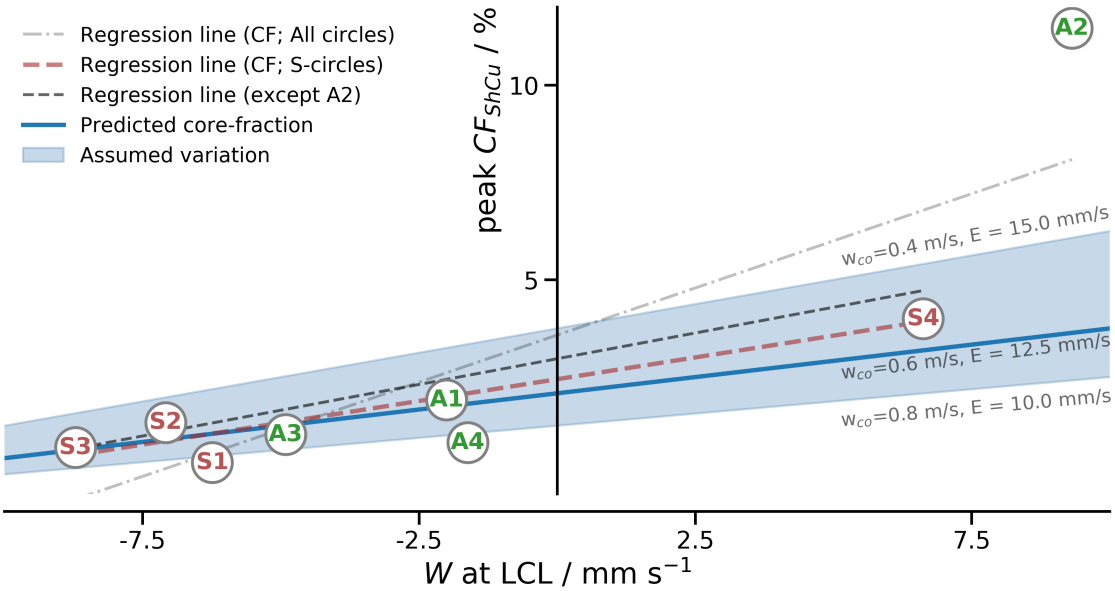

Figure 3.3: Peak shallow cumulus cloud fraction (CF_{ShCu}) from the radar is plotted against the large-scale vertical velocity at respective LCL heights of the circles. The shaded regions show the range of estimated cloud core fractions based on mass flux calculations (refer to the text)

vertical velocity W at the top of the sub-cloud layer (Vogel et al., 2020). Thus, assuming the depth of the sub-cloud layer to be steady over the period of 1-2 hours, we estimate M as,

$$M = E + W \tag{3.2}$$

Combining equations 3.1 and 3.2 gives a way to estimate cloud-core area fraction from the meso-scale vertical velocity as,

$$a_{co} = \frac{E + W}{w_{co}} \tag{3.3}$$

Thus with expected values of E (Vogel et al., 2020) and w_{co} (Sakradzija and Klingebiel, 2020) for the region, I can use equation 3.3 to make a simplistic theoretical prediction of the cloud-core area fraction given the vertical velocity, W. This is shown by the blue line and shaded region in Fig.3.3. I overlay actual cloud fraction from the radar on this prediction, which is shown by markers of circle names in Fig.3.3. There are some nuances to the interpretation of Fig. 3.3, which are provided in Appendix B. But overall, the reasonable agreement between the measurements and the simplistic theoretical prediction strengthens the argument that, over the meso scale, vertical velocity in the sub-cloud layer has more control over cloudiness than do thermodynamic factors. While this has been suggested previously by Mauger and Norris (2010) and Szoeke et al. (2016), such relationships have not been observed in nature before.

The scaling of cloud fraction with W also tells us about the nature of the relationship between cloudiness and the meso-scale circulation. No measure of cloudiness can be negative. Hence, the relationship between W and clouds is, in fact, non-linear. This goes to invalidate the argument that the response of clouds to the meso scale averages out to zero over the large scale, and that the large-scale relationships between clouds and their environment are sufficient to predict clouds accurately at the climate scale.

4

CHARACTERIZING THE CIRCULATION

Before one can make any serious attempt to explain the circulation of the atmosphere, he must become familiar with the circulation which he wishes to explain... experience suggests that the investigator who attempts to deduce the atmospheric circulation without first observing it is placing himself at a considerable disadvantage...

-Edward Lorenz (1967)

Findings from the NARVAL2 case-studies highlight the importance of circulation in cloud processes, and strengthens the case to better understand the meso-scale circulation itself. Here, I use measurements from the 70 EUREC^{4}A circles flown by HALO to describe the structure and variability of meso-scale circulation parameters such as horizontal mass divergence ($\mathcal{D}$), relative vorticity (ζ) and subsidence rate (ω) in the winter-time trades.

4.1 MEAN VERTICAL STRUCTURE

4.1.1 *Vertical structure of the atmosphere in the trades*

Certain layers of the trade-wind atmosphere are of special importance in setting the vertical structure and have been used in studies pertaining to the trade-wind regime since decades (Malkus, 1958; Augstein et al., 1974; Vogel et al., 2020). These will also aid in our discussion of the structure of meso-scale circulation quantities. Here I call them collectively as layers of interest and only identify them, but more detail on their definitions is provided in Appendix C. The layers are as follows with mean values during EUREC^{4}A indicated in parentheses.

1. *surface layer* : the lowest 50 m from the surface
2. *mixed layer* : the neutrally stable, well-mixed layer from the top of the surface layer up to the level of maximum relative humidity (~630 m)
3. *inversion layer* : the stable moisture-capping layer, a characteristic feature of the trades (~2260 m)
4. *triple-point isotherm* : the altitude at which the atmospheric temperature is the triple-point temperature of water (~4840 m).

There is often a transition layer at the top of the mixed layer, and they both together form the sub-cloud layer. The layer between the sub-cloud layer top and the inversion layer is called the cloud layer. The entire layer from the surface to the inversion layer is called the moist layer. The layers are shown in Fig. 4.1 along with the profiles of divergence, vorticity and subsidence from EUREC^{4}A measurements.

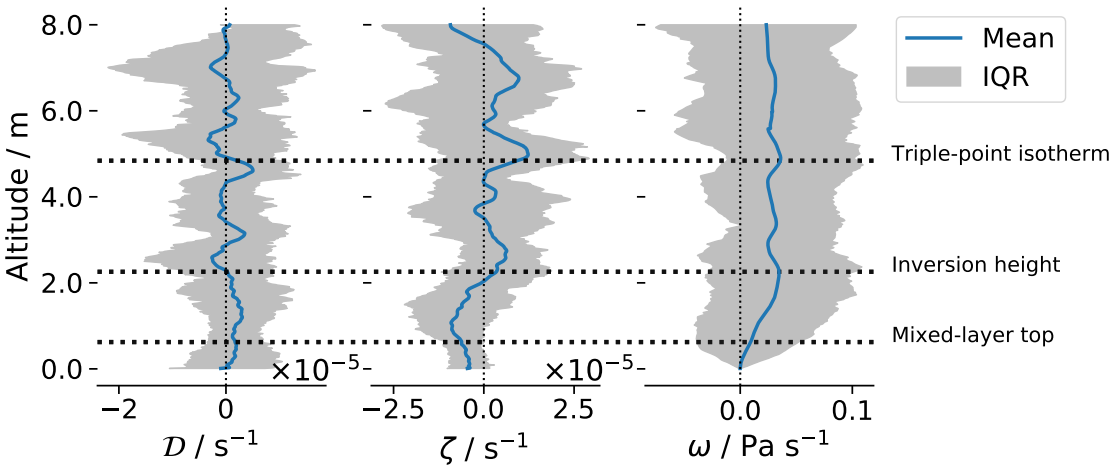

Figure 4.1: The vertical structure of the atmosphere in the trade-wind regions shown by measurements taken during the EUREC^{4}A campaign of divergence (left), vorticity (middle) and subsidence rate (right). Thick, blue line shows the mean and the grey, shaded region indicates the inter-quartile range of measurements through the period of the campaign. Horizontal dotted lines cutting across panels show mean values of mixed layer top (bottom-most), inversion height (middle) and triple-point isotherm (uppermost) during EUREC^{4}A.

4.1.2 *Mean profile of divergence, vorticity and subsidence*

The $\mathcal{D}$ mean profile (see left-most panel in Fig. 4.1) shows three key features between the surface and the triple-point isotherm, namely (a) a layer of divergence throughout the moist layer with a local minimum at the mixed layer top, (b) layers of alternating convergence (below) and divergence (above) just above the inversion, (c) layers of alternating divergence below and convergence above the triple-point isotherm. The colocation of these features with the layers of interest is an interesting feature, since $\mathcal{D}$ is estimated from horizontal winds whereas the layers are estimated from specific humidity (q) and potential temperature (θ). The divergence structure is driven by the radiative cooling profile in the long-term and I assert that this is how the structure of q and θ set the structure for $\mathcal{D}$ over time scales longer than a few days.

The mean profile of ω (shown in the right-most panel in Fig. 4.1) shows an almost linear increase of subsidence from surface upto a local maximum at the inversion layer, due to the complete divergence in the moist layer. Thereafter, in the free troposphere, ω is relatively consistent and has a mean value of 1 hPa h^{-1}. This mean subsidence value in the free troposphere can be used to estimate the mean cooling rate of the atmosphere. An approximation of the weak temperature gradient (Sobel et al., 2001) can be applied to do so. The mean cooling rate comes to $\sim$1.29 K d^{-1} which conforms with previous understanding about the cooling rate of the sub-tropics (Hartmann and Larson, 2002; McFarlane et al., 2007).

Diverging airmasses are often associated with anti-cyclonic rotation of air, and this is also observed in the mean profile of ζ (see middle panel in Fig. 4.1). Thus, throughout the moist layer, ζ shows negative values following the positive $\mathcal{D}$. However, the agreement between both is only for the mean profile and profiles of individual circles or even of daily means do not show a similar association.

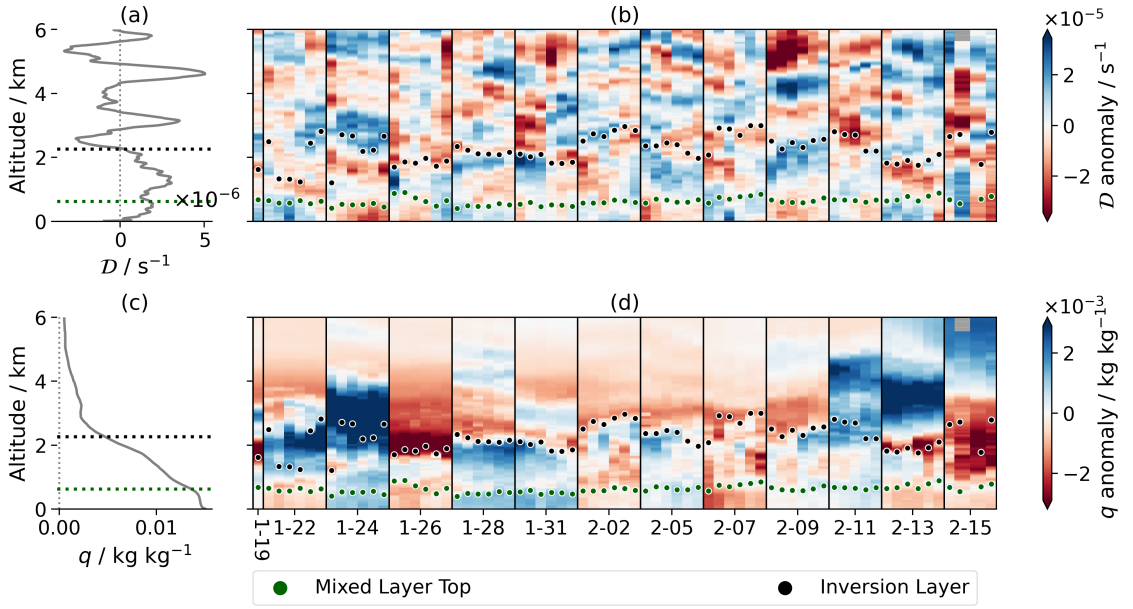

Figure 4.2: Vertical profiles of (a) $\mathcal{D}$ and (c) q averaged over all HALO-EUREC^{4}A circle measurements. The anomaly from time-mean (shown as hues) of $\mathcal{D}$, and q for individual circle profiles are shown in (b) and (d), respectively. The profiles are separated into different boxes based on their respective flight dates, which are indicated on the bottom of the x-axis in (d). Each box includes the same number of profiles corresponding to the EUREC^{4}A-circles flown during the respective flight. Profiles are sequenced based on circle-count, and the scale of x-axis is not linear in time. The mixed-layer top and inversion height are overlaid as green and black dots (lines on left panels), respectively.

4.2 VARIABILITY

A quick overview of the range of meso-scale circulation conditions sampled during EUREC^{4}A can be seen in Fig. 4.2b and 4.2d. Since the measurements were taken with no partiality towards any meteorological conditions, they provide an unbiased picture of the variability in the trades for the time period sampled.

I investigate the variability of the atmospheric parameters with dispersion measures such as the inter-quartile range (shown in Fig. 4.1) and the coefficient of variation (not shown here), the latter to compare the quantities over different units. These dispersion measures show that the magnitude of variability in area-averaged quantities ($\mathcal{D}$, ζ and ω) is much greater than that in the thermodynamics (q and θ). For example, the standard deviation of ω is roughly four times that of its mean value in the free troposphere and even greater in the moist layer. On the contrary, the standard deviation for q is of the same order of magnitude as its mean in the free troposphere and even lesser in the moist layer.

Observing such large ranges of variability in circulation parameters challenge current modelling strategies wherein climatological values are prescribed as forcings (e.g. Van-Zanten et al., 2011), even for limited-area high-resolution models where the spatial and temporal spacings are of the order of the meso scale I discuss here. It becomes especially important if processes in the meso scale are non-linear (such as those I find in section 3.3), since such large variability can amplify the difference between model results of prescribed meso-scale and large-scale forcings. Therefore, since measurements are now available, efforts must be made to restrain forcings to meso-scale profiles.

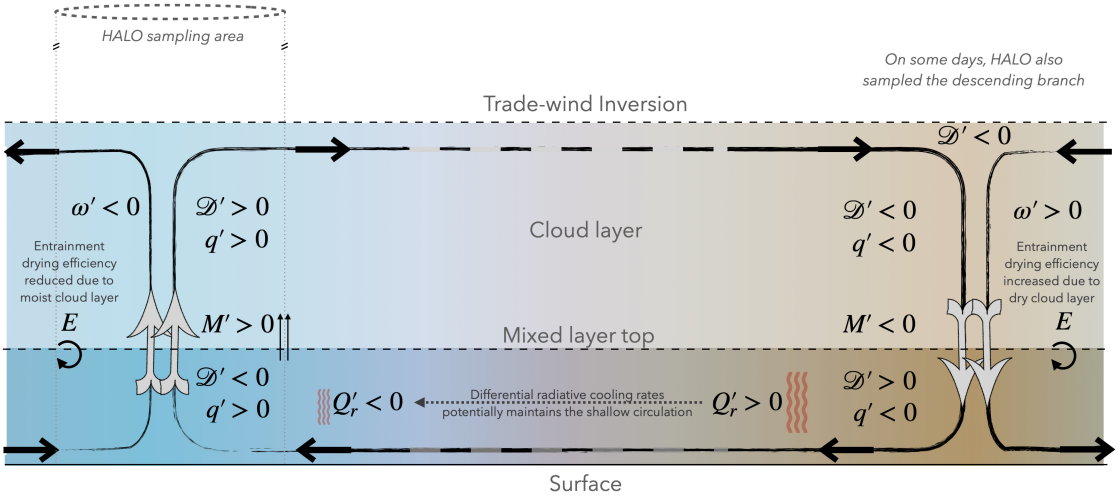

Figure 4.3: Schematic of the shallow circulation discussed in section 4.3 is shown. The marker ′ against any parameter indicates the parameter's anomaly from its mean. E stands for entrainment rate, M for shallow convective mass flux and Q_r for radiative cooling rate. The remaining symbols have the same meaning as in the text.

4.3 SHALLOW CIRCULATIONS

For most of the flight-days, in case of $\mathcal{D}$ anomaly from mean, the sign of the mean value in the mixed layer tends to be opposite to that of the mean in the cloud layer. A similar negative association is also found between the mixed-layer mean values of $\mathcal{D}$ anomaly and q anomaly.

I present a hypothesis that these associations can be explained by the presence of local shallow circulations in the trade-wind regions, which are of the depth of the moist layer. In the ascending branch of the circulation, air converges in the mixed layer and exports moisture vertically into the cloud layer via increased mass flux (equation 3.2). The increased moisture in the cloud layer reduces the drying efficiency of entrainment. Therefore, for a given entrainment rate, a converging mixed layer will moisten the cloud layer and subsequently, the mixed layer will have a greater moisture anomaly. Conversely, a diverging mixed layer will, over time, maintain a drying anomaly in the cloud and mixed layers. The differential radiative cooling between the moist, ascending region and the dry, descending region could potentially maintain the shallow circulation state (Schulz and Stevens, 2018; Naumann et al., 2019). A schematic of the proposed shallow circulations is shown in Fig. 4.3.

The moistening and drying of the cloud layer is not an instantaneous process, and its effect on the drying efficiency of entrainment takes time. This explains why the associations found as evidence for the shallow circulations are clearer over day-means or circling-means rather than individual circle values. The q anomaly in the mixed layer also correlates positively with that in the cloud layer over day-means, thus providing more evidence to the hypothesized shallow circulation.

More details regarding the meso-scale circulation quantities such as their day-to-day variability, their intra-day variability as well as how measurements varied under special meteorological conditions such as cold pools and shallow convection organisation patterns, are discussed in the study (Appendix C) but have been left out of this brief summary.

5 CONCLUSION AND OUTLOOK

A cloud does not know why it moves in just such a direction and at such a speed, it feels an impulsion... But the sky knows the reasons and the patterns behind all clouds, and you will know too, when you lift yourself high enough to see beyond horizons.

- Richard Bach (1981)

5.1 ANSWERING THE RESEARCH QUESTIONS

Here, we look at how the results of the three studies summarised in sections 2 through 4 help answer the research questions posed in section 1.3. The summaries alone do not cover all arguments used in this chapter to answer the research questions, so I refer the more ambitious reader to the complete studies in appendices A through C.

1. **Given the state of the atmosphere in the meso scale, what can be said about the cloudiness?**

   For understanding the relationships between the environment and cloudiness, we looked at the case-studies from NARVAL2, where the cloudiness and the environment have both been extensively characterised. At the meso scale, vertical motion plays a stronger role in regulating cloudiness than cloud-controlling factors shown to be important at the large scale. Particularly, conditions with converging boundary layers show a greater occurrence of cloudiness and precipitation in the trade-wind regimes. The argument also extends to conditions of deep convection but weakly, since the comparison of thermodynamics is not as straightforward in deep convection cases as in trade-wind cases, where thermodynamics do not vary much.

   a) *How well do conventional cloud-controlling factors perform in predicting cloudiness at the meso scale?*

      Conventional cloud-controlling factors such as lower tropospheric stability, sea surface temperature, and surface winds do not adequately explain the variability observed in the cloudiness. Whereas factors such as subsidence at 500 hPa (ω_{500}) and precipitable water are able to distinguish cases of deep convection from shallow convection, these still do not correlate well with any measure of cloudiness within a given regime.

   b) *What is the influence of meso-scale vertical motion on clouds?*

      A comparison of case-studies of suppressed convection reveals that with a converging sub-cloud layer, increased amounts of cloudiness are observed in terms of cloud fraction, liquid water and rain water path. This is not enough to prove that the vertical motion influences cloudiness. However, in the lack of such an argument, no explanations remain for the increased cloudiness

because other factors (e.g. thermodynamics) do not vary significantly among the cases. Thus, the rising vertical air in the sub-cloud layer becomes the most plausible explanation for the greater cloudiness. This also means that at the meso scale, the vertical motion holds a stronger influence on clouds than do other cloud-controlling parameters influential at the large scale.

c) *Could extending meso scale relationships to the large scale potentially affect cloud and climate processes, i.e. Can we comment on the linearity of the cloud response to meso-scale conditions?*

An explanation of how vertical motion influences cloudiness is provided via its regulation of the shallow convective mass flux (M). This relationship shows a positive scaling of cloud-core fraction with vertical velocity. This relationship is thus non-linear, because at large negative values of vertical velocity (W), cloudiness cannot go below zero. This challenges the ansatz of current climate models that the influence of meso-scale conditions is inconsequential when averaged over the large scale. If the response of clouds to the meso-scale conditions is non linear, as we show, then the clouds' response to meso-scale perturbations is not zero. Thus, the current parameterisation strategy of not including vertical motion becomes particularly concerning, because any changes occuring in the meso-scale circulation due to global warming will not be reflected by changes in clouds and cloud feedbacks due to their assumption of linearity.

The NARVAL2 case studies are a small sample (eight circles), and therefore, the relationships might not be robust. It is worth noting however, that there is great depth in characterisation of the atmosphere and the clouds for this limited sample. Thus, relationships apparent in these observations cannot be dismissed solely due to the low number of instances. The relationships expressed here certainly cannot be taken quantitatively. But the NARVAL2 cases put forth the argument that for determining cloudiness accurately, the meso-scale circulation is not something that should be ignored any more, especially with field campaigns such as EUREC^{4}A making investigations in this direction more feasible than ever before.

2. **What are the characteristics of the meso-scale circulation?**

I use measurements from 70 EUREC^{4}A circles, unbiased towards any particular meteorological conditions, to describe the characteristics of the meso-scale circulation via its defining variables such as horizontal mass divergence ($\mathcal{D}$), relative vorticity (ζ) and subsidence rate (ω). The 70 circles ranged over 13 flight-days and on most days, 6 circles were flown within a period of 7-8 hours. This opens the possibility to investigate variability of circulation parameters on inter- and intra-day scales.

a) *What is the mean vertical structure?*

The mean divergence structure shows positive values, i.e. diverging air, throughout the moist layer, indicating a consistency in kinematic characteristics of the sub-cloud and cloud layer in long term means. Above the moist layer, two distinct alternating bands of divergence and convergence are observed, one each at the inversion height and the triple-point isotherm. Moreover, in terms of subsidence, a completely subsiding mean profile is observed, with values in the moist layer increasing linearly upwards and a local maximum at the inversion height. The mean vorticity distinctly shows negative values in the moist layer, indicative of anti-cyclonic direction of rotation.

b) *What is the variability in the circulation parameters and how does this compare with that of thermodynamic quantities on the meso scale?*

   Over several different measures of dispersion, I find that values of divergence, vorticity and subsidence show much larger magnitudes of variability compared to their mean values. This is in stark contrast to the variability observed in thermodynamic parameters. The mean profile of humidity or potential temperature can also be representative of an hourly or daily profile of humidity. However, the nature of the circulation parameters to change sign and show such large variability means that their value on any given day bears no resemblance to that of the long term mean, neither in magnitude nor in vertical structure. Some consistent features can be observed in the day-to-day profiles of divergence though. On almost all days, the divergence anomaly from the mean in the sub-cloud layer showed opposite sign from that in the cloud layer. Moreover, in most days a sign change in divergence can be observed within the proximity of the inversion layer.

c) *What is the interplay between the meso-scale circulation and other environmental quantities thought to influence cloudiness?*

   I propose a shallow circulation mechanism of the depth of the moist layer to explain the negative association between divergence in the sub-cloud and cloud layers. It also explains the negative association of divergence and humidity in the sub-cloud layer. These shallow circulations can maintain areas of high and low moisture and could potentially maintain themselves by the resulting radiative cooling difference between the moist and dry branches of the circulation. Such shallow circulations could also potentially aid in the aggregation of convection and clouds. In terms of the mean values though, the co-location of striking features in divergence with the atmosphere's distinct layers leads to the reasoning that over the long-term the humidity and temperature set the radiative cooling profile which in turn could regulate the divergence structure.

The biggest takeaway from the EUREC^{4}A characterisation of meso-scale circulation is that at the meso scale, variables that describe the circulation, i.e. divergence, vorticity and subsidence, vary greatly from the climatology, not only in magnitude by a factor of at least four times the mean, but also in terms of their vertical structure, which shows drastic changes over two to three days. This raises a question about how effective is the current strategy of prescribing climatological values to models. Whilst this would definitely provide undesirable results for process studies, it could also be detrimental over the climate scales if there is even little deviation from linearity in the way clouds couple to the meso-scale circulation. These results strongly recommend that models be prescribed forcings of vertical motion at meso-scale values, constrained by measurements like the ones discussed here.

5.2 FRUITFUL COLLABORATIONS

My work with the circle measurements from NARVAL2 placed me in a privileged position where I could develop an expertise in the analysis of these novel measurements of vertical motion. During the EUREC^{4}A campaign I was thus made responsible for coordinating dropsonde operations from HALO. Participating in the campaign and working with the measurements opened the doors for collaboration on studies led by other colleagues,

where I contribute with my knowledge of the measurements and the analysis of the area-averaged quantities of the atmosphere. I provide a brief summary of existing and ongoing studies here.

It is a pleasure to be part of the EUREC^{4}A overview paper (Stevens et al., 2021), via my contribution of Figure-9 and related ideas in section 3.1 of the paper, both of which describe how EUREC^{4}A achieves the objective of making measurements to test hypothesized cloud feedbacks. My primary involvement with the HALO flights also helped me contribute to the paper describing HALO's participation in the EUREC^{4}A campaign (Konow et al., 2021), which we plan to submit in a matter of days. For this paper, I am involved in the segmentation of flight tracks of HALO and in the provision of metadata via the dropsondes. Additionally, my involvement in the paper is also as a mission PI for one of the HALO flights during the campaign, a role I am grateful to have played.

Comparing the EUREC^{4}A observations with global storm-resolving models provides an idea of how well the new high-resolution models represent the trade-wind characteristics and if there are any clear biases present in the model. I carry out this comparison as a part of a study by Wengel et al. (2021), which gives an overview of these DYAMOND-Winter ICON runs.

I am also involved in a study (Nuijens et al., 2021) where the objective is to describe the trade-wind momentum budget and its variability from the EUREC^{4}A circle measurements. In another study (Savazzi et al., 2021), we use wind observations from EUREC^{4}A to evaluate the tropospheric wind bias in the IFS model of the ECMWF and attempt to explain these biases with the tendencies and divergence observed in the campaign.

Outside of working with the NARVAL2 and EUREC^{4}A data, I also collaborated with colleagues from the ACTIVATE field experiment, wherein I estimated the area-averaged quantities for ACTIVATE's circles which sampled cold-air outbreak events. The study tests the sensitivity of the atmospheric boundary layer and clouds to forcings during cold air outbreaks and is detailed in Li et al. (2021).

5.3 OUTLOOK

JOANNE has already begun contributing to the scientific community by its use in several studies (e.g. Albright et al., 2021; Stephan and Mariaccia, 2021; Touzé-Peiffer et al., 2021, and others in preparation). It can serve as a benchmark and template for future campaigns involving dropsondes measurement. The HALO-(AC)^3 team are already planning to adopt JOANNE's structure with some necessary modifications to create a similar dataset for their dropsonde measurements for their campaign in 2022.

Similar to the analysis in the NARVAL2 circles, case-study analyses of EUREC^{4}A circles can give a deeper understanding of the processes by which circulation impacts cloudiness. Further, investigations into shallow circulations can be made to find more evidence which either confirm or invalidate the hypothesis, both of which raise interesting possibilities. EUREC^{4}A measurements of cloudiness can also help understand if clouds are regulated by the kinematic or the thermodynamic regulation of these shallow circulations. A comparison of the meso-scale circulation measurements from EUREC^{4}A with models and reanalysis products will also benefit in understanding biases in the latter and finding solutions for their improvement.

The studies in this dissertation are evidence that measurements from EUREC^{4}A and similar field experiments can push the frontiers of understanding the clouds-circulation coupling. To look at it in a metaphorical sense, one can go back to the quote by Richard Bach (1981) in the beginning of this chapter, but here I would cheekily add a few words,

"... the sky knows the reasons and the patterns behind all clouds, and you will know too, when you lift yourself high enough to see beyond horizons... *or just high enough to fly circles and launch sondes.*"

Part II

APPENDICES

A

JOANNE : JOINT DROPSONDE OBSERVATIONS OF THE ATMOSPHERE IN TROPICAL NORTH ATLANTIC MESO-SCALE ENVIRONMENTS

The work in this appendix has been published as:

George, Geet, Bjorn Stevens, Sandrine Bony, Robert Pincus, Chris Fairall, Hauke Schulz, Tobias Kölling, Quinn T. Kalen, Marcus Klingebiel, Heike Konow, Ashley Lundry, Marc Prange, and Jule Radtke. (2021). "JOANNE : Joint dropsonde Observations of the Atmosphere in tropical North atlaNtic meso-scale Environments". *Earth Syst. Sci. Data Discuss.* [preprint], in review, doi:10.5194/essd-2021-162

The contributions of the authors to this paper are as follows:

JOANNE was conceived by GG. The sounding strategy for EUREC^{4}A was designed by BS and SB. RP and CF adapted this for the P3's participation through ATOMIC. HS and TK contributed to the design and processing of the data. GG and BS performed the quality control. The manuscript was mainly written by GG with contributions by BS. GG, HS, MK, HK, MP and JR were responsible for dropsonde launch operations and real-time data quality control over different HALO flights. QK and AL were responsible for processing and quality-controlling the data for the P3 flights. All authors read and approved of the manuscript.

JOANNE : Joint dropsonde Observations of the Atmosphere in tropical North atlaNtic meso-scale Environments

Geet George[1], Bjorn Stevens[1], Sandrine Bony[2], Robert Pincus[3,4], Chris Fairall[4], Hauke Schulz[1], Tobias Kölling[1], Quinn T. Kalen[5,*], Marcus Klingebiel[6,*], Heike Konow[7,*], Ashley Lundry[5,*], Marc Prange[8,9,*], and Jule Radtke[8,9,*]

[1] Max Planck Institute for Meteorology, Hamburg, Germany
[2] LMD/IPSL, Sorbonne University, CNRS, Paris, France
[3] Cooperative Institute for Research in Environmental Sciences, University of Colorado, Boulder, Colorado, USA
[4] NOAA Physical Sciences Laboratory, Boulder, Colorado, USA
[5] NOAA Aircraft Operation Center, Lakeland, Florida, USA
[6] Institute for Meteorology, University Leipzig, Leipzig, Germany
[7] Meteorological Institute, Universität Hamburg, Hamburg, Germany
[8] Meteorological Institute, Center for Earth System Research and Sustainability, Universität Hamburg, Hamburg, Germany
[9] International Max Planck Research School on Earth System Modelling, Max Planck Institute for Meteorology, Hamburg, Germany
[*] These authors contributed equally to the work

Received and accepted for review: 11 May 2021 / Discussion started: 12 May 2021

ABSTRACT

As part of the EUREC[4]A field campaign which took place over the tropical North Atlantic during January-February 2020, 1216 dropsondes from the HALO and WP-3D aircraft were deployed through 26 flights to characterize the thermodynamic and dynamic environment of clouds in the trade-wind regions. We present JOANNE (*Joint dropsonde Observations of the Atmosphere in tropical North atlaNtic meso-scale Environments*), the dataset that contains these dropsonde measurements and the products derived from them. Along with the raw measurement profiles and basic post-processing of pressure, temperature, relative humidity and horizontal winds, the dataset also includes a homogenized and gridded data set with 10 m vertical spacing. The gridded data are used as a basis for deriving diagnostics of the area-averaged meso-scale circulation properties such as divergence, vorticity, vertical velocity and gradient terms, making use of sondes dropped at regular intervals along a circular flight path. 85 such circles, ~222 km in diameter, were flown during EUREC[4]A. We describe the sampling strategy for dropsonde measurements during EUREC[4]A, the quality control for the data, the methods of estimation of additional products from the measurements and the different post-processed levels of the dataset. The dataset is publicly available (https://doi.org/10.25326/221) as is the software used to create it (https://doi.org/10.5281/zenodo.4746313).

A.1 INTRODUCTION

"EUREKA! This is what I want to study for the rest of my life."

In an exclamation of serendipitous prescience Joanne Simpson is reported to have said these words upon learning about the possibility of studying trade-wind cumulus clouds through airborne measurements (Fleming, 2020). Her subsequent research proved foundational for tropical meteorology. Some seven decades later, the 2020 *ElUcidating the RolE of Cloud-Circulation Coupling in ClimAte* (EUREC^{4}A) field campaign, unwittingly expressed her exclamation of enthusiasm in finding purpose on the same topic.

The EUREC^{4}A field-campaign took place in January-February, 2020 and comprised measurements from many platforms. It adopted Barbados as its base of operations and focused its measurements in an area extending eastward of the Barbados Cloud Observatory (BCO; Stevens et al., 2016). EUREC^{4}A's initial scientific motivation, its subsequent evolution, and the final execution are described in Bony et al. (2017) and Stevens et al. (2021). As these papers emphasise, a central element of EUREC^{4}A was the airborne release of dropsondes to characterise the mesoscale meteorological environment of cloud fields in the trades. The dropsondes were mostly deployed to enable accurate estimates of the mean vertical motion field, using an approach inspired by Lenschow et al. (1999, 2007) and adapted to dropsondes by Bony and Stevens, 2019. Beyond estimating mesoscale vertical motion, the dropsondes were also aimed at characterising the thermodynamic structure in this region. In the stratified atmosphere of the trades, the dropsondes can resolve strong vertical gradients in temperature and moisture over short vertical distances, which are difficult to measure through remote-sensing (Stevens et al., 2017). The dropsondes are thus essential in characterising the atmospheric environment within which many complementary measurements took place during EUREC^{4}A. The purpose of this manuscript is to describe the resultant dropsonde dataset, which we call the *Joint dropsonde Observations of the Atmosphere in tropical North atlaNtic meso-scale Environments*, or JOANNE, in honour of Joanne Simpson's seminal contributions to our field of research.

JOANNE comprises five levels of data products, with each successive level encompassing a greater degree of synthesis and post-processing. The basic measurements that go into the JOANNE data products, and how they were made, are discussed in Section A.2. Quality control (QC) on the data are explained in Section A.3, and evidence for a possible dry bias is presented in Section A.4. The different levels of data products, and how they were constructed, are described in Section A.5 and Section A.6 concludes with a brief summary.

A.2 SAMPLING AND MEASUREMENTS

A.2.1 *Instrument and Sensors*

JOANNE is based entirely on data collected by Vaisala's RD-41 dropsondes (hereafter also 'sondes'; Vaisala, 2020a). A dropsonde is similar to a radiosonde, with the exception that it is designed to be launched out of airborne platforms and sinks down through the atmosphere to the surface while making measurements. Each sonde has a cylindrical, cardboard casing that houses within it the measurement sensors, a GPS receiver, a battery and a signal transmitter for communicating with the airborne receiving station. The casing is attached to a parachute that is designed to align the sonde properly for measurements and to reduce the fall speed.

Table A.1: Details about sensors used in the RD-41 and RS-41 sondes are provided. Repeatability is the standard deviation of differences in twin soundings. The values for the sensors are obtained from Vaisala (2020a) and values for wind measurements estimated from GPS are obtained from Vaisala (2020b). All numbers are provided in terms of absolute units, correspondingly in the first column.

Sensor / Measurements (Units)	Type	Range	Least Count	Repeatability
Pressure (hPa)	Silicon capacitor	surface pressure to 3	0.01	0.4
Temperature (°C)	Platinum resistor	-90 to +60	0.01	0.1
Relative Humidity (%)	Thin-film capacitor	0 to 100	0.1	2
Wind speed ($m\,s^{-1}$)	estimated from GPS	max reported 180	0.1	0.15
Wind direction (°)	estimated from GPS	0 to 360	0.1	2

The sondes carry three sensors - one each for measuring pressure (p), temperature (T) and relative humidity (RH), together referred to as the PTU sensors and with a sampling frequency of 2 Hz. The GPS receiver allows the position of the dropsonde to be tracked, from which ambient winds are estimated at a sampling frequency of 4 Hz. The sensors included in the sondes are the same as in Vaisala's RS-41 radiosondes (upsondes), which were also employed during EUREC^{4}A from the BCO and four other ship-based platforms (Stephan et al., 2020). Table A.1 provides a brief summary of the type, the resolution and the expected performance from the sensors used in the RD-41 and RS-41 sondes.

A.2.2 *Sondes Deployment*

A total of 1216 dropsondes were launched: 896 from the German High-Altitude Long Range aircraft (HALO) and 320 from the National Oceanic and Atmospheric Administration's (NOAA) Lockheed WP-3D Orion N43-RF aircraft (P3). The P3 was operated as a part of the Atlantic Tradewind Ocean-Atmosphere Mesoscale Interaction Campaign (ATOMIC), which itself was a part of the EUREC^{4}A campaign. Throughout this manuscript, we use the term EUREC^{4}A to refer to both experiments.

Both aircraft used the Airborne Vertical Atmospheric Profiling System (AVAPS; UCAR/NCAR, 1993) with 8 simultaneous channels, for the operation of the dropsondes, as well as for the processing and quality control of collected data. For HALO, the dropsondes are launched from a pneumatic chute controlled manually, which is located at the rear, starboard side of the aircraft, slightly oriented towards the bottom of the fuselage. For the P3, the drop point is near the center of the fuselage, with a little offset to the starboard side. HALO typically launched sondes at an altitude between 10–10.5 km, whereas the P3 did so typically at ~7.5 km. Some P3 sondes were launched at ~3 km, when the P3 was flying typical lawn-mower patterns (straight, parallel, long legs connected by shorter, perpendicular legs; parts of some visible in the north in Fig. A.1) at low

altitudes to facilitate launching Airborne eXpendable BathyThermographs (AXBTs). The total number of dropsondes launched from the two aircraft per flight is given in Table A.2.

Nearly ninety percent (~87%) of the dropsondes launched reported data as expected, with partial data being recorded by a large percentage of remaining sondes. Only 51 (~4%) sondes provided no usable data. Almost all of these 51 sondes failed because of an error in automatically detecting launch, the cause for which was later attributed to a manufacturing error in certain batches of dropsondes (Vaisala, personal communication). Success rates for the other aspects of measurements are described in more detail in Section A.3.

A core part of the EUREC^{4}A campaign was meso-scale circular flight patterns, which were adopted for most (1021 sondes, ~84%) of the dropsonde launches. The use of a repetitive flight pattern was based on a desire to provide consistent and comparable estimates of meteorological variables. Circles were chosen to facilitate estimates of the profile of the meso (circle) scale divergence of the horizontal wind. Following the error analysis of Bony and Stevens, 2019 each circle aimed to launch twelve sondes. The number of sondes launched per circle is provided in Table A.3.

Most circles were flown along a fixed circular path, called the EUREC^{4}A-circle (Stevens et al., 2021), which was planned with the centre coordinates as 57.72°W, 13.30°N and a diameter of roughly 220 km. The location of the sonde launches shown in Fig. A.1, highlight the density of HALO sondes concentrated along the circumference of the EUREC^{4}A-circle. This circle was chosen such that complementary measurements are maximised between the aircraft and other platforms in EUREC^{4}A. Measurements performed along the EUREC^{4}A-circle were made irrespective of meteorological conditions and hence were unbiased. Flight times (see Table A.2) were adjusted to best sample the diel cycle given operational constraints. HALO was mostly restricted to daylight hours, while the P3 made 3 flights at night and is the only sampling of the night-time trades from EUREC^{4}A dropsondes.

The actual mean diameter of all EUREC^{4}A-circles marked by dropsonde launches was 222.82 km, and the mean centre was 57.67°W, 13.31°N. One circuit around the EUREC^{4}A-circle took HALO roughly 60 min to execute at a flight level of about 9.5 km, resulting in sonde launches separated by about 5 min. There were 85 dropsonde circles flown during EUREC^{4}A (see details in Table A.3), and 73 of these were EUREC^{4}A-circles, with HALO flying 70 of them and the rest flown by the P3. Of the 12 circles flown which were not EUREC^{4}A-circles, one (HALO-0215_c3) was flown by HALO to provide spatial contrast for comparison with measurements in the EUREC^{4}A-circle. The remaining 11 non-EUREC^{4}A circles were flown by the P3 and were mostly centered on the location of the NOAA research vessel Ronald H. Brown. The flight track of some of the P3 circles were approximated by a dodecagon.

Sondes were also dropped to sample conditions upwind and in the vicinity of EUREC^{4}A-circles, to aid calibration of other instruments, as references for satellite underpasses, and to support surface based measurements from Research Vessels and buoys. For instance, HALO typically separated a set of three standard EUREC^{4}A-circles by an upwind 'excursion' toward the Northwest Tropical Atlantic Station buoy (NTAS) near 51.02°W, 14.82°N, along which 1 to 3 sondes were launched per flight.

Table A.2: Total number of dropsondes launched, circles flown during the flight, as well as takeoff and landing times (in UTC) for the flight are provided with corresponding flight IDs. Numbers in parentheses in the second column indicate the number of good dropsondes per flight (explained in § A.3). Note that the table only shows circles with dropsonde launches. There were also circles flown with no dropsonde launches during EUREC^{4}A.

Flight ID	Dropsondes (Good)	Takeoff time	Landing time	Circles with dropsondes
P3-0117	23 (17)	2020-01-17 14:00:02	2020-01-17 20:50:00	1
P3-0119	28 (23)	2020-01-19 13:25:25	2020-01-19 21:47:51	1
P3-0123	38 (31)	2020-01-23 13:21:02	2020-01-23 21:29:14	2
P3-0124	16 (15)	2020-01-24 13:21:05	2020-01-24 22:14:32	0
P3-0131	25 (17)	2020-01-31 15:32:27	2020-01-31 23:36:04	1
P3-0203	22 (17)	2020-02-03 13:19:02	2020-02-03 19:21:57	1
P3-0204	31 (28)	2020-02-04 13:19:52	2020-02-04 21:54:08	1
P3-0205	29 (23)	2020-02-05 13:22:23	2020-02-05 21:59:43	1
P3-0209	32 (25)	2020-02-09 01:56:28	2020-02-09 10:13:37	2
P3-0210	32 (26)	2020-02-10 01:48:57	2020-02-10 09:54:42	2
P3-0211	44 (36)	2020-02-11 03:15:07	2020-02-11 11:21:50	2
HALO-0119	15 (12)	2020-01-19 09:34:25	2020-01-19 18:48:03	1
HALO-0122	73 (69)	2020-01-22 14:57:35	2020-01-23 00:10:30	6
HALO-0124	77 (71)	2020-01-24 09:29:30	2020-01-24 18:41:13	6
HALO-0126	75 (70)	2020-01-26 12:05:30	2020-01-26 21:20:49	6
HALO-0128	74 (71)	2020-01-28 14:58:34	2020-01-28 23:55:17	6
HALO-0130	4 (4)	2020-01-30 11:19:34	2020-01-30 15:08:20	0
HALO-0131	74 (68)	2020-01-31 15:08:35	2020-01-31 23:56:53	6
HALO-0202	89 (76)	2020-02-02 11:28:02	2020-02-02 20:13:24	6
HALO-0205	76 (65)	2020-02-05 09:15:51	2020-02-05 18:21:22	6
HALO-0207	73 (62)	2020-02-07 12:02:24	2020-02-07 21:11:40	6
HALO-0209	73 (66)	2020-02-09 09:14:31	2020-02-09 18:03:00	6
HALO-0211	61 (58)	2020-02-11 12:29:05	2020-02-11 21:37:29	5
HALO-0213	73 (69)	2020-02-13 07:56:10	2020-02-13 17:17:17	6
HALO-0215	51 (48)	2020-02-15 15:07:30	2020-02-16 00:12:44	5
HALO-0218	7 (1)	2020-02-18 10:11:05	2020-02-18 18:55:31	0

Table A.3: Details of circles flown during EUREC^{4}A. Circle Time is the mean launch time for all sondes in the circle. Longitude (°E), latitude (°N) and diameter (km) are those associated with the center of a least-squares fitted circle to all sondes. Dropsondes show total number of sondes launched in each circle. The number in parentheses (L4) show the number of good sondes (explained in §3) used for regression in Level-4.

Circle ID	Circle Time	Longitude	Latitude	Diameter	Dropsondes (L4)
P3-0117_ci1	15:55	-51.00	14.84	181.86	12 (9)
P3-0119_ci1	15:02	-52.97	14.50	180.90	12 (9)
P3-0123_ci1	14:31	-54.96	14.38	186.96	12 (11)
P3-0123_ci2	20:12	-55.68	13.29	185.34	12 (9)
P3-0131_ci1	16:53	-54.38	13.84	184.74	12 (7)
P3-0203_ci1	14:40	-54.50	13.92	183.19	13 (11)
P3-0204_ci1	14:50	-53.14	13.49	184.45	12 (11)
P3-0205_ci1	15:12	-53.26	12.23	179.63	12 (10)
P3-0209_ci1	04:55	-57.67	13.26	243.92	12 (10)
P3-0209_ci2	06:22	-54.87	13.84	187.64	12 (10)
P3-0210_ci1	04:55	-57.74	13.30	220.41	12 (7)
P3-0210_ci2	06:12	-54.78	13.77	184.77	12 (11)
P3-0211_ci1	06:06	-57.71	13.30	221.59	12 (12)
P3-0211_ci2	07:16	-55.49	14.23	185.69	13 (10)
HALO-0119_c1	17:53	-57.86	13.27	186.65	12 (10)
HALO-0122_c1	15:45	-57.70	13.27	222.45	12 (12)
HALO-0122_c2	16:58	-57.71	13.28	223.80	12 (12)
HALO-0122_c3	18:09	-57.72	13.27	220.95	12 (11)
HALO-0122_c4	20:12	-57.70	13.29	224.13	13 (12)
HALO-0122_c5	21:27	-57.71	13.29	223.64	12 (11)
HALO-0122_c6	22:34	-57.71	13.31	225.99	12 (11)
HALO-0124_c1	10:19	-57.62	13.23	231.01	13 (10)
HALO-0124_c2	11:30	-57.66	13.28	224.16	13 (13)
HALO-0124_c3	12:42	-57.69	13.28	223.83	12 (12)
HALO-0124_c4	13:57	-57.68	13.27	223.80	12 (12)
HALO-0124_c5	15:07	-57.69	13.27	223.98	12 (12)
HALO-0124_c6	16:16	-57.68	13.27	223.47	13 (11)
HALO-0126_c1	12:49	-57.68	13.29	224.27	12 (12)
HALO-0126_c2	14:01	-57.67	13.30	219.53	12 (10)
HALO-0126_c3	15:10	-57.69	13.28	221.75	12 (11)
HALO-0126_c4	17:47	-57.67	13.29	224.49	12 (12)
HALO-0126_c5	19:00	-57.69	13.28	221.71	12 (11)

Continued on next page

Table A.3: Details of circles flown during EUREC^{4}A. Circle Time is the mean launch time for all sondes in the circle. Longitude (°E), latitude (°N) and diameter (km) are those associated with the center of a least-squares fitted circle to all sondes. Dropsondes show total number of sondes launched in each circle. The number in parentheses (L4) show the number of good sondes (explained in §3) used for regression in Level-4.

Circle ID	Circle Time	Longitude	Latitude	Diameter	Dropsondes (L4)
HALO-0126_c6	20:19	-57.67	13.29	224.16	12 (12)
HALO-0128_c1	15:46	-57.70	13.30	223.86	12 (12)
HALO-0128_c2	16:57	-57.70	13.30	223.84	12 (12)
HALO-0128_c3	18:11	-57.69	13.32	221.09	12 (11)
HALO-0128_c4	20:25	-57.71	13.32	226.18	12 (11)
HALO-0128_c5	21:41	-57.70	13.30	223.89	12 (12)
HALO-0128_c6	22:55	-57.70	13.30	224.00	13 (12)
HALO-0131_c1	15:57	-57.70	13.31	225.87	11 (11)
HALO-0131_c2	17:06	-57.72	13.31	226.37	12 (11)
HALO-0131_c3	18:20	-57.69	13.30	219.07	12 (10)
HALO-0131_c4	20:28	-57.69	13.29	224.03	12 (12)
HALO-0131_c5	21:42	-57.70	13.29	224.15	12 (12)
HALO-0131_c6	22:54	-57.68	13.29	221.11	12 (11)
HALO-0202_c1	12:12	-57.72	13.29	224.80	12 (10)
HALO-0202_c2	13:18	-57.71	13.28	223.70	12 (11)
HALO-0202_c3	14:27	-57.71	13.27	225.77	13 (11)
HALO-0202_c4	16:55	-57.70	13.28	226.26	12 (9)
HALO-0202_c5	18:03	-57.72	13.28	222.28	12 (11)
HALO-0202_c6	19:06	-57.71	13.29	224.82	13 (12)
HALO-0205_c1	09:59	-57.70	13.29	220.90	12 (11)
HALO-0205_c2	11:11	-57.70	13.28	220.83	14 (11)
HALO-0205_c3	12:21	-57.72	13.26	223.22	12 (11)
HALO-0205_c4	15:03	-57.71	13.23	224.79	12 (10)
HALO-0205_c5	16:11	-57.73	13.28	226.25	13 (10)
HALO-0205_c6	17:24	-57.73	13.26	221.54	12 (11)
HALO-0207_c1	12:47	-57.73	13.28	223.83	12 (12)
HALO-0207_c2	13:57	-57.74	13.28	223.89	12 (11)
HALO-0207_c3	15:08	-57.73	13.29	223.34	12 (7)
HALO-0207_c4	17:44	-57.74	13.28	228.51	12 (10)
HALO-0207_c5	18:57	-57.73	13.28	224.13	12 (12)
HALO-0207_c6	20:14	-57.75	13.30	226.98	12 (9)
HALO-0209_c1	10:00	-57.70	13.26	224.99	12 (11)
HALO-0209_c2	11:12	-57.70	13.26	224.47	12 (10)

Continued on next page

Table A.3: Details of circles flown during EUREC^{4}A. Circle Time is the mean launch time for all sondes in the circle. Longitude (°E), latitude (°N) and diameter (km) are those associated with the center of a least-squares fitted circle to all sondes. Dropsondes show total number of sondes launched in each circle. The number in parentheses (L4) show the number of good sondes (explained in §3) used for regression in Level-4.

Circle ID	Circle Time	Longitude	Latitude	Diameter	Dropsondes (L4)
HALO-0209_c3	12:26	-57.68	13.28	221.13	12 (11)
HALO-0209_c4	14:27	-57.70	13.26	224.30	12 (11)
HALO-0209_c5	15:37	-57.70	13.26	223.40	12 (11)
HALO-0209_c6	16:53	-57.68	13.28	220.94	12 (11)
HALO-0211_c1	13:25	-57.71	13.32	229.02	12 (10)
HALO-0211_c2	14:38	-57.66	13.30	223.89	12 (12)
HALO-0211_c3	15:49	-57.64	13.31	221.66	11 (11)
HALO-0211_c4	17:05	-57.67	13.32	225.76	12 (11)
HALO-0211_c5	18:25	-57.66	13.30	224.00	12 (12)
HALO-0213_c1	08:43	-57.65	13.32	223.47	12 (12)
HALO-0213_c2	09:55	-57.65	13.33	222.41	12 (10)
HALO-0213_c3	11:04	-57.65	13.32	223.76	12 (12)
HALO-0213_c4	13:33	-57.65	13.32	223.49	12 (12)
HALO-0213_c5	14:49	-57.65	13.32	223.42	12 (12)
HALO-0213_c6	16:03	-57.66	13.32	224.27	12 (11)
HALO-0215_c1	16:06	-57.73	13.29	223.31	11 (11)
HALO-0215_c2	17:14	-57.68	13.25	229.76	8 (7)
HALO-0215_c3	18:47	-52.04	13.91	224.94	12 (11)
HALO-0215_c5	22:10	-57.67	13.33	222.44	13 (13)
HALO-0215_c6	23:12	-57.59	13.22	237.56	7 (6)

Additional details and strategies for HALO and P3 flights which may be informative for those sondes not launched on standard circles, can be found in Konow et al. (2021) and Pincus et al. (2021), respectively.

The maximum drift of the sondes from their launch locations in the horizontal space had a median of around 2.5 km, as seen in Figs. A.2 and A.3. In the lower troposphere, the drift was generally more along the zonal direction than in the meridional direction, with sondes tending to drift towards the southeast of the launch location. Due to a climatological wind reversal at near 3 km the maximum displacement for HALO is at about this level, whereas for the P3 which dropped its sondes from a lower altitude and thus sampled less of the upper level westerlies, the maximum displacement is at the surface. This also explains why the drift of the P3 sondes is systematically to the west of the drop, and less directionally biased for the HALO sondes. The P3 sondes typically sampled the sub-cloud layer ~0.03° southwest of the launch location, whereas for HALO sondes, the direction of drift was influenced strongly by the winds above 3 km, and therefore varied between different flight days.

Table A.4: Table shows file types included in Level-0, which are all files in the raw data collected by the dropsondes, and a brief description of what they entail.

File Type	Description
A Files	Sounding attributes file; includes channel configuration, COM ports data, hardware configuration, launch obs data, sensor errors, aircraft data, software config and firmware information
B Files	File containing binary data; same as D-Files
C Files	Sounding data stored as comma-separated-value files
D Files	Raw sounding data recorded for timestamp at every 0.25 s
D_P Files	Only post-launch raw data; same as D-Files
R Files	Receiver ports data: signal strength and receiver frequency
0_SysLog Files	comma-separated-value file of all AVAPS system logs
1_Aircraft Files	TXT file of aircraft position data in the IWGADTS Format (IWG1)
2_GPSRef Files	TXT file of GPS data: GPGGA (system fix data) and GPRMC (minimum specific GPS/Transit data)
3_SpecAnlyzr Files	TXT file of logs of spectral analyzer

A.2.3 *Raw Data and Initial Processing*

The raw data collected on the aircraft by AVAPS and the subsequent processing with the Atmospheric Sounding Processing Environment (ASPEN; Martin and Suhr, 2021) software constitute Levels 0 and 1 of JOANNE, respectively. The data included as part of these two levels involve no external adjustments other than the standard processing and quality control by AVAPS and ASPEN – both state-of-the-art tools for dropsonde measurements.

A.2.3.1 *Level-0 (Raw data)*

Level-0 includes the raw files generated by AVAPS during dropsonde measurements. For every dropsonde launch, multiple files are generated, which store the collected data in different formats, with there being some extent of information overlap between them. These files have names starting with a capitalised letter and are described in Table A.4 with the corresponding letter as the file type.

In addition to these files, information about the hardware and the aircraft data are generated and stored each time the AVAPS system is switched on, usually once per flight. These files have names preceded by a number, and the type and content of these files are given in Table A.4.

All Level-0 files of a single day (as per UTC) are stored in their respective date directories, with their names in the format `YYYYMMDD`. The P3 and HALO directories are separated into two different directories named after the respective aircraft.

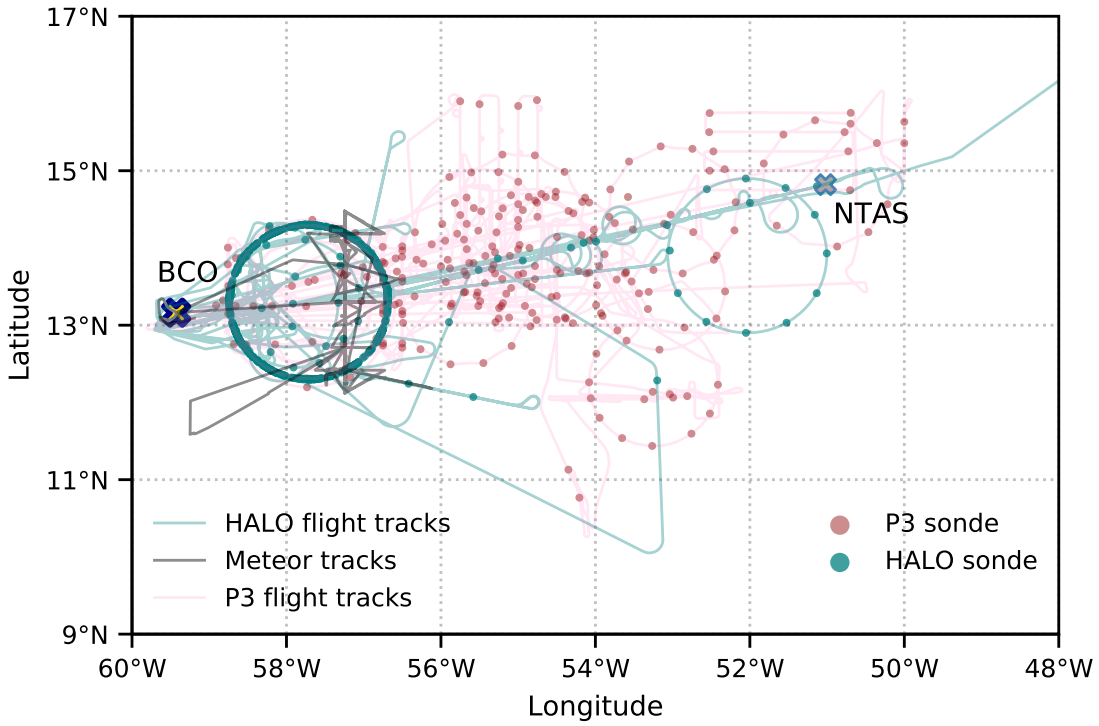

Figure A.1: Map showing the launch locations of the dropsondes during EUREC^{4}A from HALO (teal) and P3 (red). The flight paths for HALO (light teal), P3 (light pink) and Meteor (gray) are shown as shaded lines. The crosses near the west and east edges of the displayed domain mark the location of the BCO and the NTAS buoy, respectively.

A.2.3.2 *Level-1 (ASPEN processed data)*

Level-1 includes all files from Level-0 after processing by ASPEN. ASPEN takes in D-type files (see Table A.4) as input, and gives an output of quality controlled files. For JOANNE, the D files were supplied as input to BatchASPEN v3.4.3, and all output files have the suffix `_QC`. The files are in NetCDF format. For ASPEN processing, we used the standard *editsonde* configuration. A detailed explanation of the file-structure of these `_QC.nc` files and the processing steps carried out by ASPEN are outlined in detail by Martin and Suhr (2021). These Level-1 `_QC.nc` files serve as the input for further processing in JOANNE.

A.3 Quality Control (QC)

For the data products post Level-1, JOANNE aims to provide sounding profiles that do not contain any obvious measurement errors and contain minimal missing data records. After the ASPEN processing, we run additional QC tests on all Level-1 sounding profiles and filter out soundings that do not meet these objectives. Profiles which are filtered out during this QC are not included in Level-2 and onwards. We believe that soundings passing such a QC stage would best fulfil the purpose of the dropsondes – to characterise the EUREC^{4}A atmospheric environment – with little to no troubleshooting at the user end. However, users who wish to pursue a specific measurement that did not make it past the QC stage can still avail themselves of it in the exhaustive Level-0 and Level-1 data products.

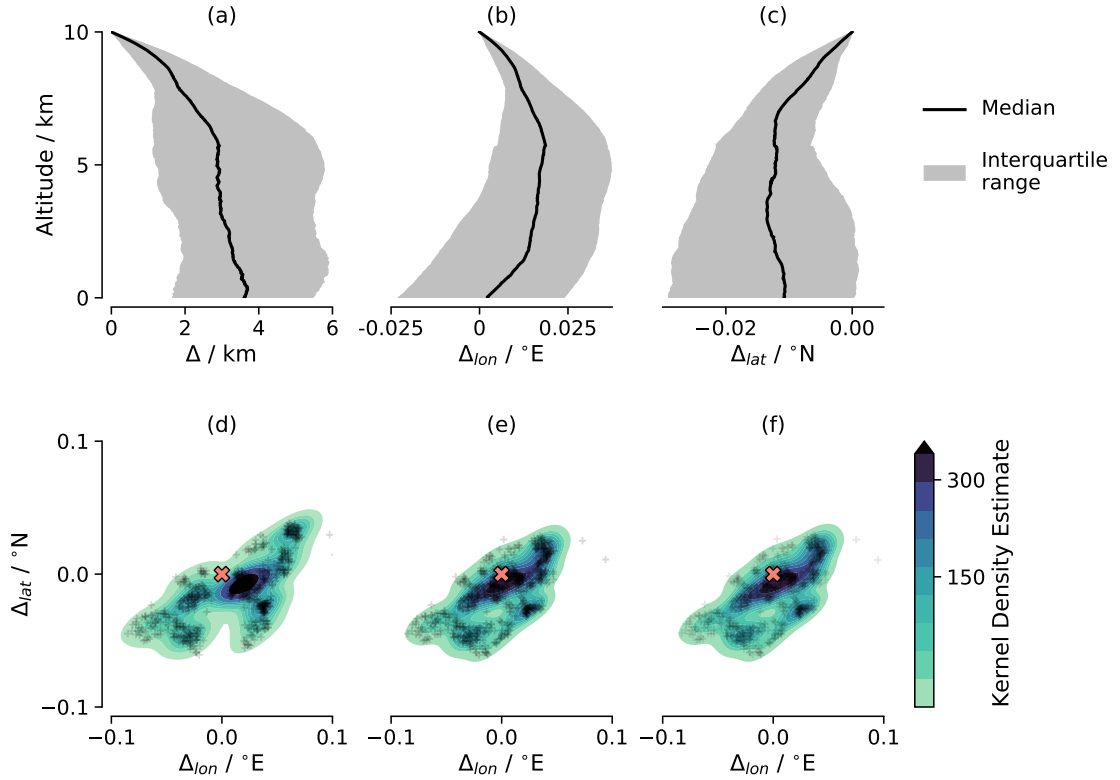

Figure A.2: Figure shows an overview of the drift in HALO sondes. Δ indicates horizontal displacement in sondes from launch location. Figures (a)-(c) show the median drift from launch and the corresponding interquartile range for (a) horizontal displacement, (b) longitude and (c) latitude. Figures (d)-(f) show as colours the kernel density estimates (KDE) of drift from launch location (red cross) at (d) median altitude of maximum drift in the profile, $\tilde{z}$=3140 m (e) sub-cloud layer mean (0-500 m) and (f) at altitude of 2 km, where usually the cloud-top layer is present.

A sounding's success in the QC stage is provided by a parameter *qc_flag* which has possible values of *good*, *bad* and *ugly*. The values stand for fully-usable, non-usable and partially-usable data, respectively and are described in more detail later with relevant context. Only soundings flagged as *good* are included in JOANNE after Level-1. A sounding's *qc_flag* value is determined by its collective performance in three tests that are designed with the aforementioned QC objectives in mind. These tests are listed as follows.

1. Launch Detection Test (*ld_test*) : This test filters sondes that failed to detect an automatic launch

2. Profile Fullness Test (*sat_test*) : This test filters sondes that did not record measurements for at least 80% of the time measured in the profile

3. Low-altitude Measurements Test (*low_test*) : This test filters sondes whose measurements in the lower levels of the atmosphere do not fall within the expected bounds of parameter values.

The details of how a sounding's performance is judged with these tests and how these tests combine to give the *qc_flag* value for the sounding are explained further in this section.

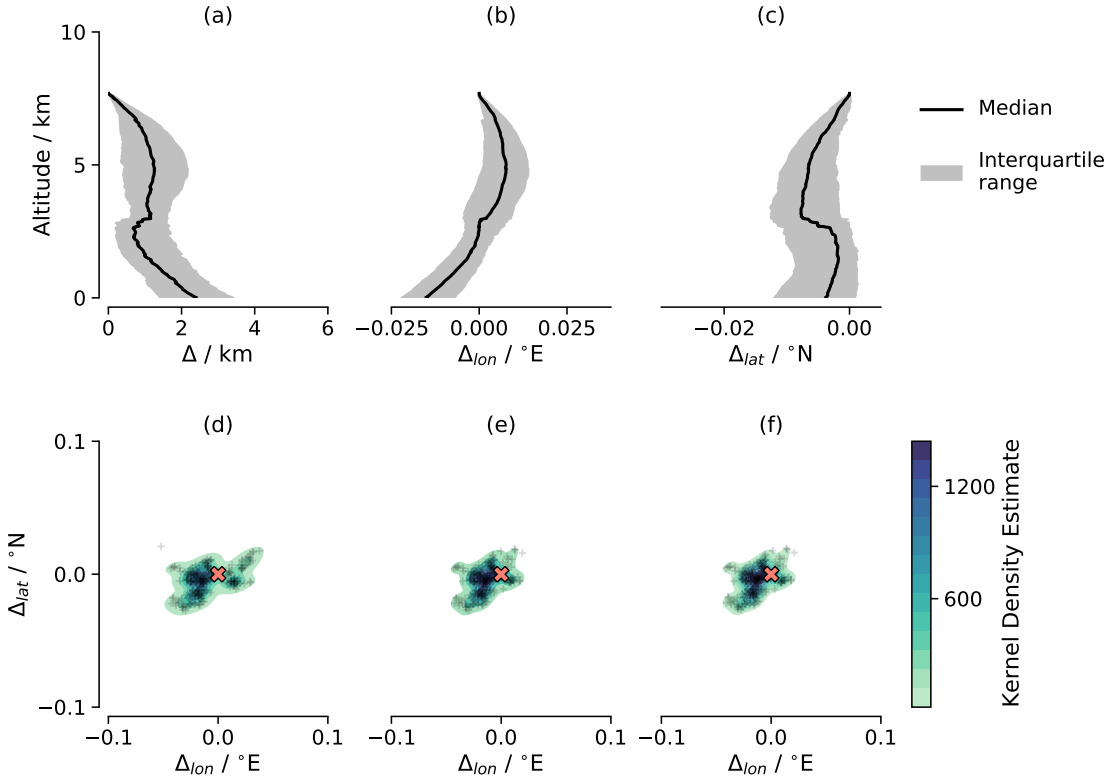

Figure A.3: Same as Fig. A.2, but for P3 sondes instead of HALO sondes. For (d), median altitude of maximum drift in the profile, $\tilde{z}$=10 m

A.3.1 *Launch Detection Test* (*ld_test*)

This test checks whether the sonde detected a launch automatically. If a sonde fails to automatically detect a launch, it does not switch to high-power signal transmission, and thus, fails to send data back to the AVAPS PC in the aircraft, after it has passed further than a short range. The receiver in the aircraft failed to detect any signal from such sondes usually after they had fallen below pressure levels of 300 hPa.

A sounding's success in this test is marked by a parameter of the same name, i.e. *ld_test* and has possible values of 0 and 1, which correspond to *bad* and *good*, respectively. The primary method to check launch detection is to parse through the sounding attribute log files (A-type; see Table A.4) in Level-0. These files have names starting with 'A' and are followed by the date and time of launch. The file extension is the number of the channel used to initialise the sonde and receive its signal. Note that for sondes that did not detect a launch, the file name has time when the sonde was initialised, whereas for the rest, the file name is for the time of the detected launch. The log file contains an internal record termed 'Launch Obs Done?'. If this value is 1, the launch was detected, else if it is 0, launch was not detected. The same values are used to mark the *ld_test*.

A.3.2 *Profile Fullness Test* (*sat_test*)

This test checks the abundance of measurements within a sounding profile relative to the flight time of the sonde. For a raw measurement profile, time is the independent dimension along which records of measurements are made. The time record is given by the 4 Hz GPS measurements which means that for the 2 Hz PTU measurements every other

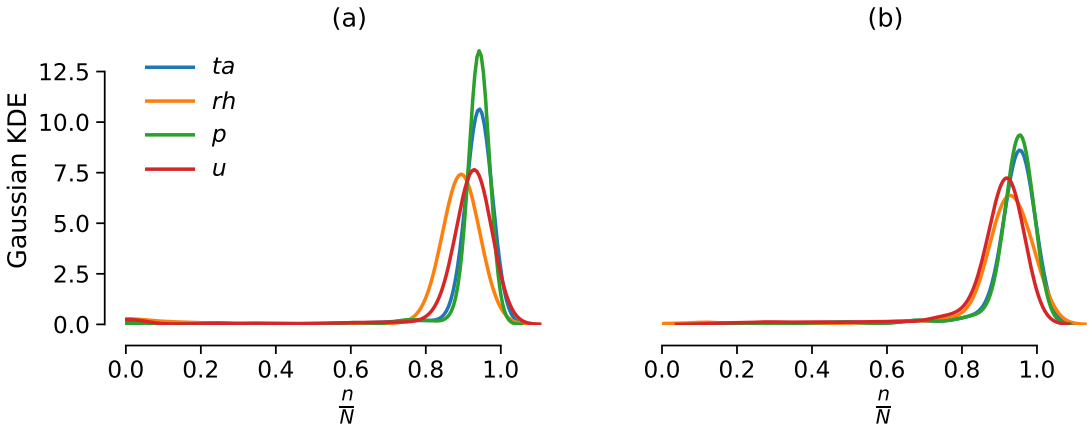

Figure A.4: Kernel density estimate of ratio of actual measurement counts (n) out of maximum possible count of measurements (N), based on the timestamp records in each sonde Level-1 file for (a) HALO and (b) P3. For u, N would be the total timestamp records in any given sonde profile, whereas for the rest it would be half that. In the legend, labels stand for temperature (ta), relative humidity (rh), pressure (p) and eastward wind (u). The northward wind (v) has the same distribution as u, and is hence not shown.

record is a missing value. Ideally, all parameters (except u,v) will have measurements at every other time record, and u,v at every time record, but in practice, the number of records with measurements always falls short of the ideal number. This is because the time records also include values during initialisation as well as during a little before and after the launch, when no signal can be sent back to the AVAPS PC. Thus, the ratio of actual measurements to total possible measurements is lower than the ideal estimate of 1.

The profile fullness test is run by checking the abundance of measurements individually for all parameters in a sounding. The success of the test for a parameter ϕ is recorded in a corresponding parameter ϕ*_test*, e.g. *p_test* corresponding to p (pressure) and this success is determined by the ratio of the count of its measurements (n) to its total possible measurements (N), denoted by,

$$\phi_{\text{sat}} = \frac{n(\phi)}{N(\phi)}. \tag{A.1}$$

Accounting for the different sampling rates of the GPS and PTU measurements, the distributions of ϕ_{sat} is shown in Fig. A.4, which shows that peaks start to flatten below 0.8. Thus, we set a threshold value of 0.8, and if parameter ϕ has ϕ_{sat} lower than this threshold, then it is taken as not having a complete profile, and ϕ*_test* is flagged as *ugly*. If ϕ_{sat} exceeds or matches the threshold, ϕ*_test* is flagged as *good*. If all values are missing, i.e. $\phi_{\text{sat}} = 0$, then ϕ*_test* is flagged as *bad*.

Whereas the aforementioned tests $(\phi$*_test*$)$ recorded the success for every parameter in a sounding, we use *sat_test* to record the success of a sounding. For a given sounding, if all parameter tests are *good*, the sounding's *sat_test* is flagged as *good*. Similarly, if all individual parameter tests are *bad*, *sat_test* is flagged as *bad*. If neither of these conditions is met, *sat_test* is flagged as *ugly*.

A.3.3 *Low-altitude Measurements Test* (*low_test*)

This test functions as a sanity-check for the measurements from a sounding in the lower levels of the atmosphere, which is mostly near the surface except for one test where the check is for the lowest 4 km. Similar to the profile fullness test, this test is also determined by the success of parameters over different individual tests. The success of these individual tests are recorded with a parameter name same as that of the corresponding test name. For each of these tests, if the sounding passes the test, it is marked as *good*, else as *bad*. The individual tests and their criteria for passing are as follows.

1. *low_p_test*

   This test checks if maximum pressure measured in a sounding is within bounds (1000–1020 hPa) and if so, the sounding passes the test. If maximum value of p is greater than upper bound, it is unrealistic, and if lesser than lower bound, it means that the sonde did not measure the near-surface levels of the atmosphere. This test does not check any GPS values. Even if there were no pressure measurements higher than 1000 hPa, there may still be GPS measurements in the low-altitude levels. Such sondes can still be useful for wind and wind-derived products.

2. *low_t_test*

   This test checks if air temperature measured in a sounding is within bounds. It sets two criteria for bounds, which are (a) maximum air temperature recorded should not be greater than 30 °C and (b) mean T in the bottom 100 m should not be lesser than 20 °C. If either of the above limits is violated, measurement of T for the sounding is considered out of bounds, and marked as *bad*. The sonde is also marked *bad*, if there are no measurements in the bottom 100 m (by GPS altitude (*gpsalt*) in Level-1).

3. *low_rh_test*

   This test checks if relative humidity measured in a sounding is within bounds. The criterion is that mean RH in the bottom 100 m should not be lesser than 50%. If this bound is violated, RH for the sonde is considered out of bounds, and marked as *bad*. The sonde is also marked *bad*, if there are no measurements in the bottom 100 m.

4. *low_z_test*

   This test checks if minimum *gpsalt* of a sounding is within bounds, i.e. $\leq$ 30 m above mean sea level. A value higher than the bound means there are no near-surface measurement values of GPS and consequently, horizontal winds. This flag does not include any geopotential height values. Even if there are no GPS values below 30 m, there may still be PTU measurements in the lowest levels.

5. *palt_gpsalt_rms_test*

   This test checks if the root mean square (RMS) difference between geopotential altitude (palt) and the GPS altitude (gpsalt),for values below 4 km, and is lower than 100 m. If the estimated RMS difference is below the limit, then the sounding is flagged as *good*. If the estimated RMS difference is greater than the limit, or if there are no values of either *palt* or *gpsalt* overlapping in the lower 4 km, then the sounding is flagged as *bad*. The lack of overlap could be because either there are no palt values or no gpsalt values or both.

Table A.5: Determination of *qc_flag* value based on success of sounding in the three QC tests – *ld_test*, *sat_test* and *low_test*. The * indicates that any value for the test satisfies the condition.

ld_test	*sat_test*	*low_test*	***qc_flag***
good	*good*	*good*	***good***
bad	*	*	***bad***
*	*bad*	*bad*	***bad***
– All other combinations –			***ugly***

Table A.6: Count of sondes that passed each QC test, separated by platforms

Platform	Classification	*ld_test*	*sat_test*	*low_test*	***qc_flag***
HALO	Good	854	814	831	**810**
	Bad	41	1	40	**41**
	Ugly	N/A	80	24	**44**
P3	Good	312	270	280	**258**
	Bad	4	0	8	**10**
	Ugly	N/A	52	34	**54**

Based on the success in the aforementioned individual tests, the overall success of a sounding for the low-altitude measurements test is recorded in the parameter *low_test*. If all individual tests are flagged as *good*, the *low_test* is flagged as *good*, and similarly, if all individual tests are flagged as *bad*, the *low_test* is flagged as *bad*. If neither of these conditions is met, the sounding's *low_test* is flagged as *ugly*.

Note that the bounds used for the individual tests are all considered keeping in mind the EUREC^{4}A region and conditions. For a similar QC in a different region or environment, the bounds for the parameters will likely be different.

A.3.4 *qc_flag*

The overall success of a sounding is recorded as values of *good*, *bad* or *ugly* in the *qc_flag* parameter, and is determined by the combination of success through the three QC tests, as shown in Table A.5.

Table A.6 summarises the statistics of the QC tests for HALO and P3. Although the process of classifying the sondes can be simplified by other combinations of the *sat_test* and *low_test* values, the method we present ensures no good sondes are omitted, and no bad sondes are admitted. The rest of the sondes, the ugly sondes, still have data that can be salvaged, and after some additional QC, can be combined with the other good sondes depending on the user's objective.

JOANNE provides a status file per platform, which stores the results for each individual test and group of tests mentioned above, as well as the final *qc_flag* classification for each sounding. Thus, the user can still mould the classification based on their objectives, add or remove tests to the process and customise the sonde selection for themselves.

A.4 DRY BIAS IN HALO DROPSONDES

The radiosonde measurements during EUREC^{4}A taken from the BCO and the research vessel Meteor show evidence of a dry bias in the humidity measurements of the HALO dropsondes. The HALO measurements are bounded by Meteor's on the upwind side and BCO's on the downwind side (see Fig. A.1). Since all three platforms have unbiased sampling, we expect that the HALO distribution should be between the other two. Fig. A.5 shows that the BCO and Meteor distributions of RH align closely throughout the lower troposphere and thus, HALO measurements should not differ. The offset in the HALO measurements towards lower RH values suggests a dry bias in the HALO sondes. Since the sensors for the dropsondes and the radiosondes are the same, an instrument difference can be ruled out. Further comparisons with other water vapour measurements in the vicinity such as the radiosondes from the ship Ron Brown, surface humidity measurements from both ships and dropsondes from the P3 aircraft also show HALO's median specific humidity to be lower than expected (not shown).

A possible contamination of the polymer film in the moisture sensor could affect its dielectric constant, whose fluctuations with respect to relative humidity is subsequently affected. The most plausible explanation is that the reconditioning procedure of HALO dropsondes was improper, which resulted in some trace gas pollutants being retained on the humidity sensor, and should otherwise have been removed during the reconditioning. The protocols of operation for P3 and HALO were not the same, and this leads us to believe that the improper reconditioning was only an issue for the dropsondes launched from HALO. In the case of radiosondes, the reconditioning is part of the automatic calibration process, and so it is not expected to cause problems.

A multiplicative correction factor of 1.06 to the RH values (dotted line in Fig. A.5) aligns the HALO distributions well with the BCO and Meteor distributions. The success of this simple rescaling, in both matching the mean and the variance of the distributions, suggests that the bias is both multiplicative and systematic. Had the bias come from a subset of the sondes, a multiplicative correction to match the mean would have resulted in a broader distribution. Had the bias been an additive one, then the correction would have not been as successful at all heights. It is not, however, understood how the contamination of the sensor leads to this dry bias, and why the multiplicative correction appears to work so well. For these reasons, the correction is not applied to the published data.

Users of the data should also be aware that the uncorrected dry bias in HALO dropsonde measurements will propagate into other variables, especially PW and moisture gradients (since it is apparently multiplicative) and will even have a slight effect on estimates of geopotential altitude which depend on the atmospheric density, and hence moisture content. However, the proposed multiplicative correction, should users wish to adopt it, is straightforward to apply to these data.

A.5 DATA PRODUCTS

A.5.1 *Level-2 (Quality Controlled Sounding Data)*

The Level-2 NetCDF files contain data from individual soundings, which passed with a *qc_flag* value of *good* from the QC stage (discussed in Section A.3). For Level-2, only variables that are measurements from the dropsonde sensors are included. Redundant state variables are not carried forward from the Level-1 files. Products up to Level 2 main-

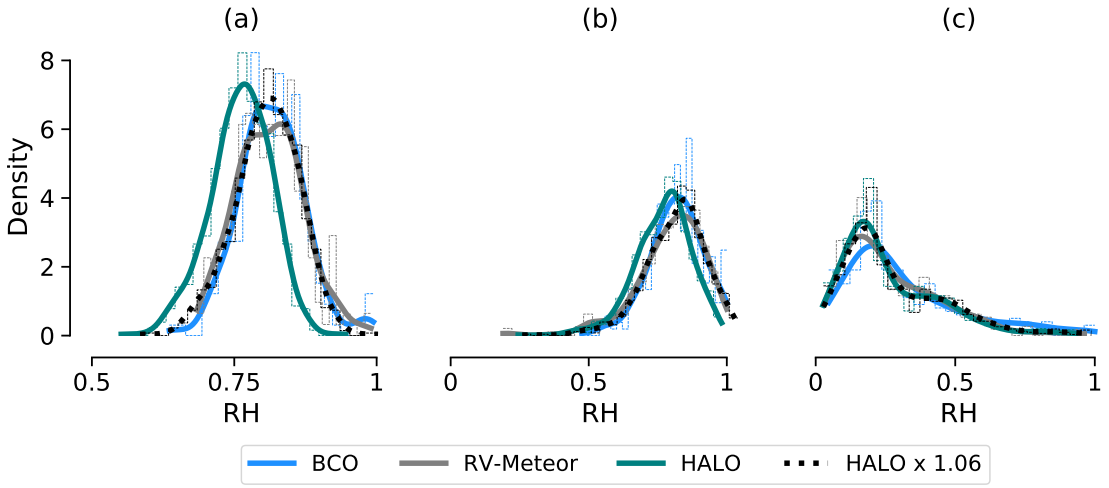

Figure A.5: Spread (kernel density estimates) in relative humidity values from soundings made by BCO, Meteor and HALO at (a) mean of 0-500 m, (b) mean of 750-1500 m and (c) mean of 2000 - 4000 m. The last item in the legend is for RH values of HALO multiplied by 1.06. To coincide with HALO measurement times, BCO and Meteor soundings between 03:00 and 09:00 UTC have been excluded from these distributions, which has a relatively insignificant impact.

tain the raw measurement profile, and data variables are aligned along the independent dimension `time`.

File names in Level-1 are generally indicative of launch times, however for sondes that did not detect a launch, the file name indicates time of initialisation. The attribute `Launch-time-(UTC)` in every sounding file of Level-2 should be considered as the final authority on launch time. This is the same as the variable *launch_time* in Levels-1 and 3.

`sonde_id` is a variable available in JOANNE products from Level-2 onwards. This is a unique, immutable identifier and is meant to identify exactly one dropsonde which corresponds to exactly one sounding profile. Note that the identifier variable `sounding_id` in the EUREC^{4}A radiosondes dataset (Stephan et al., 2020) identifies sounding trajectory and not instrument, since one instrument can have upward and downward trajectories. The JOANNE variable `sonde_id` functions solely as an identifier and no information should be interpreted from the semantics of this variable.

The Level-2 product consists of individual files for every sounding with the file structure as shown in Table A.7. All files also include flight information such as position, height, and speed as attributes. These are saved by the AVAPS aircraft computer in the sonde A-files (see Table A.4) and is input from the aircraft system itself. The files also have additional attributes such as the software version for post-processing and quality control. The file names are in the format:

`[campaign]_[project]_[instrument]_[sonde_id]_[version].nc`,

e.g. `EUREC4A_JOANNE_Dropsonde-RD41_HALO-0124_s42_v0.11.0.nc`. Note that `sonde_id` includes one underscore character within its value for the example shown.

A.5.2 *Level-3 (Gridded Data)*

Level 3 is a product combining dropsonde measurements launched from both the HALO and P3 aircraft, interpolated onto a uniform vertical grid of 10 m spacing, similar to the

Table A.7: Table shows the structure for the Level-2 product, outlining the coordinates, variables and their corresponding descriptions, units and dimensions.

OBJECT	NAME	DESCRIPTION	UNITS	DIMENSION
Coordinates	time	time of recorded measurement	seconds since 2020-01-01	time
	alt	geopotential height	m	time
	lat	latitude	degree_north	time
	lon	longitude	degree_east	time
Variables	p	atmospheric pressure	Pa	time
	ta	air temperature	K	time
	rh	relative humidity		time
	wspd	wind speed	$m\ s^{-1}$	time
	wdir	wind direction	degrees	time
	sonde_id	sonde identifier		

processing of EUREC^{4}A radiosounding profiles (Stephan et al., 2020). The product is a single file which contains, all dropsondes from Level-2 along the altitude dimension `alt`.

A.5.2.1 *Gridding*

The primary objective behind the Level-3 product is gridding all soundings on a common, vertical grid, thus making it easier to use the soundings for different analyses. The vertical grid spacing for the dataset is kept at 10 m, up to an altitude of 10 km.

In the case of a regular drop, i.e. if there are no issues like a fast fall, or a failed parachute, the average descent rate of the dropsondes is $\sim 21\,m\,s^{-1}$ at 12 km altitude and $\sim 11\,m\,s^{-1}$ near to the surface. The PTU sensors have a measurement frequency of 2 Hz, while the GPS has a 4 Hz measurement frequency. This would translate to a vertical sampling of roughly 9–10 m at HALO's flight altitude, and 5–6 m close to the surface for the PTU values and correspondingly finer vertical sampling for the GPS-based measurements. Hence the data are slightly coarsened, and only for PTU values in the upper-mid troposphere do the interpolated values exceed the resolution of the measurements. The gridding is carried out through the following steps.

1. Variables `q` (specific humidity), `theta` (potential temperature), `u` (eastward wind), and `v` (northward wind) are computed and added to the dataset (for details, see Section A.5.2.2).

2. All variables along the height coordinate in the dataset are averaged on 10 m bins up to 10 km altitude. In cases where no data are available in the altitude bin, a linear interpolation from neighbouring measurements along the height dimension is used to estimate the value in the altitude bin, with the restraint that the neighbouring measurements are not further apart than 50 m. If data are not available within 50 m of the desired height level, values at that height level are assigned `_FillValue`. While this still allows for a few missing values (~2-3 considering a fall speed of 15–20 $m\,s^{-1}$, it does not lead to substantial artificial information created by the smoothened interpolation between points relatively farther away.

3. Pressure values are interpolated logarithmically and these values replace the linearly interpolated pressure values.

4. Temperature (T) and relative humidity (RH) are the originally measured properties by the dropsonde sensors. However, for interpolation q and θ are preferred, as these variables are conserved. After interpolation, T and RH are recomputed from the interpolated values of θ and q. The recomputed values for T and RH replace the previously interpolated T and RH variables from the sounding.

5. Wind speed and wind direction are computed from the interpolated values of u and v and added to the interpolated dataset.

Table A.8: Table shows the structure for the Level-3 product, outlining the coordinates, variables and their corresponding descriptions, units and dimensions.

OBJECT	NAME	DESCRIPTION	UNITS	DIMENSION
Coordinates	alt	height obtained by integrating upwards the atmospheric thickness estimated from the hypsometric equation	m	alt
	sonde_id	unique sonde ID		sonde_id
	launch_time	time of dropsonde launch	seconds since 2020-01-01	sonde_id
	interpolated_time	value of time (original independent dimension) linearly interpolated to altitude grid	seconds since 2020-01-01	sonde_id, alt
	lat	latitude	degree_north	sonde_id, alt
	lon	longitude	degree_east	sonde_id, alt
Variables	p	atmospheric pressure	Pa	sonde_id, alt
	ta	dry bulb temperature	K	sonde_id, alt
	rh	relative humidity		sonde_id, alt
	wspd	wind speed	m s^{-1}	sonde_id, alt
	wdir	wind direction	degree	sonde_id, alt
	u	u-component of the wind	m s^{-1}	sonde_id, alt

Continued on next page

Table A.8: Table shows the structure for the Level-3 product, outlining the coordinates, variables and their corresponding descriptions, units and dimensions.

OBJECT	NAME	DESCRIPTION	UNITS	DIMENSION
	v	v-component of the wind	m s^{-1}	sonde_id, alt
	theta	air potential temperature	K	sonde_id, alt
	q	specific humidity	kg kg^{-1}	sonde_id, alt
	low_height_flag	flag if flight height < 4 km when dropsonde was launched		sonde_id
	platform_id	platform from which dropsonde was launched		sonde_id
	flight_altitude	altitude of the aircraft when dropsonde was launched	m	sonde_id
	flight_lat	north latitude of the aircraft when dropsonde was launched	degree_north	sonde_id
	flight_lon	east longitude of the aircraft when dropsonde was launched	degree_east	sonde_id
	N_p	number of observations used to derive level 3 pressure data		sonde_id, alt
	N_ta	number of observations used to derive level 3 temperature data		sonde_id, alt
	N_rh	number of observations used to derive level 3 relative humidity data		sonde_id, alt
	N_gps	number of observations used to derive level 3 GPS-data		sonde_id, alt
	m_p	method used to derive Level-3 pressure data		sonde_id, alt
	m_ta	method used to derive Level-3 temperature data		sonde_id, alt
	m_rh	method used to derive Level-3 relative humidity data		sonde_id, alt

Continued on next page

Table A.8: Table shows the structure for the Level-3 product, outlining the coordinates, variables and their corresponding descriptions, units and dimensions.

OBJECT	NAME	DESCRIPTION	UNITS	DIMENSION
	m_gps	method used to derive Level-3 GPS-data		sonde_id, alt
	alt_bnds	cell interval bounds for altitude	m	alt, nv

A.5.2.2 *Added Variables*

The complete list of variables, their units and dimensions for Level-3 are provided in Table A.8. The descriptions of variables added in Level-3 are as follows.

Launch Time (`launch_time`)

Level-3 data are of the trajectory type with a single timestamp associated with each sounding, i.e. the launch time. This variable is the same as `launch_time` present in all Level-1 files.

Potential Temperature, θ (`theta`) and Specific Humidity, q (`q`)

For estimating θ, we consider standard pressure, i.e. 1000 hPa. For the estimation of saturated vapour pressure, the method by Hardy (1998) is used with temperature at every altitude level as input and subsequently, specific humidity (q) is estimated. The values of θ and q are estimated from the soundings on their respective, raw vertical grid, before interpolating them on to a common grid.

Platform Name (`platform`)

Although all soundings are in a single file in Level-3, they can still be separated into HALO and P3 sondes, using this variable, which specifies the platform from which the dropsonde was launched. The values of the variable are strings, and have two possible values – "HALO" and "P3".

Interpolated time (`interpolated_time`)

Since time is the independent dimension along which the measurements are made, it is illogical to average or interpolate time along the altitude dimension. Therefore, `time` is not available as a variable from Level-3 onwards. However, for practical purposes, this can be useful information for instance, to compare with remote-sensing instruments on the aircraft. Thus, relying on the high sampling rate and based on the robust assumption that the dropsondes have negligible upward motion, Level-3 includes the variable `interpolated_time`. The variable is computed with linear interpolation, same as for other variables except pressure.

Low Flight Height Flag (`low_height_flag`)

Some of the sondes from the P3 were launched at an altitude of ~3 km when the aircraft was also launching AXBTs. Therefore, these soundings sampled only the lower levels of the atmosphere, over just half of the depth sampled by other P3 sondes, and a third of that of HALO's typical sondes. The `low_height_flag` variable in Level-3 marks sondes that have a launch altitude of less than 4 km, with a value

of 1 and otherwise, 0. This flag is useful to put in to context estimates of integrated quantities such as total column moisture, as well as to act as an easy separator for users who want to look at profiles in the free troposphere.

Number of Measurements in Bin (`N_p`, `N_ta`, `N_rh`, `N_gps` and Bin Method (`m_p`, `m_ta`, `m_rh`, `m_gps`))

The variables `N_p`, `N_ta`, `N_rh` and `N_gps` provide the number of pressure, temperature, relative humidity and GPS measurements, respectively in each altitude bin for gridding. Depending on the values of these `N`-variables, the corresponding cell methods – denoted by the `m`-variables – are provided. For the `m`-variables, possible values are 0, 1 and 2 and stand for no data, interpolation and averaging, respectively.

A.5.3 *Level-4 (Circle Products)*

As discussed in Section A.2.2, the estimation of area-averaged mesoscale properties, such as divergence, was the primary objective behind the sondes' deployment over circular patterns. The Level-4 product provides these circle products as gradient terms estimated by regressing the parameters at each level for a set of sondes comprising a circle. Level-4 also includes terms of divergence, vorticity, vertical velocity and pressure velocity, which are subsequently computed from the gradient terms. The input data are from the gridded dataset in Level-3.

A.5.3.1 *Identifying circles and corresponding sondes*

The flight phase segmentation (FPS) files for HALO (Konow et al., 2021) and for P3 (Pincus et al., 2021) are used for identifying the circles and the dropsondes corresponding to these circle segments. To facilitate ease of working with JOANNE and the FPS files, the circle segments in JOANNE Level-4 have been tagged with the same segment IDs as those in the FPS files. Moreover, the FPS files include a list of dropsondes associated with every flight segment, and this list is comprised of sonde IDs that are the same as that in the JOANNE Level-3 gridded product.

A.5.3.2 *Regression*

Following Bony and Stevens (2019), for any parameter ϕ measured by a dropsonde, assuming that variation at any altitude level is linear in horizontal space and is steady in time, the value at any point can be estimated as,

$$\phi(x,y) \approx \phi_o + \frac{\partial \phi}{\partial x}\Delta x + \frac{\partial \phi}{\partial y}\Delta y, \tag{A.2}$$

where ϕ_o is the meso-scale mean value, Δx and Δy are the eastward and northward distances respectively, from the mean center-point of all observed points included in the regression. Minimising the least-squared errors for the linear regression fit shown in Eq-A.2, would give an estimate of the linear variation in the eastward ($\frac{\partial \phi}{\partial x}$) and northward ($\frac{\partial \phi}{\partial y}$) direction, along with a value for the intercept for the line (ϕ_o), providing the mean

meso-scale value for ϕ. Formulating this least-squares problem for an overdetermined system of k points as,

$$\min_x \|Ax - b\|_2, \tag{A.3}$$

where $A = \begin{pmatrix} 1 & x_1 & y_1 \\ 1 & x_2 & y_2 \\ \dots & \dots & \dots \\ 1 & x_k & y_k \end{pmatrix}$, $x = \begin{pmatrix} \phi_o \\ \partial_x\phi \\ \partial_y\phi \end{pmatrix}$ and $b = \begin{pmatrix} \phi_1 \\ \phi_2 \\ \dots \\ \phi_k \end{pmatrix}$, we solve for x and compute the regression estimates as,

$$x = A^+ b, \tag{A.4}$$

where A^+ is the Moore-Penrose pseudo-inverse. This pseudo-inverse is obtained from the components of singular value decomposition (SVD) of A. If the SVD of A is written as $U \cdot \Sigma \cdot V^T$, then A^+ is estimated from the inverse of the SVD components as $V \cdot \Sigma^+ \cdot U^T$. Here, U and V are unitary matrices, Σ is a rectangular diagonal matrix with A's singular values and Σ^+ is a rectangular diagonal matrix with the reciprocal of A's singular values. We use the `linalg.pinv` function from the numpy Python library (v1.18.3) to calculate A^+.

As a sanity check, we tested the Moore-Penrose pseudo-inverse method of least-squares fitting against the ordinary least-squares fitting by Bony and Stevens (2019), and found no difference between the solutions (not shown). The advantage with incorporating SVD in the regression is that it significantly reduces computing time, because of the availability of vectorized functions in the numpy library.

The Level-4 product includes the eastward (zonal) and northward (meridional) gradients of temperature, pressure, specific humidity as well as u- and v-winds. Derived from these, Level-4 also provides area-averaged meso-scale divergence ($\mathcal{D}$), vorticity (ζ), vertical velocity (W) and pressure velocity (ω), following Bony and Stevens (2019). The dataset also provides the standard error of each of these regressed estimates as ancillaries to the corresponding variables, thus establishing an extent of confidence in the calculation of these meso-scale properties.

Derived variables in Level-4 are at the same vertical grid of 10 m spacing as in Level-3, and the number of sondes regressed at every level is provided as a variable (`sondes_regressed`). If at any level, fewer than 6 sondes have data available, the value for regressed values at that level is set to NaN. This includes data missing due to no data being recorded as well as sondes removed in any of the previous QC steps. Since the number of sondes regressed change at different levels, this causes abrupt, but generally minor fluctuations in integrated products such as pressure velocity and vertical velocity.

All data variables in Level-4 are along the `circle` and `alt` dimension (see Table A.9), and individual sounding data are excluded. The list of sonde IDs included in every circle is included as a variable along dimension `sonde_id`, making it easier to retrieve data for the individual soundings in the circle.

Table A.9: Table shows the structure for the Level-4 product, outlining the coordinates, variables and their corresponding descriptions, units and dimensions. The ancillary variables (with the prefix 'se_') give the standard error for their corresponding variables indicated by the suffix in the name.

OBJECT	NAME	DESCRIPTION	UNITS	DIMENSION
Coordinates	alt	height obtained by integrating upwards the atmospheric thickness estimated from the hypsometric equation	m	alt
	sounding	sonde number		sounding
	circle	circle number		circle
	circle_lon	longitude of fitted circle for all regressed sondes in circle	degree_east	circle
	circle_lat	latitude of fitted circle for all regressed sondes in circle	degree_north	circle
	circle_time	mean launch time of all sondes in circle	seconds since 2020-01-01	circle
	segment_id	unique segment ID		circle
Variables	platform_id	platform which flew the circle		circle
	flight_altitude	mean altitude of the aircraft during the circle	m	circle
	circle_diameter	diameter of fitted circle for all regressed sondes in circle	m	circle
	u	mean eastward wind in circle	$m\ s^{-1}$	circle, alt
	dudx	zonal gradient of eastward wind	s^{-1}	circle, alt
	dudy	meridional gradient of eastward wind	s^{-1}	circle, alt
	sonde_id	unique sonde ID		circle, sounding
	v	mean northward wind in circle	$m\ s^{-1}$	circle, alt
	dvdx	zonal gradient of northward wind	s^{-1}	circle, alt

Continued on next page

Table A.9: Table shows the structure for the Level-4 product, outlining the coordinates, variables and their corresponding descriptions, units and dimensions. The ancillary variables (with the prefix 'se_') give the standard error for their corresponding variables indicated by the suffix in the name.

OBJECT	NAME	DESCRIPTION	UNITS	DIMENSION
	dvdy	meridional gradient of northward wind	s^{-1}	circle, alt
	q	mean specific humidity in circle	kg kg^{-1}	circle, alt
	dqdx	zonal gradient of specific humidity	kg kg^{-1} m^{-1}	circle, alt
	dqdy	meridional gradient of specific humidity	kg kg^{-1} m^{-1}	circle, alt
	ta	mean air temperature in circle	K	circle, alt
	dtadx	zonal gradient of temperature	K m^{-1}	circle, alt
	dtady	meridional gradient of temperature	K m^{-1}	circle, alt
	p	mean air pressure in circle	Pa	circle, alt
	dpdx	zonal gradient of pressure	Pa m^{-1}	circle, alt
	dpdy	meridional gradient of pressure	Pa m^{-1}	circle, alt
	D	area averaged horizontal mass divergence	s^{-1}	circle, alt
	vor	area averaged horizontal relative vorticity	s^{-1}	circle, alt
	W	area averaged vertical air velocity	m s^{-1}	circle, alt
	se_dudx		s^{-1}	circle, alt
	se_dudy		s^{-1}	circle, alt
	se_dvdx		s^{-1}	circle, alt
	se_dvdy		s^{-1}	circle, alt
	se_dqdx		kg kg^{-1} m^{-1}	circle, alt
	se_dqdy		kg kg^{-1} m^{-1}	circle, alt
	se_dpdx		Pa m^{-1}	circle, alt
	se_dpdy		Pa m^{-1}	circle, alt
	se_dtadx		K m^{-1}	circle, alt
	se_dtady		K m^{-1}	circle, alt
	se_D		s^{-1}	circle, alt

Continued on next page

Table A.9: Table shows the structure for the Level-4 product, outlining the coordinates, variables and their corresponding descriptions, units and dimensions. The ancillary variables (with the prefix 'se_') give the standard error for their corresponding variables indicated by the suffix in the name.

OBJECT	NAME	DESCRIPTION	UNITS	DIMENSION
	se_vor		s^{-1}	circle, alt
	se_W		m s^{-1}	circle, alt
	omega	area averaged atmospheric pressure velocity	Pa s^{-1}	circle, alt

A.6 SUMMARY

The EUREC^{4}A field-campaign took place in January-February, 2020 over the North Atlantic trade-wind region. The campaign employed a multitude of platforms measuring a range of atmospheric and oceanographic variables with the objective of understanding shallow clouds and processes that influence them. A core part of the campaign was the deployment of dropsondes to characterise the thermodynamic and dynamic structure of the atmospheric environment. Here, we present JOANNE, the dataset that provides these dropsonde data and additional derived products.

JOANNE presents measurements from 1216 dropsondes launched during EUREC^{4}A by the German research aircraft HALO and the NOAA WP-3D. Dropsondes were primarily released in groups of twelve circumscribing a mesoscale, 223 km diameter, circle centered near 57.7°W, 13.3°N, which we call the EUREC^{4}A-circle. Eighty-five circle patterns were flown with dropsonde launches, seventy-three being flown by HALO over the EUREC^{4}A-circle along patterns that were not biased toward particular meteorological conditions. In addition, sondes were launched on circular flight patterns centered elsewhere, along lawn-mower flight patterns coinciding with AXBT drops, and in a variety of other locations to provide context, or calibration for other measurements. Data presented in JOANNE have been quality controlled to eliminate sondes with no, or partially corrupted data. 51 of the 1216 sondes did not provide usable data, and another 98 provided only partial data and are not included in data products from Level-2 onwards.

A comparison of the HALO dropsondes with radiosondes intensively launched from the R/V Meteor close to the western (upwind) edge of the EUREC^{4}A-circle, and with radiosondes launched from the downwind Barbados Cloud Observatory, suggest a dry-bias. Multiplying relative humidity values by 1.06 appears to largely correct the bias, however due to a lack of physical justification, this correction is not applied to the JOANNE data. We found no evidence of such a bias in the P3 sondes, and the difference seems attributable to different reconditioning procedures applied on the P3 as compared to HALO.

JOANNE is divided in 5 levels of data products, with increasing order of processing and product retrieval. Level-0 comprises the raw measurement data from the dropsondes collected by AVAPS on the aircraft. Level-1 provides data processed using ASPEN – a state-of-the-art tool for processing raw dropsonde data files. Level-2 consists of individual sounding files that passed through the QC check, but with redundant quantities removed and no derived variables added. Level-3 provides the data after gridding them to a uniform vertical spacing of 10 m, along with derived variables such as potential tempera-

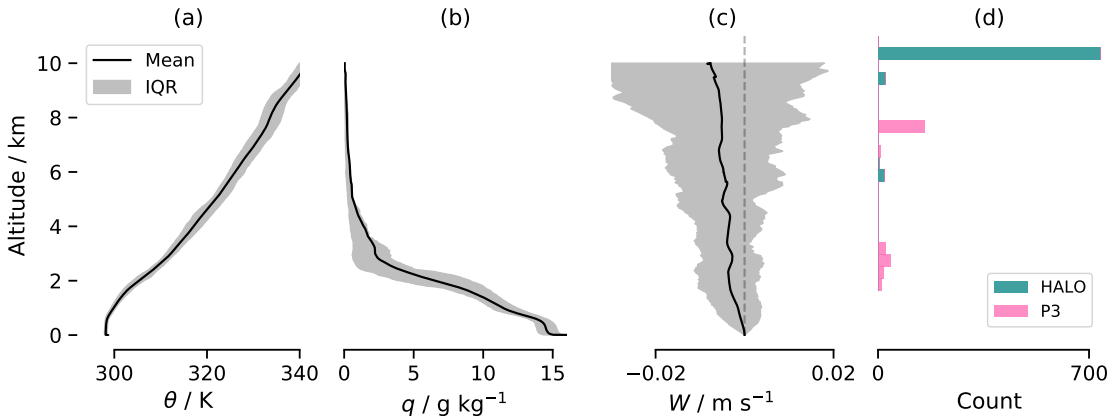

Figure A.6: Vertical profiles of mean potential temperature (a) and specific humidity (b) from measurements of HALO and P3 sondes. (c) shows vertical profile of mean vertical velocity from estimates of HALO's EUREC^{4}A-circle measurements. Shaded regions in (a)-(c) show interquartile range (IQR) of the respective properties. (d) shows the histogram for the flight altitude of dropsondes launched from both platforms.

ture and specific humidity. Level-4 contains the circle products which are area-averaged, meso-scale variables such as gradients, divergence, vorticity and vertical velocity. The vertical profiles and histogram of flight altitude for dropsonde launches shown in Fig. A.6 provide an overview for a subset of the atmospheric observations that JOANNE provides. While reaffirming the typical steadiness in the thermodynamic structure of the trades, JOANNE also confirms the high variability in meso-scale vertical motion found by Bony and Stevens (2019) compared to the mean over longer time-scales.

A.7 CODE AND DATA AVAILABILITY

The JOANNE dataset (George et al., 2021b) described in this manuscript is freely available at AERIS (https://doi.org/10.25326/221). The software used to process the dropsonde data and create JOANNE is also publicly available (https://doi.org/10.5281/zenodo.4746313; George (2021))

Acknowledgments. This research was made possible through generous public support provided to, and managed by, the Max Planck Society (DE), DFG HALO SPP 1294 (DE), CNRS (FR) and NOAA (USA). The project also received funding from the European Research Council (ERC) under the European Union's Horizon 2020 research and innovation programme (EUREC4A Advanced Grant NO. 694768) and from the French AERIS research infrastructure. A great number of people contributed to the launching of the sondes, as recognized in the EUREC^{4}A overview paper. In particular, the authors thank Friedhelm Jansen for his organization and provision of the sondes, Mario Mech and Lutz Hirsch for logistical and technical support, and Angela Gruber for administrative support. Aboard HALO, in addition to the authors, Felix Ament, Jude Charles, Tim Cronin, André Ehrlich, Kerry Emanuel, Florian Ewald, David Farrell, Marvin Forde, Silke Groß, Martin Hagen, Marek Jacob, Theresa Mieslinger, Ann Kristin Naumann, Theresa Lang, Veronica Pörtge, Sabrina Schnitt, Eleni Tetoni, Ludovic Touze-Peiffer, Jessica Vial, Raphaela Vogel, Antone Wiltshire, Allison Wing and Kevin Wolf contributed to the launching of sondes. Akshar Patel launched the sondes from the P3. The authors are also indebted to the ground and flight crew of both aircraft as well as the civil aviation facility and air traffic

control for their efforts to facilitate the measurements. Special thanks to Holger Vömel for advice on the possible cause behind the HALO dry bias. GG thanks Anna Lea Albright, Florent Beucher, Xuanyu Chen, Thibaut Dauhut, Geiske de Groot and Louise Nuijens in addition to some names already mentioned for feedback on early versions of the dataset and Ann Kristin Naumann for her comments on the manuscript.

B

OBSERVED IMPACT OF MESO-SCALE VERTICAL MOTION ON CLOUDINESS

The work in this appendix has been published as:

George, Geet, Bjorn Stevens, Sandrine Bony, Marcus Klingebiel, and Raphaela Vogel. "Observed impact of meso-scale vertical motion on cloudiness". (2021). *Journal of the Atmospheric Sciences*. doi:10.1175/JAS-D-20-0335.1.

The contributions of the authors to this paper are as follows:

GG did most of the formal analysis, investigation and all of the writing, and was involved in the concept design. BS and SB designed the concept and methodology of the study, as well as supervised the analysis. MK and RV helped with the analysis and investigation. RV was also involved with the concept design. All authors reviewed for GG several rounds of draft writing.

Observed impact of meso-scale vertical motion on cloudiness

Geet George[1], Bjorn Stevens[1], Sandrine Bony[2], Marcus Klingebiel[1,*], Raphaela Vogel[2]

[1] Max Planck Institute for Meteorology, Hamburg, Germany
[2] LMD/IPSL, Sorbonne University, CNRS, Paris, France
* Current affiliation: Leipzig Institute for Meteorology (LIM), University of Leipzig, Leipzig, Germany

Received: 3 Nov 2020 / Accepted: 5 May 2021 / Published online: 17 May 2021

ABSTRACT

We use estimates of meso-scale vertical velocity and co-located cloud measurements from the second *Next-Generation Aircraft Remote Sensing for Validation* campaign (NARVAL2) in the tropical North Atlantic to show the observed impact of meso-scale vertical motion on tropical clouds. Our results not only confirm previously untested hypotheses about the role of dynamics being non-negligible in determining cloudiness, but go further to show that at the meso-scale, the dynamics has a more dominant control on cloudiness variability than thermodynamics. A simple mass-flux estimate reveals that meso-scale vertical velocity at the sub-cloud layer top explains much of the variations in peak shallow cumulus cloud fraction. In contrast, we find that thermodynamic cloud-controlling factors, such as humidity and stability, are unable to explain the variations in cloudiness at the meso-scale. Thus, capturing the observed variability of cloudiness may require not only a consideration of thermodynamic factors, but also dynamic ones such as the meso-scale vertical velocity.

Significance Statement. Knowing how low clouds link to atmospheric circulation over a few hundred kilometers, will reduce current uncertainties in the sensitivity of earth's climate to warming. Such investigations have previously been limited by lack of circulation measurements at the meso-scale. However, using measurements now available from a recent field campaign over the tropical North Atlantic along with cloud measurements, we demonstrate how atmospheric vertical motion especially in the lower layers can influence the extent and structure of clouds. We find that the kinematics have a more dominant control on low-level cloudiness than conventionally studied thermodynamics. Our results show why it is important to focus attention to the circulation to improve our understanding of the variability in cloudiness.

B.1 INTRODUCTION

Understanding how low-level clouds respond to their environment can help reduce uncertainties in climate sensitivity estimates (Bony and Dufresne, 2005; Zelinka et al., 2020). Tropical environmental conditions on the meso-scale (20-200 km) can change within a few hours to a day, whereas over the large-scale, $O(1000\ \text{km})$, conditions can be expected to persist for multiple days. What controls cloudiness at the meso-scale is not as well-investigated as what controls them at the large-scale. This shortcoming is mainly due to a limited understanding of how the atmospheric state varies at the meso-scale, especially in terms of circulation, which in turn can be attributed to an absence of observations at such scales. Nevertheless, the clouds-circulation coupling from the cloud-scale to the large-scale is thought to be important for the strength of cloud feedbacks and consequently, for projecting the future climate (Bony et al., 2015). In this study, we aim to provide insights into how atmospheric circulation can influence tropical cloudiness at the meso-scale.

Predicting cloudiness for an air parcel *a priori* is simple, and can be linked directly to the occurrence of saturation. In the tropical boundary layer, saturation is primarily associated with ascending air, and therefore, it is necessary to understand what determines the intensity, the spatial distribution and the vertical extent of coherent ascents. This amounts to determining what controls the shallow convective mass flux. Vogel et al., 2020 show that mass flux is regulated by environmental factors, primarily the meso-scale atmospheric vertical motion at cloud base. This suggests that clouds depend directly on meso-scale circulation features, and that the connection between the two may need to be accounted for when predicting cloudiness.

To study the influence of circulation on clouds, observational challenges have compelled previous investigations to use reanalysis data, and since these are more reliable over larger scales of time and space, such studies focus on the large-scale (e.g. Bony et al., 2004; Stevens et al., 2007; Myers and Norris, 2013, and others). An unequivocal finding from these studies is that pressure velocity (ω) in the free troposphere (e.g. at 500 hPa, 700 hPa, etc.) can be used to separate cloudiness into regimes of shallow convection (subsidence) and deep convection (ascent). Additionally, if lower-tropospheric stability (LTS) is considered, one can classify the shallow convection regimes into stratocumuli (stronger inversion) and trade-wind cumuli (weaker inversion), as shown by Medeiros and Stevens, 2009. Along with stability and kinematic factors such as ω, clouds are also shown to be strongly associated with other thermodynamic factors such as relative humidity (Slingo, 1987) and sea surface temperature (SST; Qu et al., 2015), which themselves are influenced by kinematic factors (or motion field parameters).

Klein, 1997 and Brueck et al., 2015, however, show that on scales of 5-days or shorter, these associations weaken significantly. Moreover, Nuijens et al., 2015b show that while

humidity, lapse-rate, surface wind-speed and ω at 850 hPa (ω_{850}) together explain close to 56% of the monthly variance in cloud cover in the trade-wind region, they account for only 24% of the daily variance. These results indicate that factors controlling clouds on longer time and larger space scales hold lesser influence at the shorter (hours to day) and finer (20-200 km) scales, and that other factors might be more dominant in controlling cloudiness therein. The importance of determining these day to day or scene-scale controls is further highlighted by the finding of Nuijens et al., 2015a, that more than 50% and 75% of the variability observed in low-level cloudiness occurs over time-scales shorter than 1 and 5 days, respectively.

The influence of dynamics on clouds has been investigated by several studies, but these were mainly restricted to stratocumulus regimes and have only used reanalysis products to characterise the environment, especially circulation parameters. Mauger and Norris, 2010, using a Lagrangian framework, show that factors such as large-scale divergence ($\mathcal{D}$) at the surface and ω_{700} have a more instantaneous control (0-12 h) on stratocumulus clouds compared to thermodynamic factors like LTS and SST (12-48 h). They also find that strong subsidence at 700 hPa leads to a reduction in cloud fraction. Myers and Norris, 2013 similarly show that for constant inversion strength, stratocumulus cloud fraction increases with weakening subsidence. Szoeke et al., 2016 find a similar effect as in both previous studies on the sub-daily time scale, wherein clouds away from the stratocumulus regimes increase in amount with ascent in the free troposphere (ω_{700}). These aforementioned findings imply that cloudiness might be enhanced by low-level convergence at the meso-scale – a hypothesis currently lacking observational evidence for shallow cumulus clouds. Moreover, Stevens and Brenguier, 2009 point out that in contrast to thermodynamic factors, the role that dynamic factors such as divergence play in controlling cloudiness is uncertain and far from trivial, particularly on finer scales which are less strongly coupled to the large-scale thermodynamic environment. Thus, for determining tropical cloudiness at such scales, it appears necessary to test the hypothesis about low-level convergence enhancing cloud fraction and to understand how clouds are controlled by the meso-scale dynamics. The long-standing challenge though, has been in measuring said dynamics.

Some field campaigns such as the *Barbados Oceanographic and Meteorological Experiment* (BOMEX, Holland, 1970) and the *Atlantic Trade-wind Experiment* (ATEX, Augstein et al., 1974) have successfully measured divergence previously. But their small number of measurement points over the large-scale makes it difficult to establish the veracity of these measurements, particularly on the meso-scale. These were also best constrained by large-scale budgets on much larger space and time scales than would be relevant for the meso-scale. However, Bony and Stevens, 2019, using recent measurements from the second *Next-Generation Aircraft Remote Sensing for Validation* campaign (NARVAL2; Stevens et al., 2019a), demonstrate that area-averaged meso-scale $\mathcal{D}$ and ω can be measured using horizontal wind observations from dropsondes launched along a circular path. With successive measurements within the same air masses and confirmation from high-resolution simulations, they show that the NARVAL2 vertical motion estimates are indeed ones that can be confidently used at the meso-scale, which we aim to study here.

The vertical motion estimates and the collocated cloud measurements from NARVAL2 make it possible to investigate shallow cumulus clouds in their immediate environment, where both the thermodynamics and dynamics are well-characterised. We exploit this opportunity and study how ω at different levels in the atmosphere (i.e. in the moist layer, at 700 hPa and 500 hPa) controls shallow cloudiness differently, thus providing insight into how the circulation influences cloudiness at the meso-scale.

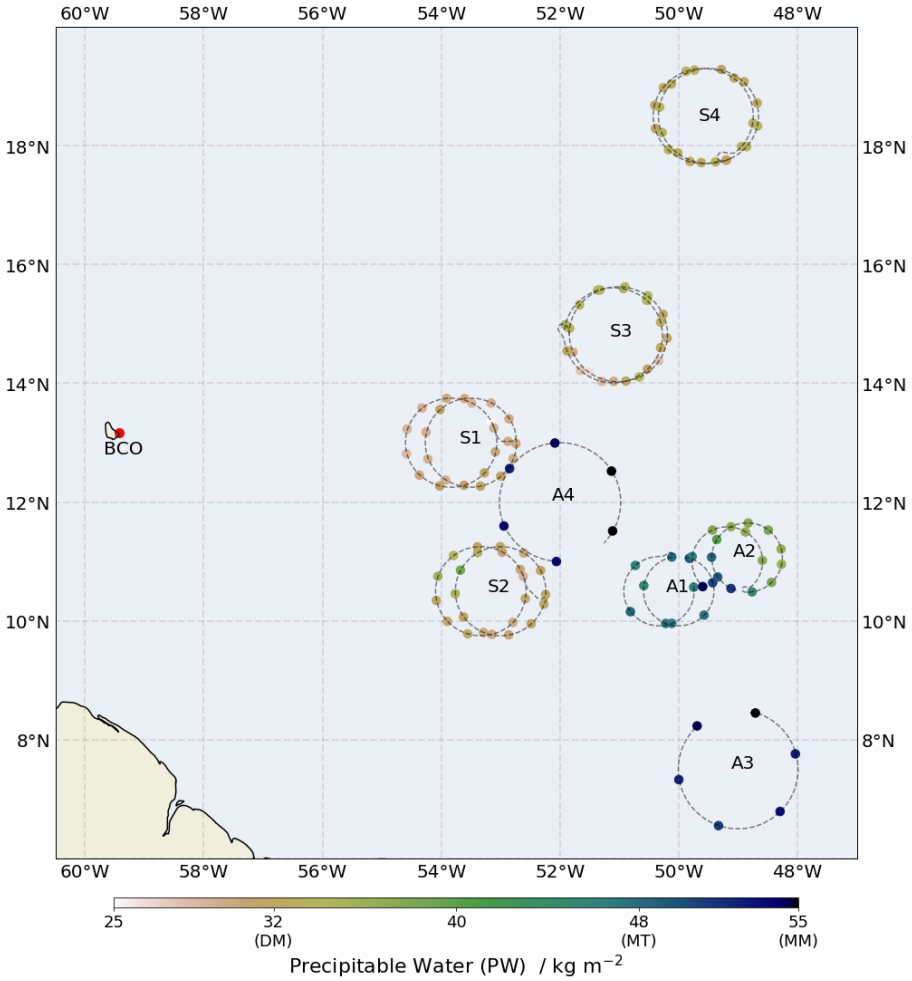

Figure B.1: Markers show dropsonde location for the different circles throughout NARVAL2, and are connected by the flight path during the circles. The marker colors indicate PW retrieved from the respective sondes. The red marker in the west shows the location of BCO. The colorbar for PW indicates the labels of dry mode (DM), moist mode (MM) and the moist threshold (MT), used to categorise the circles (refer to the text in Section B.2B.2.2).

The structure of the paper is as follows. We give a short description of the data used in Section-B.2, along with the methodology of their analyses. In Section-B.3, we provide a quantative picture of the cloudiness sampled during the campaign. This is followed by a discussion of associations between cloudiness and meso-scale environmental factors in Section-B.4. Here, we look at the impact that thermodynamics and dynamics have on cloudiness, and test if ω can potentially be used as a predictor of cloudiness. In Section-B.5, we summarise our findings, provide implications thereof and give an outlook for future studies.

B.2 DATA AND METHODOLOGY

B.2.1 *Circle environments*

The NARVAL2 campaign took place in August 2016 over the tropical North Atlantic – east of Barbados – and included ten research flights (RF) flown with the *High Altitude and Long Range* aircraft (HALO, Stevens et al., 2019a). Five of these flights included segments flown

in circular patterns with a mean diameter of ~175 km (circles, hereafter), along which dropsondes were launched approximately every 4-6 minutes. One of these circles during research flight RF10 was located in the extra-tropics at about 35°N, and is excluded from the study. Data from the remaining eight circles (a total of 137 dropsondes) form the basis for this study. Their location and timing is summarised by Fig. B.1 and Table B.1, respectively. Circles other than those during RF07 were flown in pairs of a clockwise and an anticlockwise round each. Here, we use the term 'circle' to mean these circle pairs, unless specified otherwise. Stevens et al., 2019a provide more information about the campaign and the instruments employed for measurements, and the circle flight strategy is explained in detail by Bony and Stevens (2019).

Vaisala RD-94 dropsondes were used during the campaign (refer to Wang et al., 2015 for details). For processing the dropsonde raw data, we use the *Atmospheric Sounding Processing Environment* (ASPEN), version 3.3-297 software and interpolate the measurements to a uniform 10 m vertical grid. These processed data are used to estimate kinematic parameters such as $\mathcal{D}$, ω and vertical velocity (W) following Bony and Stevens (2019), as well as thermodynamic parameters such as static energy, precipitable water (PW), free tropospheric humidity (FTH), surface wind speed, lifting condensation level (LCL), LTS, inversion height and surface fluxes. PW and FTH are estimated as column water vapour from surface and from 700 hPa level, respectively, with the upper limit of the profile set to 5850 m, to be consistent with the lowest-flown circle. The surface wind speed is estimated as the mean of dropsonde measurements in the 50 m closest to the surface. We estimate the LCL using values of pressure, temperature and humidity averaged over the bottom 200 m and follow the method by Bolton, 1980. LTS is defined as the difference between the potential temperature at 700 hPa and that at surface (10 m), following Klein and Hartmann, 1993. For the inversion height, we use the height at which the squared Brunt-Vaisala frequency (N^2) has its first local maximum from the surface.

To estimate surface fluxes, we use dropsonde measurements of humidity, temperature and wind speed at 20 m altitude, and apply the Coupled Ocean–Atmosphere Response Experiment (COARE) bulk flux algorithm version 3.6 as detailed in Fairall et al., 2003 and Edson et al., 2013. For SST, we use the nearest values from the European Centre for Medium-Range Weather Forecasts (ECMWF) reanalysis product (ERA5; CDS, 2017; Hersbach et al., 2020) at 0.25° horizontal and 1 h temporal resolution.

B.2.2 *Classifying the circles*

The NARVAL2 circles sampled both deep and shallow convection. Here we refer to circles with deep convection and with profiles relatively closer to saturation as *Active* circles (A-circles) and the circles with a substantially drier atmosphere and shallow convective activity as *Suppressed* circles (S-circles).[1] We use mean PW of the circles (see Table B.1) as a basis of classification. Mapes et al. (2018) set a PW moist threshold (MT) of 48 kg m^{-2} for deep convection. Their study also confirms the well-known bimodality in the distribution of tropical PW, and we associate their modes at lesser PW (~32 kg m^{-2}; dry mode (DM)) and at greater PW (~52 kg m^{-2}; moist mode (MM)) with the A and S-circles, respectively. Note that the PW values in Mapes et al. (2018) were taken for the moisture in the entire atmospheric column, whereas the values here are for profiles only up to 5850 m, as

[1] In boreal winter, we don't expect deep convective regimes in this area, and active situations might thus be associated with *disturbed* regimes and termed as such, whereas the more suppressed conditions are the *undisturbed* regimes. This is mentioned as a point of clarification to distinguish them from the corresponding terms 'active' and 'suppressed', used for the respective regions during the summer.

explained in Section B.2.1. For the circles with the moistest free troposphere (A3 and A4), the difference between estimating PW upto 5.85 km and upto flight altitude (9 km) is ~5%, while for all S-circles, this difference is ~1% or lesser. This confirms the general understanding about moisture in the trades, that there is very little moisture above 6 km. Therefore we use the values from Mapes et al. (2018) as is, without any substantial impact on our separation of deep and shallow convection regimes.

Placing the NARVAL2 circles in the context of the above mentioned modes, we identify circles of RF07 as A-circles (A3 & A4) and those of RF03 and RF06 as S-circles (S1-S4), since their PW values match closely with the dry and moist modes, respectively. For the circles of RF02, this classification is a bit more delicate. Flight reports from the campaign confirm that they sampled the edge of deep convection areas, but in doing so also extended across air-mass boundaries to include dry air masses. Thus, although PW values for some dropsondes in the RF02 circles are below the moist threshold (see Fig B.1), we classify them as A-circles (A1 & A2). In the nomenclature of the circles, the digits following the capitalised letters indicate the chronological sequence of the circles in their respective groups.

B.2.3 *Quantifying cloudiness*

B.2.3.1 *Airborne radar and microwave measurements*

To quantify cloudiness, we use the unified dataset by Konow et al. (2019) for measurements from the *HALO Microwave Package* (HAMP; Mech et al., 2014), which includes microwave radiometers and a 35 GHz cloud radar, all looking nadir from the aircraft. As we focus here on low-level clouds, we also extract profiles of shallow cumulus clouds from the HAMP radar, with a cloud mask developed by segmenting the radar cloud data into individual two-dimensional cloud objects along time and height, which we refer to here as the Konow mask. All objects derived from the Konow mask with base below 1 km and top below 4 km are classified as shallow cumulus (ShCu) clouds. We estimate the fraction of radar echoes >-50 dBZ as a proxy for cloud fraction (CF) for the ShCu cloud objects as well as for all hydrometeors detected by the radar, and call them CF_{ShCu} and CF_{total}, respectively.

We also use estimates of liquid water path (LWP) and rain water path (RWP) from HAMP measurements by Jacob et al., 2019 to quantify cloud activity and precipitation, respectively. For LWP and RWP, only values > 50 g m^{-2} and > 1.5 g m^{-2}, respectively are considered for both mean and fractions (see Table B.2). This filter is to ensure that very low values that are likely noise are kept out of the estimation.

B.2.3.2 *Airborne lidar measurements*

We also quantify cloudiness with the nadir-looking WALES lidar (*Water-vapor Lidar Experiment in Space*; Wirth et al., 2009) on board HALO, from which estimates of cloud top height (CTH) are retrieved by Gutleben et al., 2019, by setting a fixed threshold of 20 for the backscatter ratio at the 532 nm channel. The cloud cover over the flight path is estimated by calculating the fraction of lidar profiles that encountered a cloud from the total number of profiles. CTH values are not available for circles in RF02. For the rest of the circles, lidar coverage time exceeded 97% of the circle duration.

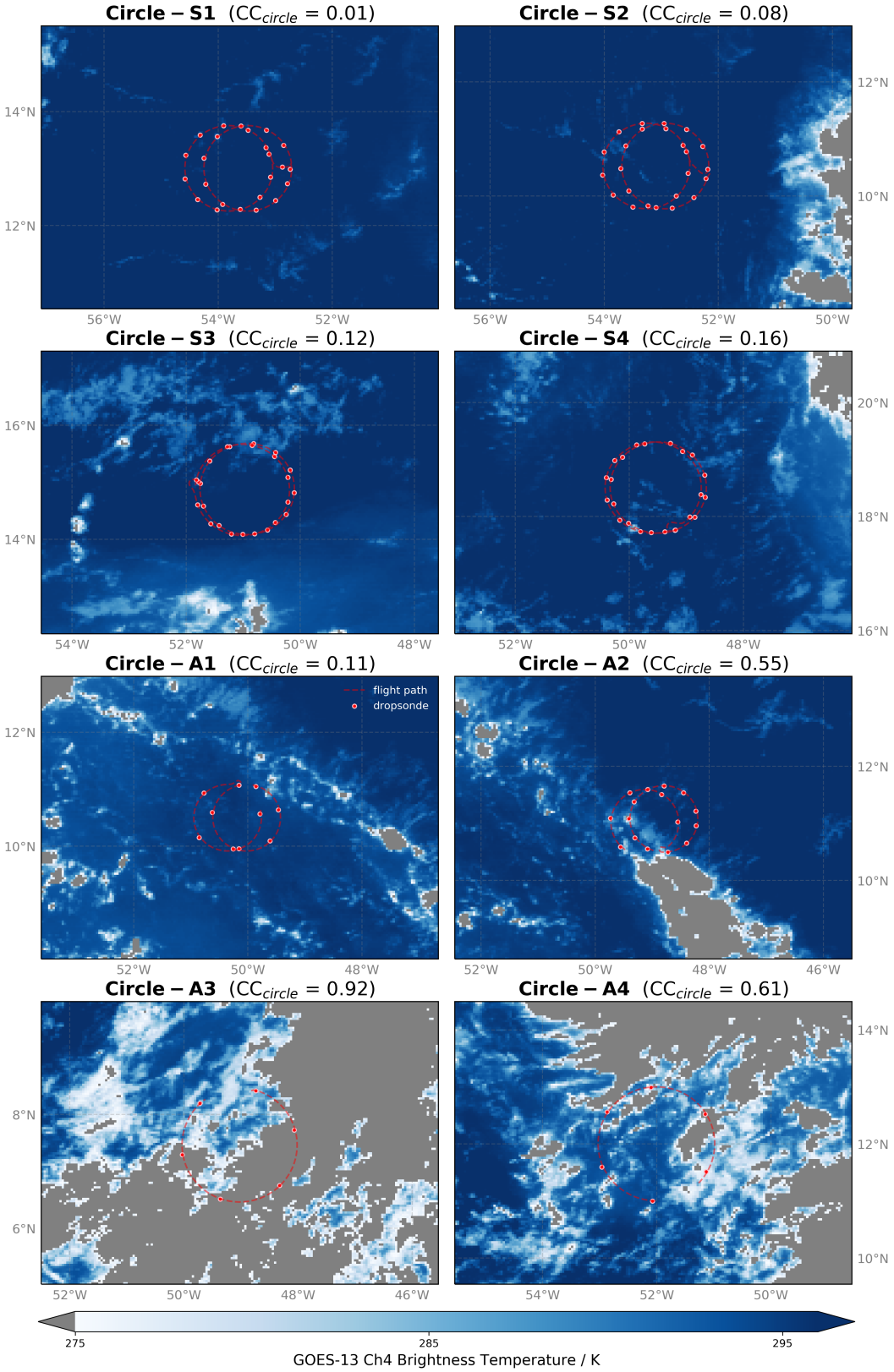

Figure B.2: The GOES-13 Channel-4 brightness temperature values are plotted for all circles, with the upper and lower limit on the colorbar being the cloud detection threshold and indicator of deep convection, respectively. The red markers and lines show the dropsonde launch locations and the flight path, respectively. The time of satellite observation is the hour nearest to the circle mean time and the circle locations are shifted accordingly, following the mean wind. The CC$_{circle}$ values over every box indicate the cloud cover within the circle area.

B.2.3.3 *Satellite measurements*

Since the radar and lidar measurements quantify clouds only over the circumference of the circle, we rely on satellite measurements to look at the cloudiness within the circle area (see Fig. B.2). Hourly measurements at ~4 km (0.04°) horizontal resolution from *Gridded Satellite* (GridSat) from the *Geostationary Operational Environmental Satellite Program - 13* (*GOES-13*) *for the Western Hemisphere* (GridSat-GOES) v01 (Knapp, 2017) are used.

We follow the method of Benner and Curry, 1998 to select cloudy pixels from satellite images using threshold values for Channel-4 (brightness temperature from 11 μm channel) and Channel-1 (reflectance from 0.6 μm band) for all circles. Since their method is applicable only to scattered cloudiness, such as in S-circles, we take the mean of the Channel-4 thresholds for all S-circles, and apply this as a fixed threshold (295.59 K) across all circles to determine cloudy grid points and thus cloud cover (CC) in the circle area. This method works well under the assumption that the SST and lifting condensation level (LCL) temperatures do not vary too much across the circles. Unlike the average Channel-4 threshold, the Channel-1 thresholds are still estimated individually for all circles. The cloud cover we estimate from satellites is only for the grid points that are completely within the circle or are overlapping the edges of the circle fitted to the dropsonde launch locations.

B.2.3.4 *Cumulative cloud cover profiles*

Since the lidar and satellite cannot see past cloud tops, the cloud cover profiles determined by the lidar and satellite are shown as cumulative profiles (see Fig. B.3), with values increasing as altitude decreases, and the maximum value giving the total cloud cover for the circle area. For the satellite, since cloud detection is based on brightness temperatures and since these are not a monotonic function of height, we fit a mean temperature profile to altitude for every circle, by applying an isotonic linear regression (non-increasing with height) to the respective circles' dropsonde temperature measurements.

B.2.4 *Sampling scale*

The above-mentioned environmental and cloud parameters are provided in Table B.1 and Table B.2, respectively. The average lateral drift in the sondes was ~5 km in the direction of the mean flow, and hence, the displacement of the circle along the vertical profile can be considered negligible in terms of both the remotely-sensed clouds and the environmental parameters sampled by the dropsondes. Also, since every round in a circle took around 45 minutes to 1 hour, the environments and cloudiness of the circles characterised here should be taken as representative for the circles at a time-scale of 1-2 hours. Along with this time-scale, the circles' average diameter of ~175 km also fits well with our objective of studying clouds and the environment at the meso-scale of ~20-200 km, which Orlanski (1975) calls the *meso-β* scale.

B.3 CHARACTERIZING THE CLOUDINESS

In this section, we sketch out what the clouds looked like for the different circles. For this, we resort to the aforementioned satellite measurements (Figs. B.2 & B.3), the radar measurements (Figs. B.3, B.4 & B.5) and the lidar measurements (Fig. B.3).

Flight ID	RF03		RF06		RF02		RF07	
Circle ID	S1	S2	S3	S4	A1	A2	A3	A4
Date (08-2016)	12	12	19	19	10	10	22	22
Diameter (km)	167.37	168.08	177.37	176.99	133.24	131.46	221.42	221.62
Time (UTC)	13:54	17:42	14:33	17:57	14:07	17:44	15:37	19:07
Total Sondes	12+12	12+12	12+12	13+11	6+6	11+6	6	6
Flight Altitude (m)	9024	9003	9035	9014	5894	5878	9011	8913
PW ($kg\ m^{-2}$)	29.4 (1.5)	31.4 (2.2)	31.0 (2.5)	32.1 (0.8)	46.9 (1.5)	40.2 (6.0)	50.1 (1.8)	52.3 (2.0)
FTH ($kg\ m^{-2}$)	4.3 (0.5)	4.5 (0.3)	3.0 (1.2)	1.9 (0.8)	8.4 (1.4)	4.5 (2.1)	12.4 (0.8)	10.1 (1.6)
LTS (K)	14.1 (0.4)	13.3 (0.3)	14.7 (0.2)	13.5 (0.2)	13.0 (0.3)	13.5 (0.4)	11.3 (0.4)	13.6 (0.8)
Surface Wind ($m\ s^{-1}$)	6.2 (0.4)	7.8 (0.3)	5.1 (0.2)	6.5 (0.2)	4.7 (0.3)	8.7 (0.4)	3.3 (0.4)	1.8 (0.8)
Latent Heat Flux ($W\ m^{-2}$)	146.8 (26.7)	199.2 (26.5)	102.3 (19.8)	118.4 (16.2)	89.8 (13.2)	145.2 (39.4)	97.4 (57.7)	40.3 (7.7)
SST (°C)	28.4 (0.2)	29.4 (0.2)	27.9 (0.2)	28.1 (0.0)	29.0 (0.3)	28.8 (0.3)	29.8 (0.3)	28.7 (0.3)
LCL (m)	795	865	730	675	590	590	720	510
Inversion Height (m)	1390	1620	1650	1630	1400	1410	680	1630

Table B.1: The table provides details of the circles together with mean values of selected thermodynamic parameters. Units are given in parentheses following parameter names. Total sondes are the number of sondes launched in the circle, for the clockwise (first number) and the anticlockwise (second number) rounds, respectively. Parameter definitions are given in Section B.2.1. Note that due to the lack of a steady inversion, the inversion height value for A3 is unusually low and cannot be considered as an estimate for the true inversion height, like for the other circles. Numbers in parentheses are standard deviations.

Flight ID	RF03		RF06		RF02		RF07	
Circle ID	S1	S2	S3	S4	A1	A2	A3	A4
Satellite CC (%)	1.2	7.8	11.9	16.0	11.4	55.1	92.5	61.1
Lidar CC (%)	11.9	17.8	17.5	17.4	-	-	52.3	47.1
Radar CC (%)	3.4	2.9	3.4	7.1	4.1	28.2	37.2	25.6
Peak ShCu CF (%)	0.3	1.3	0.7	4.0	1.5	10.5	1.0	0.8
RWP ($g\ m^{-2}$)	7.0	2.9	2.7	10.1	2.5	20.7	8.5	15.2
RWP Fraction (%)	0.0	0.1	0.1	0.8	0.1	3.4	2.4	4.4
LWP ($g\ m^{-2}$)	165.1	132.3	129.8	200.1	126.3	201.1	105.4	207.9
LWP Fraction (%)	0.8	2.4	1.7	5.3	1.2	14.5	21.6	11.6
ShCu Top (m)	1254.0	1422.0	1410.0	1512.5	1211.2	1158.5	1496.0	1135.4
ShCu Base (m)	834.0	858.0	690.0	578.3	611.2	613.0	746.0	676.2

Table B.2: The table provides details of the cloudiness parameters for the circles. Units are given in parentheses following parameter names. All parameters that do not have a '%' unit show mean values for the circle. Details of how the parameters are estimated are provided in Section B.2.3.

B.3.1 *Clouds in the S-circles*

From Fig. B.2, we see that circles S1 and S2 are part of a much larger, relatively homogeneous, cloud-free area, and thus have low CC_{circle} values. S3 is also mostly cloud-free, albeit with some bands of stratiform clouds at the northern and northeastern edges and a blanket of dust present towards the south - both also confirmed by visual testimony in the flight reports.

Both satellite and radar measurements show greater cloudiness in circle S4 compared to the other three S-circles, in terms of CC_{circle}, CF_{ShCu} and CF_{total} (see Figs. B.2-B.4 and Table B.2). A perception of how active the clouds in these circles were can be derived from the LWP and RWP estimates. Comparing the S-circles in Table B.2 and Fig. B.4, we see that S4 has more instances of relatively high LWP, and that its mean LWP is much higher than that of the other S-circles. The RWP also indicates that S4 has a greater number of precipitating clouds (large RWP fraction), with an overall higher intensity (larger mean

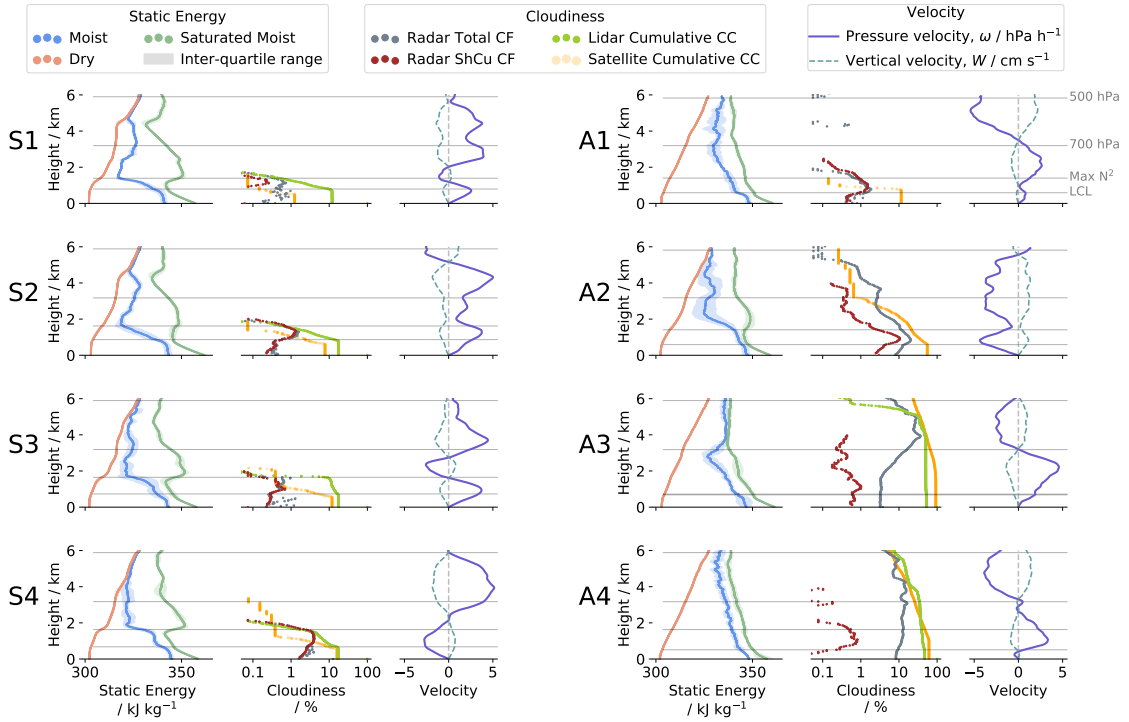

Figure B.3: For all circles, the static energy profiles (left), cloudiness profiles (centre) and the meso-scale vertical motion profiles (right) are shown. The grey lines, cutting horizontally across all profiles are, from bottom to top, levels of LCL, maximum N^2, 700 hPa and 500 hPa, for the particular circle. The static energy values, pressure velocity (ω) and vertical velocity (W) are determined from dropsonde measurements, and the cloudiness profiles are obtained from the HAMP radar, WALES lidar and the GOES satellite, as per the legend.

RWP). Since the HAMP radar detects even low amounts of rain (Jacob et al., 2020), it would be fair to assume from Fig. B.4, that S4 was the only S-circle along which any noticeable precipitation was measured.

In terms of lidar cloud cover (see Table B.2), the S-circles do not vary much from each other except S1, which shows smaller values. This difference in cloudiness between the radar and lidar can be mostly explained by the difference in LWP values among the S-circles. Jacob et al., 2020 show that the HAMP radar misses more than 75% of the clouds detected by the WALES lidar, when LWP < 50 g m^{-2}. Thus, the lower LWP values of S1 through S3 result in the radar cloudiness deviating greatly from that of the lidar, as seen in the profiles in Fig. B.3. Additionally, for S3, the lidar cloud cover also accumulates a distinct offset from the radar CF at an altitude of around ~1.7 km. This can be attributed to the presence of the stratiform clouds in the northern part of the circle, which were too shallow for the radar to detect. In contrast to the other S-circles, for S4 the radar is able to detect a larger proportion of the clouds detected by the lidar, indicating that most of the clouds in S4 were active clouds with relatively larger LWP.

The satellite cloud cover profile in Fig. B.3 shows that S4 had some clouds with tops reaching to ~3.5 km which are much higher than cloud tops in the other S-circles, which had maximum values of about 2 km. The general agreement between the satellite cloud cover and the radar measurements provides confidence that the airborne measurements were not simply sampling discrepancies. Thus, over several measures of cloudiness such

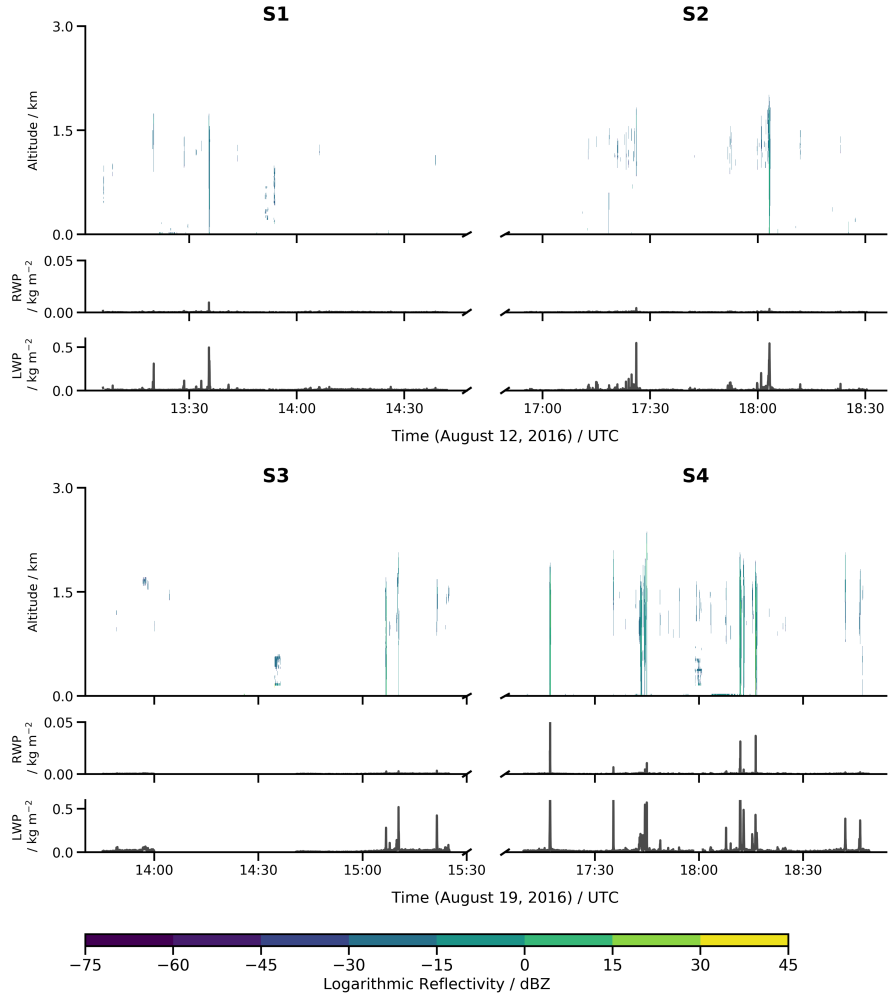

Figure B.4: Radar reflectivity (top), rain water path (RWP; middle) and liquid water path (LWP; bottom) are shown for all four S-circles.

as occurrence (CF and CC), activity (LWP and RWP) and vertical extent (cloud top height), we find that circle S4 is significantly 'cloudier' than the other three S-circles.

B.3.2 *Clouds in the A-circles*

A-circles show higher cloud tops (see grey regions in Fig. B.2), and although A1 does not have any within the circle area itself, it is surrounded by similar spurts of high cloud tops. The HAMP radar gave echoes for parts of these cloud systems from surface upto the flight altitude (see Fig. B.5), thus indicating that the high cloud tops we see from the satellite were indeed parts of deep convective clouds and their attached anvils. The greater spatial coverage (CC_{circle}) and higher cloud tops in A-circles (with the exception of A1) are in contrast to the S-circles, which are relatively cloud-free and have shallow clouds, with tops not exceeding brightness temperatures of ~288 K.

The contrast between S- and A-circles is also visible in cloud fraction profiles from the radar (Fig. B.3). The peak low-level cloud fraction in the S-circles is at most one-sixth of that of the A2-A4 circles, and this could partially be explained also by the high LWP values obtained for the latter set of circles (see Fig. B.5). The cloud fraction not only varies in amount, but also in its vertical structure. No cloudiness is observed above ~2 km, for

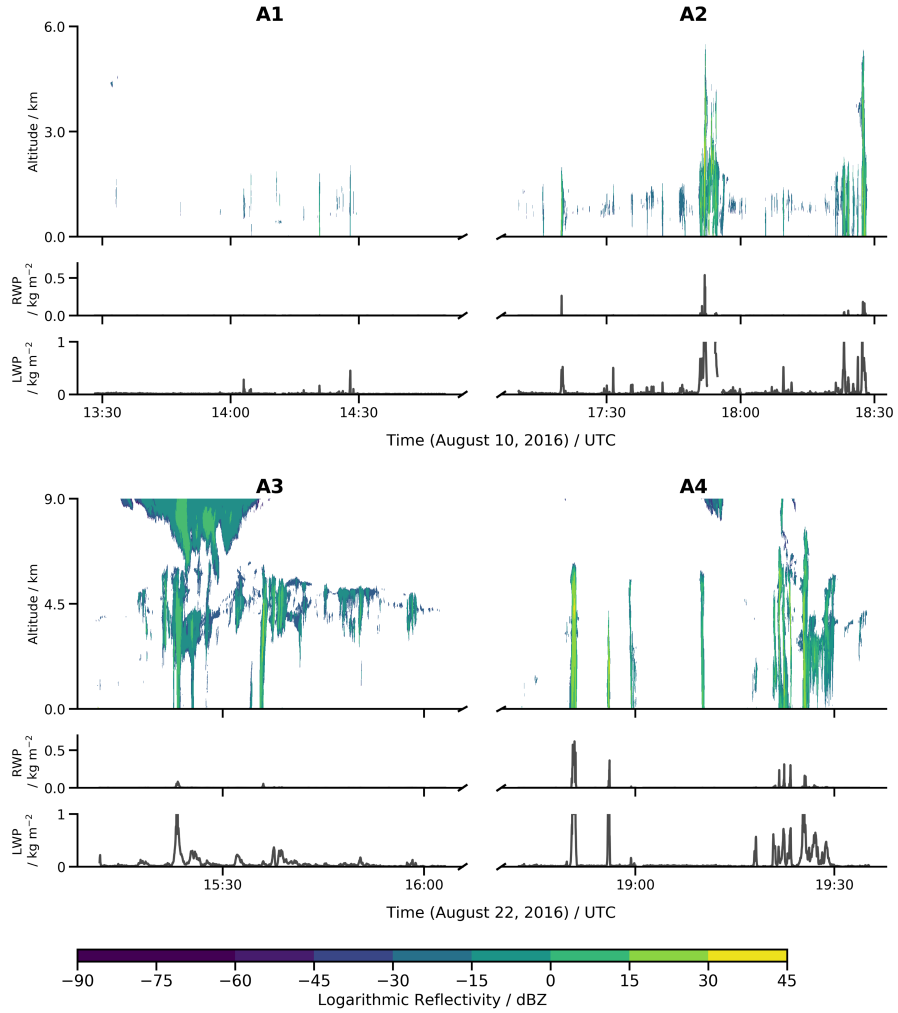

Figure B.5: Radar reflectivity (top), rain water path (RWP; middle) and liquid water path (LWP; bottom) are shown for all four A-circles. Note that the scale of the Y-axis is different for the top and bottom panels and also different from that in Fig B.4.

the S-circles, whereas, for A-circles, the cloudiness can be observed up to flight level. A large proportion of clouds in A-circles have cloud tops much higher than 2 km, as shown in Fig. B.5.

B.4 Relationship between the meso-scale environment and clouds

B.4.1 *The thermodynamic environment*

The dry, moist and saturated moist static energy profiles in Fig. B.3 together characterize the thermodynamic state of the atmosphere in the circles. The vertical structure of these profiles is consistent among the S-circles. All circles show the same features of well-mixed sub-cloud layers, a relatively dry free troposphere, and inversions present at ~1.6 km (indicated by the max N^2 line), which align well with the cloud tops from the remote-sensing instruments. There are minor differences among the static energy profiles of the circles. However, these differences are more between days than across circles flown on the same day yet several hundreds of kilometers apart. As an example, consider the similarity among circles S3 and S4, both flown on the same day, a couple of hours apart.

Both circles, compared to S1 and S2, show stronger inversions at ~1.8 km, as well as slightly less humidity and weaker stability at ~4-4.5 km. These differences indicate that the thermodynamic environments sampled are more homogeneous in space than they are stationary in time. In contrast, the variation in cloudiness among the S-circles (e.g. the greater cloudiness in S4) is on the meso-scale, and is not consistent for circles flown on the same day. Therefore, due to the similarity in its state across the large-scale, the thermodynamics cannot be relied upon here to diagnose the meso-scale variability in cloudiness. With these observations, we thus find no support for the hypothesis that mean thermodynamic factors are adequate predictors of clouds for the meso-scale.

Upon analyzing conventional cloud-controlling factors for the S-circles, we find that the spread is small in the observed values for SST (27.9 - 29.4 °C), LTS (13 - 14 K) and PW (30 - 32 kg m^{-2}). For S4, none of these parameters has values that stand out as excessively large or small, compared to the other S-circles. Thus, the conventional cloud-controlling factors also fail to explain why S4 shows more cloudiness across several aspects. This indicates that although conventional cloud-controlling factors explain substantial variance on longer space and time scales, they are not as strongly correlated with the cloudiness at the meso-scale, which is consistent with findings of previous studies, e.g. Klein et al. (1995), Brueck et al. (2015) and Nuijens et al. (2015b).

B.4.2 *Influence of sub-cloud vertical motion on mass flux*

An important, and we assert decisive, distinction among the S-circles is that for S4, the low-level flow is converging, leading to a layer of upward motion between the surface and ~2 km (see velocity profiles in Fig. B.3). The other three S-circles show an almost completely subsiding layer from the surface to about 6 km. S4 is also the circle with largest values of shallow cumulus cloud fraction as well as cloud cover (see CF_{ShCu} in Fig. B.3 and Table B.2). Thus, since no thermodynamic component of the environment explains the large cloud amounts in S4, we hypothesize that the low-level convergence in S4 can provide a causal explanation. The convergence and subsequent upward vertical motion in the sub-cloud layer can exert its influence on clouds via the shallow convective mass flux (M). This hypothesis can also be extended to circle A2, which also has converging airmasses in the sub-cloud layer and has the largest shallow cumulus cloud fraction. To test our hypothesis, we use a simple mass-flux estimate for the circles.

Vogel et al., 2020 demonstrate that M can be estimated as a residual of the sub-cloud layer mass budget, relating M to the entrainment rate responsible for deepening the sub-cloud layer via small-scale mixing at its top (E) and meso-scale vertical velocity (W) at the top of the sub-cloud layer through the following budget equation:

$$\frac{\partial h}{\partial t} = E + W - M, \tag{B.1}$$

where $\frac{\partial h}{\partial t}$ is the rate of change of sub-cloud layer depth. Following Vogel et al., 2020 we neglect the temporal change of h in the budget and estimate M as

$$M = E + W. \tag{B.2}$$

The shallow convective mass flux at any height z can also be estimated in a more direct manner by the equation

$$M(z) = a_{co}(z) \cdot w_{co}(z), \tag{B.3}$$

where a_{co} is the cloud-core area fraction occupied by clouds and w_{co} is the mean updraft velocity in the clouds. The cloud-core area fraction is defined as the fraction of the cloud area that has positive vertical velocity at cloud base. Combining Eqs. B.2 and B.3 gives us a relationship between cloud core fraction at cloud base and the meso-scale vertical velocity as

$$a_{co} = \frac{E + W}{w_{co}}. \tag{B.4}$$

The estimates of meso-scale vertical velocity from the circle measurements are used to obtain W. Since the LCL can be taken as a proxy for the top of the sub-cloud layer, we take a mean value of the vertical velocity in a range of 50 m above and below the LCL as the value for W.

To ensure a robust assumption for the values of E and w_{co}, we rely on findings from previous studies. Vogel et al., 2020 show that day-to-day variations in M are more correlated to variations in W than to variations in E. Following this, we assume a constant value of E for all circles. Vogel et al., 2020 obtain a mean value of 12.5 mm s^{-1} over the S-circles, and we take this as the value of E for all circles, with an uncertainty of $\pm$ 2.5 mm s^{-1}.

For core updraft velocities, we use the Deardorff convective velocity scale w^*, which is a good approximation for cloud-base convective updrafts over the ocean surface as shown by Stratum et al. (2014) and Zheng (2019). The values of w* are linearly related to the cloud-base height, or the LCL (Zheng and Rosenfeld, 2015; Zheng, 2019). With values of the LCL ranging between 510 and 865 m, we use values from the linear relationship shown by Zheng (2019) and assume a conservative range for variations in w_{co} from 0.4 to 0.8 m s^{-1}, with a mean of 0.6 m s^{-1}.

Thus, we theoretically estimate the cloud-core area fraction at cloud base by using the aforementioned values of W, E and w_{co} as described by Eq. B.4. The blue line in Fig. B.6 shows predicted a_{co} and the shaded region indicates expected variability, for assumed variations in E and w_{co}. The peak shallow cumulus cloud fraction from the airborne HAMP radar has been overlaid on the theoretical estimates in Fig. B.6. The peak values are usually found within a ~300 m deep layer above the LCL. It is important to note here that the theoretical cloud-core area fraction is only the area of cloud cover with positive updraft velocity at cloud base. The cloud fraction from the radar however, is inclusive also of cloud areas that are negatively buoyant at cloud base, and thus, play no role in transporting mass outside the sub-cloud layer. The ratio of cloud core to total cloud cover has been empirically estimated to be 0.5 (Siebesma et al., 2003). Thus, the radar CF is expected to be greater than the estimated core fraction.

The CF values from the HAMP radar, however, are quite close to the predicted core fraction estimates. This is explained by the low sensitivity of the radar in detecting smaller clouds, and thus, giving lower cloud cover. Jacob et al. (2020) show that the HAMP radar could have missed an absolute value of ~7% of cloud fraction with radar reflectivity >-50 dBZ. Moreover, their study also shows that almost 75% of the clouds with LWP values < 50 g m^{-2} were missed by the radar. This explains why the radar CF is underestimated. The cloud fraction of A2 is higher compared to the estimated core fraction. This is consistent with the higher LWP and RWP (see Table B.2), which indicates a greater vertical development of the clouds rooted in the sub-cloud layer and that the majority of the clouds were captured by the radar.

Notwithstanding the difference in absolute values of estimated and actual fraction due to instrument limitations, the trend of the cloud fraction with respect to W is seen to be positive – similar to the theoretical estimation – thus lending strength to our hypothesis

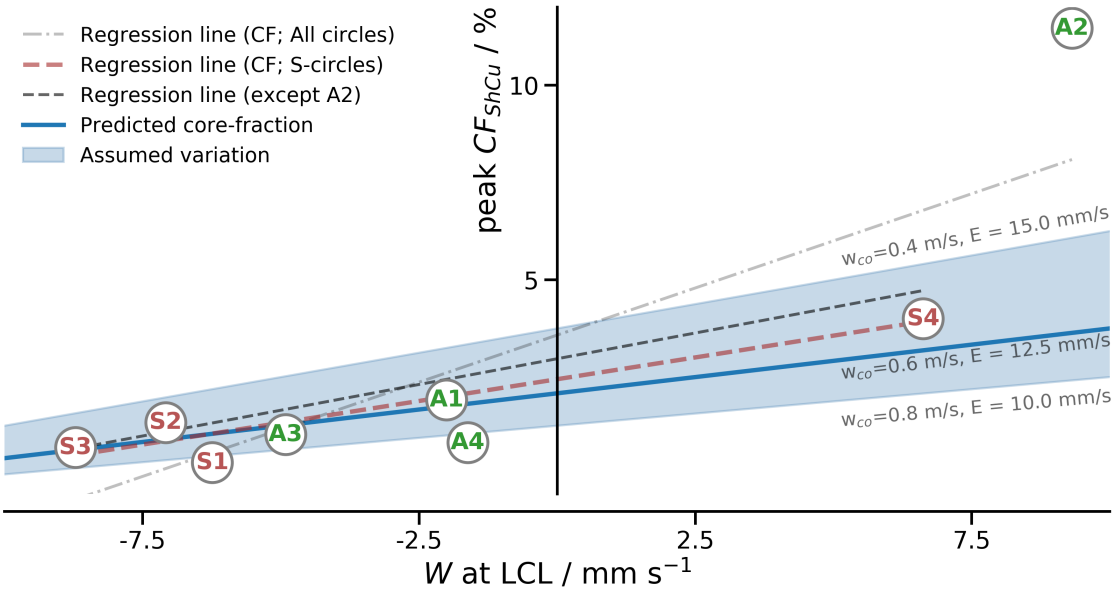

Figure B.6: Peak shallow cumulus cloud fraction (CF_{ShCu}) from the radar is plotted against the large-scale vertical velocity at respective LCL heights of the circles. The shaded regions show range of estimated cloud core fraction based on mass flux calculations (refer to the text in Section B.4.2). w_{co} and E values used for prediction are shown as mean (below thick blue line) and bounds (adjacent to shaded envelope boundaries). The regression lines are lines of least-squares fit for the data points indicated in the legend.

that the meso-scale vertical velocity at LCL can influence cloud base cloud fraction via the mass flux. These estimates thus provide a possible explanation as to why we see a higher cloud cover in S4 compared to the other S-circles. Clouds in S4 need to ventilate more air out of the mixed layer to balance the convergence of mass. This might be the cause for more active clouds in the region, with relatively higher LWP and RWP compared to the other S-circles. Even though subsidence reduces the mass flux for the other three S-circles, it is still not strong enough to offset the entrainment at the top of the mixed layer (equation B.2). Hence, we still get positive values of mass flux and the prevalence of some cloudiness in the region, although much less than in the region with convergence (circle S4).

The primary takeaway from Fig. B.6 thus is that the W-scaling provides a possible explanation for the variability in shallow cumulus cloudiness. However, the relationship in the figure cannot be taken as that having statistical significance because of the small number of samples. Nevertheless, the positive relationship we see strengthens the argument in favor of our hypothesis that low-level convergence controls cloud fraction more instantaneously at the meso-scale than do thermodynamics – something that is also put forward by previous studies using reanalysis products (e.g. Mauger and Norris, 2010; Myers and Norris, 2013; Szoeke et al., 2016).

We remind the reader that the values of cloud fraction plotted in Fig. B.6 are only for shallow cumulus clouds. If the total cloud cover were shown instead, circles A3 and A4 would show a large increase, as can be understood from Fig. B.7, which shows total cloud cover. Whereas Eq. B.4 describes controls on cloud base cloud fraction, it does not inform estimates of total cloud cover insofar as this is influenced by stratiform or other cloud processes aloft, e.g. the stratiform clouds pronounced in S3's lidar profile (Fig. B.3) are not explained by the equation.

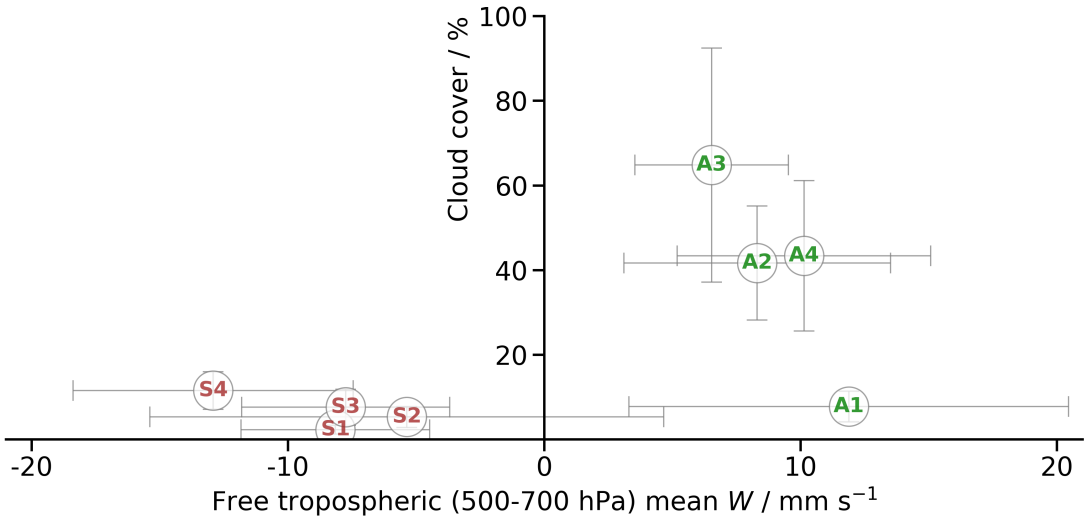

Figure B.7: Mean cloud cover from radar and satellite estimates of all circles plotted against the mean vertical velocity between pressure levels of 700 hPa and 500 hPa. Horizontal bars show standard deviation of W and extents of the vertical bars show the lower and upper estimate of cloud cover, with these estimates being from the radar and the satellite, respectively for all circles.

Another important takeaway from Fig. B.6 is the linearity in the relationship between peak ShCu fraction and vertical velocity among the eight circles. However, if extrapolated towards values of larger negative W, this would not be linear any more, since cloudiness cannot be negative. This is important in light of how current cloud schemes deal with meso-scale variability. They attempt to account for variability on scales that are smaller than the grid-scale for today's climate models (Sommeria and Deardorff, 1977), but they do not specifically account for meso-scale (20-200 km) variability, such as that associated with the organization of shallow convection (Stevens et al., 2019b). Thus, in effect, cloud schemes assume that the meso-scale contributions average to zero. This assumption is valid only if the relationship between cloudiness and the meso-scale perturbations is linear. Thus, if there is large variability in meso-scale conditions, the assumption that the meso-scale influence would average to zero does not hold true because of the non-linearity discussed above.

B.4.3 *Free tropospheric vertical motion*

In contrast to W in the lower levels, W in the free troposphere has long been linked to cloudiness. In one of the earliest applications of this idea, Slingo (1987) demonstrated that ω in the upper troposphere can be an effective indicator of the synoptic regime, and consequently, can determine the cloud type prevailing in the region. Several studies since then have shown consistently how ω in the free troposphere influences time-averaged cloudiness over large ($\gg$ 200 km) spatial scales (e.g. Bony et al., 2004; Myers and Norris, 2013). We test this idea for our 'snapshots' of cloudiness on the meso-scale by associating the total cloud cover estimates of the circle from the radar and satellite to the mean W (as a proxy for ω) in the free troposphere between pressure levels of 700 hPa and 500 hPa in Fig. B.7.

The clustering of data points of A-circles away from that of S-circles in Fig. B.7 shows the influence that ω in the free troposphere holds in setting the regime for cloudiness. However, this association becomes poor if taken for values of vertical velocity only at 500 hPa or only at 700 hPa (not shown), and serves as a hint that at the meso-scale, these values cannot be used as predictors (as previously suggested by Stevens and Brenguier (2009)). This is especially true for the S-circles. If we want to correctly predict the differences in cloudiness among S-circles, just a measure of the standard ω_{500hPa} or ω_{700hPa} values are not enough, since a subsiding layer is a characteristic feature of the trade wind regions and will always be present.

Foregoing studies (e.g. Medeiros and Stevens, 2009; Webb et al., 2015) have already noted this, stating that ω_{500} alone is not a good predictor of low-level cloudiness within subsidence regimes, and that LTS is a better predictor for these regimes. But from the NARVAL2 observations, we find that even both these predictors jointly are insufficient. Free tropospheric ω (or W) helps distinguish between cloud types, but to distinguish between different extents of cloudiness within suppressed trade-wind environments, focus should shift to factors that control cloudiness at the meso-scale. Therefore, in this sense, the vertical motion in the sub-cloud layer might hold more importance than that in the free troposphere.

B.5 CONCLUSIONS

We use estimates of meso-scale atmospheric vertical motion and collocated cloud measurements from the NARVAL2 campaign to understand the response of tropical clouds to their meso-scale environments. For this, we examine four cases each of low-level cloudiness forming in suppressed (S-circles) and active (A-circles) meso-scale environments.

Among the circles in the suppressed environments, circle S4 with air converging in its sub-cloud layer has greater cloudiness in terms of cloud fraction, liquid water path (LWP) and rain water path (RWP). The only other circle, which also has a converging sub-cloud layer is A2, and it also shows large values of shallow cumulus cloud fraction, LWP and RWP. From this association alone, it is difficult to establish if the convergence is causing the cloudiness or if it is a consequence of the cloudiness. In case of the latter though, we are left with no explanations for the cloudiness. Thus, in the absence of any thermodynamic factor that could explain the variation in cloudiness, we believe that the most plausible explanation for the increased cloudiness in S4 and A2 is the low-level convergence.

We find that large-scale parameters such as free tropospheric ω or precipitable water can be useful in distinguishing between cloud regimes, such as shallow and deep convection. However, these are not helpful in distinguishing between the amount of cloudiness and its meso-scale variability within a given regime (e.g. suppressed). In this sense, the meso-scale dynamics proves to be more useful. We use a simple mass-flux estimate to show how the meso-scale vertical motion within the sub-cloud layer might regulate shallow cumulus cloud fraction at cloud base. This measure serves as a good indicator of shallow cloud amount across all flights, irrespective of thermodynamic state. Thus, the vertical velocity at the top of the sub-cloud layer helps explain variations in cloud base cloud amounts that cannot otherwise be explained. While the relationship between mass flux and meso-scale vertical velocity for steady state has been emphasized previously (Neggers et al., 2006; Vogel et al., 2020), this is the first time we see a potential manifestation of it in nature through cloud area fraction at cloud base.

Although the relationship between mass flux and vertical velocity is linear, the same cannot be said for the relationship between cloudiness and vertical velocity, as cloudiness cannot be negative. This means that the response of clouds to their meso-scale circulation is non-linear. Thus our results challenge the ansatz of general circulation model (GCM) parameterizations that the influence of the meso-scale circulation on cloudiness is inconsequential over larger scales. This outlook becomes especially important in the context of global warming, since any changes to the meso-scale circulation would not be reflected in the clouds, and will thus mask the changes in clouds and cloud feedbacks in a warming climate.

Our finding of the influence of meso-scale dynamics on clouds could also be considered to revisit strategies of estimating cloud fraction in climate models. Currently, all cloud parameterisation schemes rely on thermodynamical variables to determine cloudiness. Although dynamics strongly influences thermodynamical variables, cloud schemes keep them out of direct consideration. Grid-scale pressure velocity, ω, being a variable that already exists in GCMs, can be used to adjust parameterizations so as to depend also on meso-scale dynamics, along with the thermodynamic variables. Our results strengthen and provide observational support to the reasoning that dynamics needs to be incorporated directly into cloud schemes.

The NARVAL2 observations, although with a small sample size (8 circles), have the advantage of being well-characterized in terms of their environment (thermodynamics and dynamics) as well as the cloudiness (radar, lidar and satellite remote-sensing), and sample regimes of both deep and shallow convection. With the limited sample size in mind, we do not provide a quantitative relationship between the variation in cloudiness and the vertical velocity. Instead, we put forward the argument that to understand the variability in meso-scale cloudiness, the circulation at that scale is something that we cannot ignore. Observations from the *ElUcidating the RolE of Cloud-Circulation Coupling in ClimAte* (EUREC^{4}A; Bony et al., 2017; Stevens et al., 2021) field campaign, which were focused on the trade-wind suppressed regimes during January-February of 2020, will offer a larger statistical sampling of cloudiness and dynamical conditions, to quantify the variability in meso-scale conditions and thus help test the hypothesis we make. EUREC^{4}A will also provide more direct estimates of cloud base cloud fraction and more robust estimates of the shallow convective mass flux.

Nevertheless, an advantage with the NARVAL2 cases is the sampling over active regimes. Our results provide observational evidence in favor of the argument that at the meso-scale, kinematic factors – such as sub-cloud meso-scale vertical velocity – can have greater control over low-level clouds than do thermodynamic factors, and as shown by both active and suppressed cases, this relationship does not seem to vary based on the regime of convection.

Acknowledgments We thank the entire team of NARVAL2 for making the measurements. We thank Chris Fairall for sharing his code to compute the surface fluxes from the dropsondes. We thank Anna Lea Albright, Cathy Hohenegger, Theresa Mieslinger, Robert Pincus and Hauke Schulz for their insights and helpful discussions. We thank Heike Konow for help with the cloud objects from the HAMP radar, which we refer to as the Konow mask in this study. We thank Manuel Gutleben and Martin Wirth for their help with the WALES lidar data and cloud top height estimates using the same. This project has received funding from the European Research Council (ERC) project EUREC4A (Grant 694768) under the European Union's Horizon 2020 research and innovation programme.

ERA5 data was retrieved from the IPSL mesocenter ESPRI facility, which is supported by CNRS, Sorbonne Universite, Labex L-IPSL, CNES, and Ecole Polytechnique.

Data Availability Statement The NARVAL2 measurements from the dropsondes, HAMP radar and the HAMP microwave radiometers are available as unified data products from the CERA database at the URL: https://doi.org/10.1594/WDCC/HALO_measurements_3. The LWP and RWP products from the microwave measurements are available at the CERA database at the URL: https://doi.org/10.26050/WDCC/HALO_measurements_6 The WALES lidar data and the dropsondes raw data can be accessed from the HALO database http://doi.org/10.17616/R39Q0T. The GridSat-B1 satellite products are publicly available at the URL: https://www.ncei.noaa.gov/data/geostationary-ir-channel-brightness-temperature-gridsat-b1/access/. The ERA5 reanalyses used in this study can be accessed from the ECMWF website https://www.ecmwf.int/en/forecasts/datasets/reanalysis-datasets/era5

C

MESOSCALE CIRCULATION IN THE TRADES : STRUCTURE, VARIABILITY AND INTERPLAY WITH OTHER ENVIRONMENTAL FACTORS

The work in this appendix is in preparation for submission as:

George, Geet, Bjorn Stevens, Sandrine Bony and Raphaela Vogel. (2021). "Mesoscale circulation in the trades : Structure, variability and interplay with other environmental factors". (*in preparation*)

Mesoscale circulation in the trades : Structure, variability and interplay with other environmental factors

Geet George[1], Bjorn Stevens[1], Sandrine Bony[2] and Raphaela Vogel[2]

[1] Max Planck Institute for Meteorology, Hamburg, Germany
[2] LMD/IPSL, Sorbonne University, CNRS, Paris, France

ABSTRACT

We paint a picture of the meso-scale circulation in the trades by using measurements of meso-scale area-averaged horizontal mass divergence ($\mathcal{D}$), relative vorticity (ζ) and subsidence rate (ω) taken during the *ElUcidating the RolE of Cloud-Circulation Coupling in ClimAte* (EUREC^{4}A) field campaign over the northern tropical Atlantic, to describe the quantities' mean vertical structure and their variability across days and over a period of a few hours. The sub-cloud and cloud layers are both found to have positive $\mathcal{D}$ and negative ζ in their mean structure. However, in contrast, we find that the sub-cloud $\mathcal{D}$ anomalies and cloud $\mathcal{D}$ anomalies have varying signs of divergence consistently across flight-days. We propose a shallow circulation mechanism that aims to explain this negative association as well as connects other pieces of evidence such as a negative association between sub-cloud $\mathcal{D}$ and humidity. Moreover, we find the variability of $\mathcal{D}$ and ω to be of magnitudes much larger than their mean values, as opposed to those of quantities such as humidity and temperature. These results argue for models to include a more robust prescription of meso-scale forcings, which are constrained by measurements such as the ones discussed here.

C.1 INTRODUCTION

A long-standing lack of observations have limited the current understanding of the nature of atmospheric circulation at the meso scale. Here, the *meso scale* stands for a spatial scale of 20-200 km and a temporal scale of a few hours, or the *meso-β* scale as per Orlanski (1975). The meso-scale circulation plays a crucial role in how clouds respond to a warming climate (Bony et al., 2015) and therefore, an understanding of its structure and variability is important to improve the understanding of clouds-circulation coupling. A recent aircraft campaign in the trade-wind regions of the north Atlantic measured meso-scale area-averaged quantities relevant to circulation, over 13 different days during a month-long period in early 2020. Here, we use these measurements to describe the circulation parameters such as horizontal mass divergence ($\mathcal{D}$), relative vorticity (ζ) and subsidence rate (ω) in terms of their mean vertical structure and their variability observed over time-scales of a few hours and across days. We also propose a persistent shallow circulation mechanism in the trades to explain the associations we find between moist-layer quantities of divergence and moisture.

Investigations related to the meso-scale circulation have been quite overlooked compared to circulations at the synoptic scale. This traces back to the lack of measurements at the former scale. The poor understanding of meso-scale circulation also results in current models being prescribed climatological mean values of subsidence (e.g. Jansson et al., 2021), despite the spatial grid and time-steps of the simulations being often of the order of the meso scale. As such, cloud feedbacks to changes in the circulation can still be studied if these feedbacks are of a linear nature, but observational measurements point towards that not being the case (George et al., 2021a). To use models to understand clouds-circulation coupling therefore, both at the meso scale and at the climate scale, it is important that models are prescribed forcings of subsidence which are more representative of the meso-scale than of the climatology. Forcings for meso-scale subsidence however are practically unused, since they are not constrained from any observations of the meso-scale circulation.

Outside of the modeling approach to understand cloud-circulation coupling, an observational approach is also required to describe the processes in nature and investigate how the circulation impacts the clouds and other atmospheric parameters (Bony et al., 2017). This is also important in interpreting the seemingly different cloud feedbacks to circulation among models (e.g. in high-resolution simulations by Vial et al. (2017) and in climate models by Webb et al. (2015)). Moreover, recent studies show that the meso-scale vertical velocity can be important regulators of the shallow convective mass flux (Vogel et al., 2020) and cloud core-area fraction (George et al., 2021a). Therefore, despite being important quantities in characterising the circulation of the atmosphere, and therefore a potentially significant cloud-controlling factor, observational challenges have rendered the mean and variability of circulation parameters in the trade-wind regions elusive.

The atmospheric environment can primarily be characterised by the state variables obtained from dropsonde measurements. These can be divided into thermodynamic and kinematic quantities, with pressure, temperature and humidity coming under the former, and wind measurements coming under the latter category. Whereas individual dropsonde soundings provide local horizontal wind measurements, vertical wind measurements – which are of a few orders of magnitude lower than horizontal wind values – cannot be estimated reliably from individual soundings. However, a regression method demonstrated and tested by Bony and Stevens (2019) can be applied to obtain area-averaged estimates of divergence and vorticity if the dropsondes are launched along a circular path (hereafter simply called circles). Based on mass conservation, one can integrate values of divergence at every altitude from the surface upwards to get an estimate of the area-averaged vertical velocity.

This method of estimating area-averaged measurements of the motion field was employed extensively in the recent *ElUcidating the RolE of Cloud-Circulation Coupling in ClimAte* (EUREC^{4}A; Stevens et al., 2021) field campaign, where 85 circles were flown to measure the meso-scale circulation parameters and describe the meso-scale state of the atmosphere. We use the measurements from 70 out of 85 circles from EUREC^{4}A, since these were unbiased in terms of the meteorological conditions sampled. This provides a unique opportunity to investigate the divergence and motion-field in the trades with some statistical confidence.

The structure of this manuscript is as follows. The data and methodology are described in section C.2. We describe the mean structure of the divergence, subsidence and vorticity in section C.3, and their variability in different aspects in section C.4. A shallow circulation hypothesis is described in section C.5 along with the evidence that we see for it in

the measurements. Finally, we provide a summary of our results and some concluding points in section C.6.

C.2 DATA AND METHODOLOGY

C.2.1 *Data*

Here, we primarily use data measured from dropsondes during the EUREC^{4}A field campaign. EUREC^{4}A took place in January-February, 2020 over the north tropical Atlantic upwind of Barbados. The dropsonde measurements taken during the campaign are made available as a dataset called *Joint dropsonde Observations of the Atmosphere in tropical North atlaNtic meso-scale Environments*, with the backronym JOANNE (George et al., 2021c). One of the data products of JOANNE, Level-4, provides area-averaged quantities at 10 m vertical spacing from the circle measurements of EUREC^{4}A, such as horizontal mass divergence and relative vorticity among others. The measured quantities are from the surface up to ~10 km, which was the typical flight altitude during the circles. Thus, we use JOANNE Level-4 extensively here to characterise the meso-scale circulation parameters.

During EUREC^{4}A, a standard circle was fixed for measurements to facilitate synergy with other participating platforms, with a diameter of 222.82 km and centred at 57.67°W, 13.31°N. Following Stevens et al. (2021), we call this the EUREC^{4}A-circle. In all, 85 circles were sampled during EUREC^{4}A, out of which 73 were EUREC^{4}A-circles. For this study, we will resort to statistics from the 70 EUREC^{4}A-circles flown by the German *High Altitude and Long range* aircraft (HALO), to restrain samples only during daytime. Flight-phase segmentation files provided by Konow et al. (2021) give details about the circle segments during the campaign, and we use these to identify the HALO-EUREC^{4}A circles from the remaining circles.

The 70 HALO-EUREC^{4}A circles were flown over 13 different flight-days, with a typical flight including 6 circles, each launching 12 dropsondes spaced equally around the circle over a period of an hour. On most flight days, HALO flew two sets of three circles each with an excursion in between aimed at sampling upwind conditions. We call these sets here as circling-sets. Thus, for a typical flight, sampling of two circling sets was carried out over a period of 7-8 hours. An overview of the circles flown during EUREC^{4}A and the dropsondes therein is provided in George et al. (2021c).

The consecutive nature of circles provide an opportunity to study the area-averaged quantities on a finer scale than just one value every hour. Since there is new information collected with every dropsonde, we can stagger the circle measurements to effectively provide the state of the atmosphere every 5-6 minutes. To qualify as staggered circles, we set three conditions; (a) There should be at least 12 sondes in every staggered circle, (b) the difference between the launch time of the first and the last sonde should be less than 90 minutes and (c) there should be sonde measurements present in at least three out of the four quadrants of the EUREC^{4}A circle. With these conditions, there are roughly 45 such staggered circles per flight day. We use these to look into how the atmospheric state variables vary over the shorter time period of 2-3 hours.

C.2.2 *Estimating standard error*

Whereas one of the main objectives of this study is to describe the mean vertical structure of the kinematic properties, this description would be incomplete without a provision of the uncertainty of the mean.

The 70 EUREC^{4}A circles provide, by a big margin, the largest sample of measurements available as yet for estimating the mean structure of divergence in the trade-wind regions. There is, however, the question of how well 70 semi-independent circles can provide the mean structure of divergence over a month-long period. If the samples are assured to be independent, one can use the estimator for the standard error of mean (σ_{μ_x}),

$$\sigma_{\mu_x} = \frac{\sigma_x}{\sqrt{n}} \tag{C.1}$$

where σ_x is the standard deviation of measurements in the sample and n is the number of measurements. However, the samples taken during EUREC^{4}A cannot be considered truly independent. Whereas every circle was an independent measurement, the time-correlation makes circle measurements dependent, especially those flown on a single day. Therefore, instead of taking 70 as the value of n in equation C.1, we take a cautious sample size of half the actual number, i.e. $n = 35$, thus increasing the standard error estimate.

C.2.3 *Atmospheric layers of interest*

We first define some known features of the trade-wind atmosphere's vertical structure to aid in our characterisation of the thermodynamic and kinematic parameters. The terms discussed here have been known and observed since decades (e.g. Malkus, 1958; Augstein et al., 1974), and are still currently used to define the vertical structure of the trade-wind environment (e.g. Vogel et al., 2020). Nevertheless, the definitions used in this study are presented below.

From the ocean surface up to ~50 m, the atmosphere experiences 'friction' of the surface and is characterised by a sharp decrease in humidity from surface upwards. This is called the surface layer. Above the surface layer, a neutrally stratified layer is present, characterised by turbulent eddies and resulting in a constant distribution of specific humidity through the layer. This layer is thus called the mixed layer. The top of the mixed layer is marked by a local maximum in relative humidity – a result of the constant specific humidity and an adiabatic lapse-rate in the layer. We thus define the top of the mixed layer height (h) as the level of maximum relative humidity in the bottom 1000 m.

One of the most persistent features of the trades, the trade-wind inversion, is where the atmosphere is distinctly stable and displays a relatively strong decrease in moisture, or a hydrolapse. We define the inversion height (z_{inv}) as the level at which the Brunt-Väisälä frequency squared (N^2) is the maximum below 3000 m. N^2 is estimated using the virtual potential temperature (θ_v) and its vertical gradient ($\frac{d\theta_v}{dz}$) as,

$$N^2 = \frac{g}{\theta_v}\frac{d\theta_v}{dz}, \tag{C.2}$$

where g stands for gravitational acceleration. The use of N^2 thus considers the effects of the temperature and humidity gradients at the inversion.

The cloud layer is essentially the layer between the mixed layer top and the inversion height. However, there is often a transition layer present between the mixed layer top and

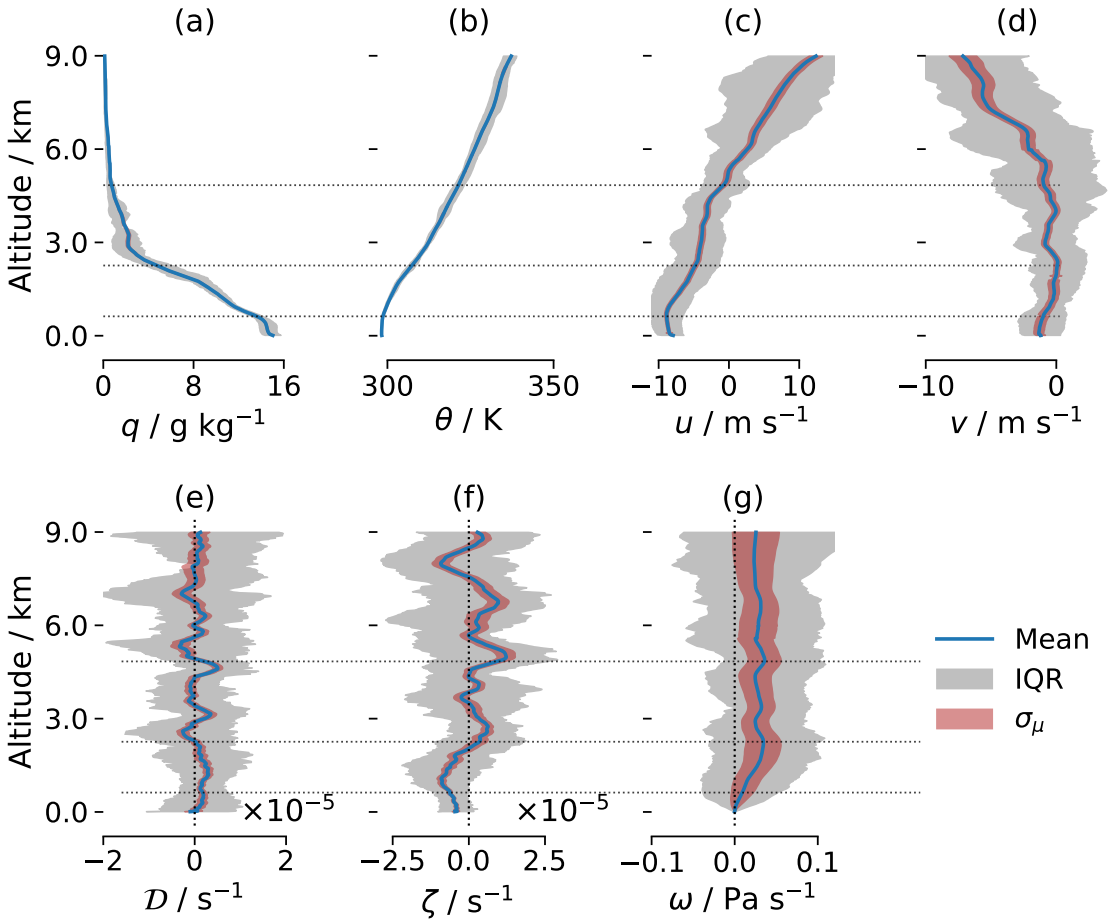

Figure C.1: Mean profiles of quantities – (a) specific humidity, (b) potential temperature, (c) eastward wind, (d) northward wind, (e) horizontal mass divergence, (f) absolute vorticity, (g) pressure velocity – measured during EUREC^{4}A are shown by blue lines. Grey shaded regions indicate the inter-quartile range (IQR) for measurements through the EUREC^{4}A period and orange shaded regions indicate the estimator of standard error for mean values (σ_μ). Horizontal dotted lines cutting across lower and upper panels show mixed layer top (bottom-most), inversion height (middle) and triple-point isotherm (upper-most).

the cloud base height. The transition layer is marked by a strong reduction in humidity compared to the mixed layer. Similarly, the inversion height is not a single stable level, rather a layer over which the inversion conditions persist, and thus cap the moist layer. Therefore, to ensure that we exclude any variability present in the transition layer or the inversion layer, we conservatively define the cloud layer as the layer between h + 250 m and z_{inv} - 250 m.

Additionally, another level of significance is the level at which the temperature in the atmosphere reaches the triple-point temperature of water, similar to the definition of Stevens et al. (2017). We call this the triple-point level (z^*). The layer between z_{inv} and z^* is called the lower free troposphere.

The average height of the sub-cloud layer top during the campaign is ~630 m, indicated by the bottom-most horizontal line in upper and lower panels in Fig. C.1, while the average inversion height is estimated at ~2260 m, which is indicated by the middle horizontal line. The triple-point isotherm is shown by the upper-most horizontal line with a mean value of 4840 m.

C.3 MEAN VERTICAL STRUCTURE

In this section, we describe the mean vertical structure of the state variables from the measurements. Fig. C.1 shows the mean profiles of atmospheric state variables and the estimated corrected standard error of the mean (orange shaded regions).

C.3.1 *Thermodynamic Quantities*

The mean profiles of specific humidity (q) and potential temperature (θ) shown in Fig. C.1 reflect several of the aforementioned features related to the layers of interest in the vertical structure of the trade-wind atmosphere. The surface layer (0-50 m) displays sharp vertical gradients for humidity. The vertically homogeneous values of θ and q below h indicate a well-mixed layer. The θ profile shows the base of a stable layer at $\sim$2 km from the surface, indicating the well-known trade-wind inversion layer. At the same altitude, following the inversion, we see a strong negative gradient in the q profile, also called the hydrolapse. Above the inversion layer, in the free troposphere, the charateristically dry atmosphere of the trade-winds is observed, although this is not the case for all flight days. Conditions with much greater humidity in the free troposphere were also sampled during the campaign. These are discussed in detail in section C.4.

C.3.2 *Kinematic Quantities*

C.3.2.1 *Divergence* ($\mathcal{D}$)

The mean value for $\mathcal{D}$ (blue line in Fig. C.1e) between the surface and the triple-point isotherm shows three clear features: (a) a diverging layer in the moist layer, i.e. from the surface to the inversion layer, (b) layers of alternating signs just above the inversion height, with sharp convergence below and divergence above and (c) layers of sharp divergence below and convergence above the triple-point isotherm.

The divergent layer from surface to the inversion height has a local minimum at the sub-cloud layer top. Both the cloud and sub-cloud layer show similar profiles with diverging airmasses. This feature, however, is only observed in the mean profile. At shorter time scales such as over a day or over circling-sets, the sub-cloud and cloud layers often show opposing signs, as we shall see in section C.5.1.

It is worth noting here that the co-location of the above features in the mean profile of $\mathcal{D}$ with the previously discussed levels of interest come from independent measurements. The former is derived from horizontal winds, whereas the latter are obtained from measurements of humidity and temperature. The mean divergence structure is thus intricately linked to the environment's thermodynamic parameters. This association can likely be attributed to the structure of radiative cooling at these levels, which sets the mean divergence structure over the long term. However, further investigations are needed to understand why we see these clear features in the divergence structure occur exactly at the levels of interest.

C.3.2.2 *Subsidence rate* (ω)

The features in the mean structure of $\mathcal{D}$ are also reflected subsequently in the mean structure of ω (blue line in Fig. C.1g). The atmospheric column is, on average, in a subsiding regime. Since the moist layer has mean divergence throughout, we see increasing values

of subsidence up to the top of the moist layer, above which ω stays relatively consistent around a free tropospheric mean of 0.028 Pa s^{-1} (or 1.00 hPa h^{-1}), with minor, compensating fluctuations due to the aforementioned alternating layers of divergence and convergence.

Based on the weak temperature gradient approximation, the time-mean cooling rate of the atmosphere Q can also be estimated from the mean subsidence rate and temperature lapse rate as,

$$Q = -\omega \frac{T}{\theta} \frac{d\theta}{dp} \tag{C.3}$$

We make a back-of-the-envelope calculation with time-mean values averaged over the measured free-tropospheric column for the quantities on the right-hand side in Eq. C.3 ($\frac{T}{\theta} = 0.82$; $\frac{d\theta}{dp}$ = -0.06 K hPa^{-1}). This gives values of Q as 1.29 K/day, which is roughly how quickly the subsiding wing of the Hadley cell can be expected to cool (e.g. Hartmann and Larson, 2002; McFarlane et al., 2007).

C.3.2.3 *Relative Vorticity (ζ)*

In the moist layer, the ζ mean profile shows negative values, i.e. anti-cyclonic rotation, with the magnitude peaking just above the mixed layer height. This is consistent with the $\mathcal{D}$ pattern in the moist layer, since diverging air is usually associated with anti-cyclonic movement. At the inversion layer, consistent with $\mathcal{D}$, ζ reduces to zero and shows a layer of positive ζ just above it. The similarity between the $\mathcal{D}$ and ζ mean profiles is not observed above this layer.

C.4 VARIABILITY

In this section, we discuss the variability observed in the state variables with dispersion measures of inter-quartile range and the coefficient of variation. Later, we also discuss the variability in the variables across time-scales of days as well as over a few hours.

C.4.1 *Inter-quartile range*

The range of different conditions sampled by the EUREC^{4}A-circles and the impartiality in sampling meteorological conditions allows us to understand the variability of meso-scale conditions in the trades. The inter-quartile range of state variables is shown by the grey shaded region in Fig. C.1.

Moisture varies most in the sub-cloud layers and above the cloud layer. The presence of elevated moist layers sampled during some of the flights causes the greater variability seen at and above 3 km. Temperature values remain quite steady within the moist layer and most of the variation is seen in the free troposphere.

The kinematic quantities, i.e. the wind components in the three dimensions along with divergence and vorticity, show large variability. For the area-averaged quantities, the range of variability is in fact an order of magnitude than the mean values. Divergence values at the top of the mixed layer and vorticity values within the mixed layer show a noticeable drop in variability compared to the rest of the vertical profile.

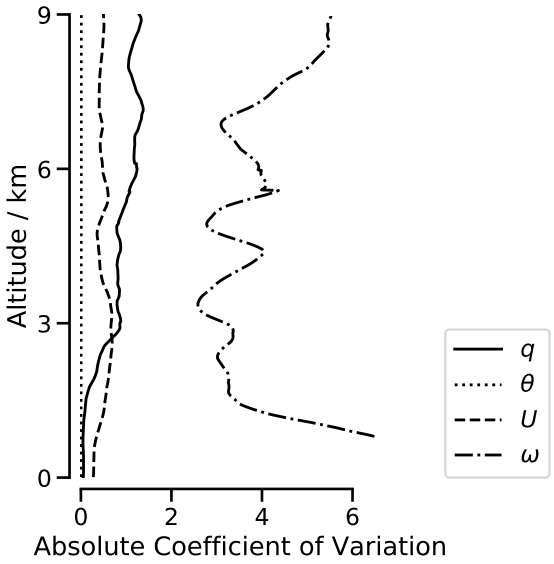

Figure C.2: Absolute values of coefficient of variation (CV) of specific humidity (q), potential temperature (θ), wind speed (U), and pressure velocity (ω) during EUREC^{4}A. Values greater than 7 are not shown.

C.4.2 *Coefficient of Variation*

At first glance, the thermodynamic quantites seem to be fairly invariant, whereas the kinematic quantities show relatively large variability. However, since the quantities are over different units, a better comparison would be using the coefficient of variation for the different quantities, which is defined as the ratio of standard deviation to the mean, thus providing a dimensionless quantity. We show the absolute values of the coefficient of variation for humidity, potential temperature, horizontal wind speed and subsidence rate in Fig. C.2.

A comparison of the variability among the parameters in Fig. C.2 shows that there are differences over orders of magnitude in how quantities can vary from their mean values in the meso-scale. For example, potential temperature shows the least variability from the mean, but pressure velocity can be expected to vary by four times the mean value itself. This difference between the parameters' variabilities is also reflected in the standard error estimates in Fig. C.1, where the confidence in retrieving the mean for the thermodynamic quantities is much higher than that for the kinematic quantities.

The large variability of ω with respect to the mean has important implications in the way forcings are provided to models, especially for the boundary layer. Since ω varies by a much greater magnitude than the mean, providing a time-mean forcing to models that run over short time-scales will affect investigations into processes at the cloud scale. It also affects models that run over longer time-scales and investigate climate processes if the response to the forcings are non-linear. George et al. (2021a) show that the response of clouds to the meso-scale circulation could potentially be non-linear. In case of non-linearities, such large variabilities from the mean would greatly compound the errors in estimating feedbacks on the climate scale.

In contrast, for quantities like q, especially within the moist layer, the variability is much less compared to the mean value. Thus, if the mean value of q is prescribed to models, it wouldn't be as detrimental to the output as would providing a climatological profile of ω, which can vary by an order of magnitude from the mean over shorter time-scales.

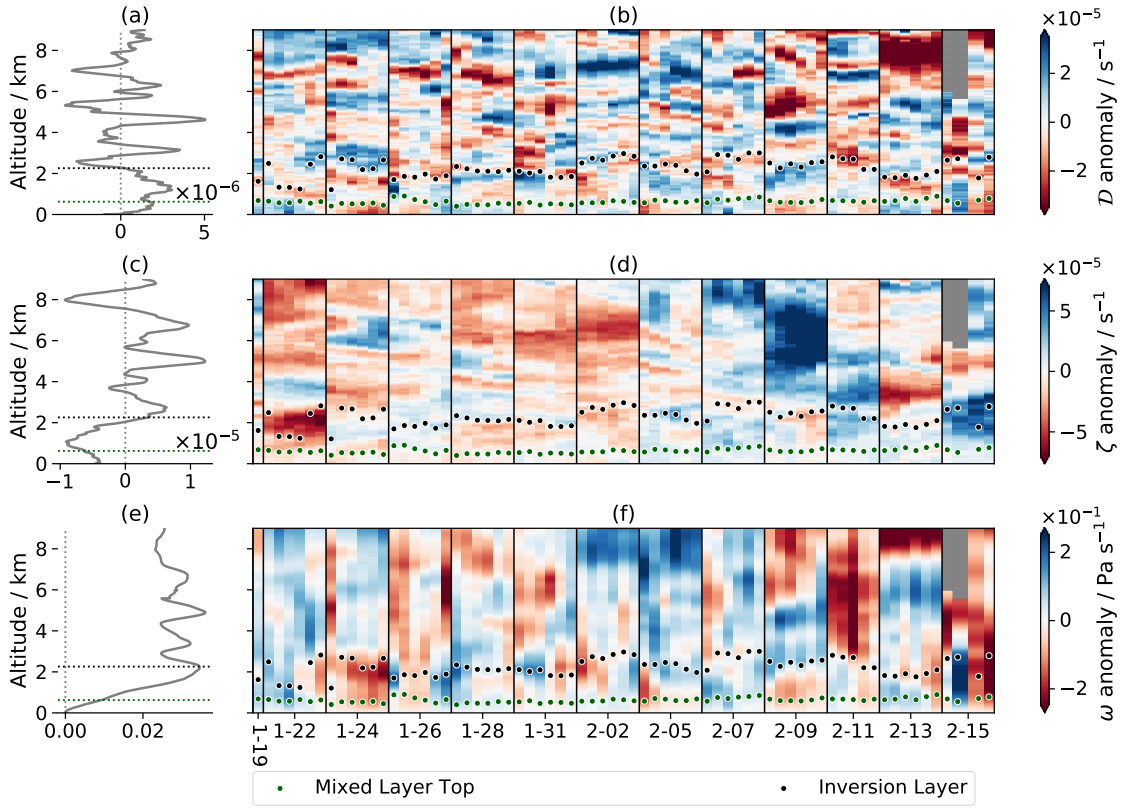

Figure C.3: Vertical profiles of (a) $\mathcal{D}$ in s^{-1}, (c) ζ in s^{-1} and (e) ω in Pa s^{-1} averaged over all HALO-EUREC^{4}A circle measurements. The anomaly from time-mean (shown as hues) of $\mathcal{D}$, ζ and ω for individual circle profiles are shown in (b), (d) and (f), respectively. The profiles are separated into different boxes based on their respective flight dates, which are indicated on the bottom of the x-axis in (f). Each box includes the same number of profiles corresponding to the EUREC^{4}A-circles flown during the respective flight. Profiles are sequenced based on circle-count, and the scale of x-axis is not linear in time. The mixed-layer top height and inversion height are overlaid as green and black markers (lines over the mean profiles), respectively.

Currently, widely-used large-eddy simulations (LES) forcings, such as from the RICO measurements (VanZanten et al., 2011), prescribe a long-term mean of ω, with values fixed throughout the boundary layer.

C.4.3 *Day-to-day meso-scale conditions*

C.4.3.1 *Divergence*

The day-to-day values in all area-averaged quantities, i.e. $\mathcal{D}$, ζ and ω show an order of magnitude larger values than the time-mean (see Fig. C.3). This is in contrast to the quantities shown in Fig. C.4. The mean profile of q or θ could as well be a measured profile taken over any random day. However, the same cannot be said for $\mathcal{D}$ or ω, wherein neither the structure nor the magnitude on any given day bear similarity to the mean profiles.

The vertical structures of $\mathcal{D}$ across days show finer-scale features in the vertical structure than any other parameters (see Figs. C.3 and C.4), but they vary drastically over days. On one hand, on some days, such as on 9th February, the entire measured profile

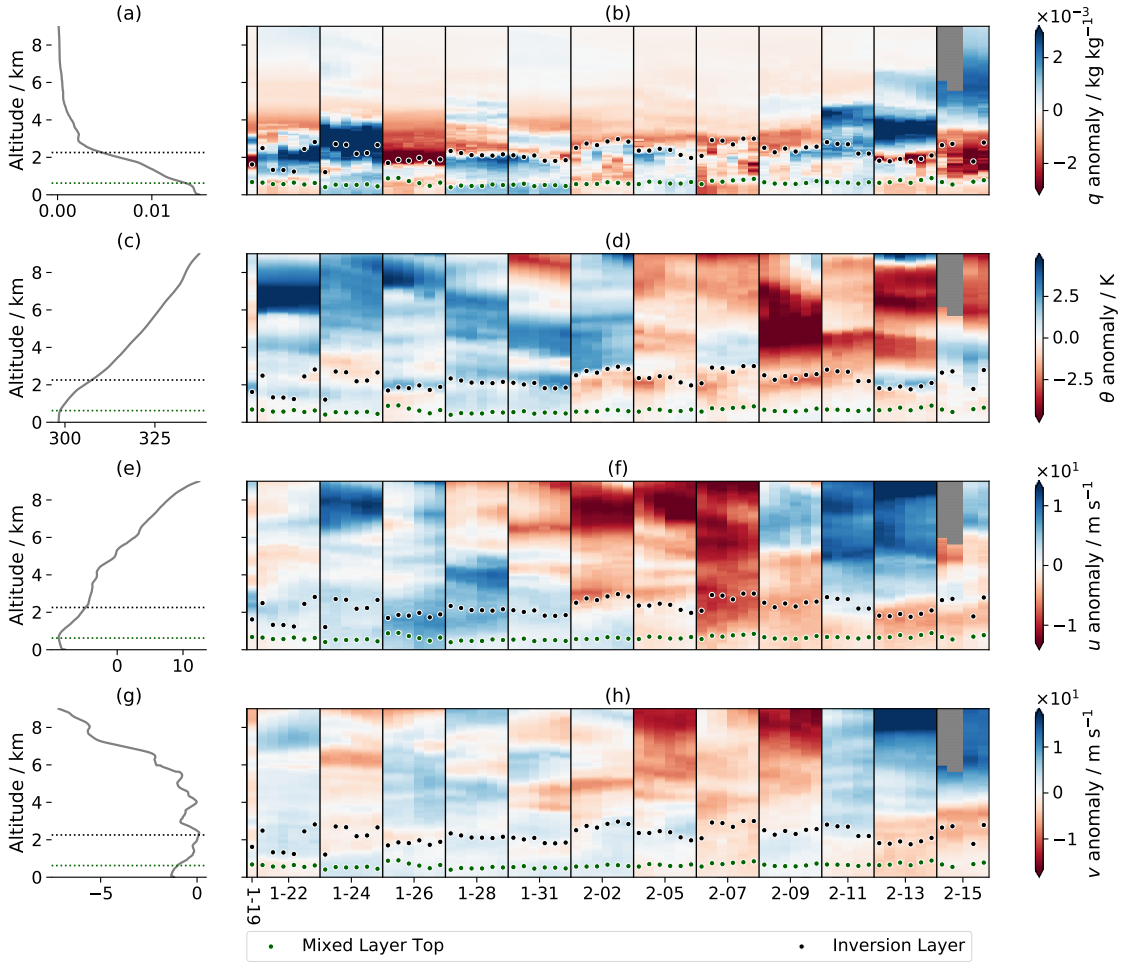

Figure C.4: Vertical profiles of (a) q in kg kg^{-1}, (c) θ in K, (e) u in m s^{-1} and (g) v in m s^{-1} averaged over all HALO-EUREC^{4}A circle measurements. The anomaly from time-mean (shown as hues) of q, θ, u and v for individual circle profiles are shown in (b), (d), (f) and (h), respectively. The profiles are separated into different boxes based on their respective flight dates, which are indicated on the bottom of the x-axis in (h). Each box includes the same number of profiles corresponding to the EUREC^{4}A-circles flown during the respective flight. Profiles are sequenced based on circle-count, and the scale of x-axis is not linear in time. The mixed-layer top height and inversion height are overlaid as green and black markers (lines over the mean profiles), respectively

can be seen as alternating bands of anomalously high and low divergence during the entire 7-8 hours of sampling. On the other hand, there are also examples when divergence varied drastically during the same flight, such as on 22nd January. A clear instance of the propagation of an inertial gravity wave was also sampled on 31st January. The sign of $\mathcal{D}$ just above and below the inversion layer can be seen alternating from the first three circles of the flight to the next three. The wave signature was also visible in satellite cloud observations, as reported by Stephan and Mariaccia (2021).

There is no apparent fixed structure to the vertical profile of $\mathcal{D}$ on a daily scale. There are, however, some consistencies that can be found across the days, especially in the lower free troposphere. The $\mathcal{D}$ in the mixed layer very rarely changes sign through the day, i.e. over the sampling period of 7-8 hours, although the intensity can vary quite a bit. The same can be said about $\mathcal{D}$ in the cloud layer with the exception of 3-4 days. For most days, the signs of the anomaly of $\mathcal{D}$ are opposite between the mixed and cloud layers,

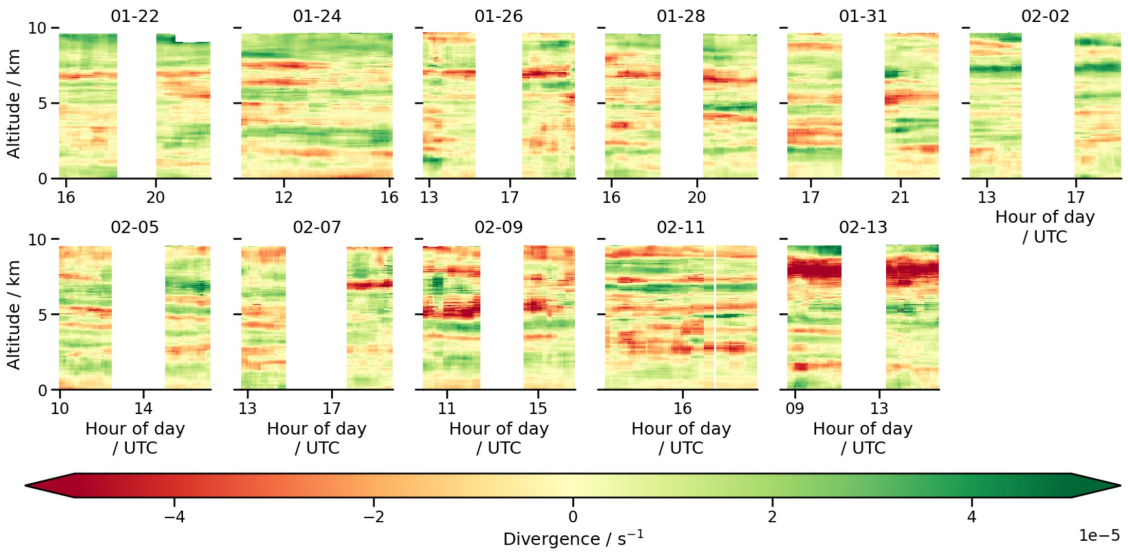

Figure C.5: Divergence profiles from staggered circles are shown along the time axis for the different flight days as indicated by the titles of the sub-plots. The white gaps throughout in the timelines are because no circles which qualified criteria to be a staggered circle were found for the time.

with the neutral layer of zero divergence often lying at or just above the top of the mixed layer. On most days, the value of $\mathcal{D}$ also shows a sign change just above and below the inversion.

c.4.3.2 *Humidity*

Free-tropospheric humidity tends to be low for most of the days, except the last three flight-days when a large increase is observed (see Fig. C.4b). These are mostly indicative of elevated moisture layers, such as those described in Stevens et al. (2017) and their persistence over a period of days suggests it to be a large scale signal. Flight reports also confirm the presence of thick, altus clouds during the flights on 13th and 15th February, thus providing visual confirmation of upper-level humidity. Incidentally, on these days the sub-cloud and cloud layers are anomalously drier compared to the campaign-mean. The free troposphere is also moister on 24th January, when intense cold-pool activity was observed within and surrounding the circle region. We discuss this in section C.5.2.2.

c.4.4 *Variability within circling sets*

The staggered circles (described in section C.2.1) can be used to study the variability of quantities over a period of a few hours, i.e. within the circles of a day, or within a single circling set. The divergence profiles from these staggered circles are shown in Fig. C.5, which displays a finer structure of divergence temporally than from estimates of just the six circles. The most striking feature is the difference in the vertical structure across days, especially in the free troposphere. The days also show different rates of change of the structure through the day. However, compared to the other quantities used here to describe the atmospheric state (not shown), the vertical structure of divergence is the least consistent through the day.

The time regularity of the staggered circles also allows for an autocorrelation analysis to determine how rapidly a quantity decorrelates with itself and thus, gives an idea of

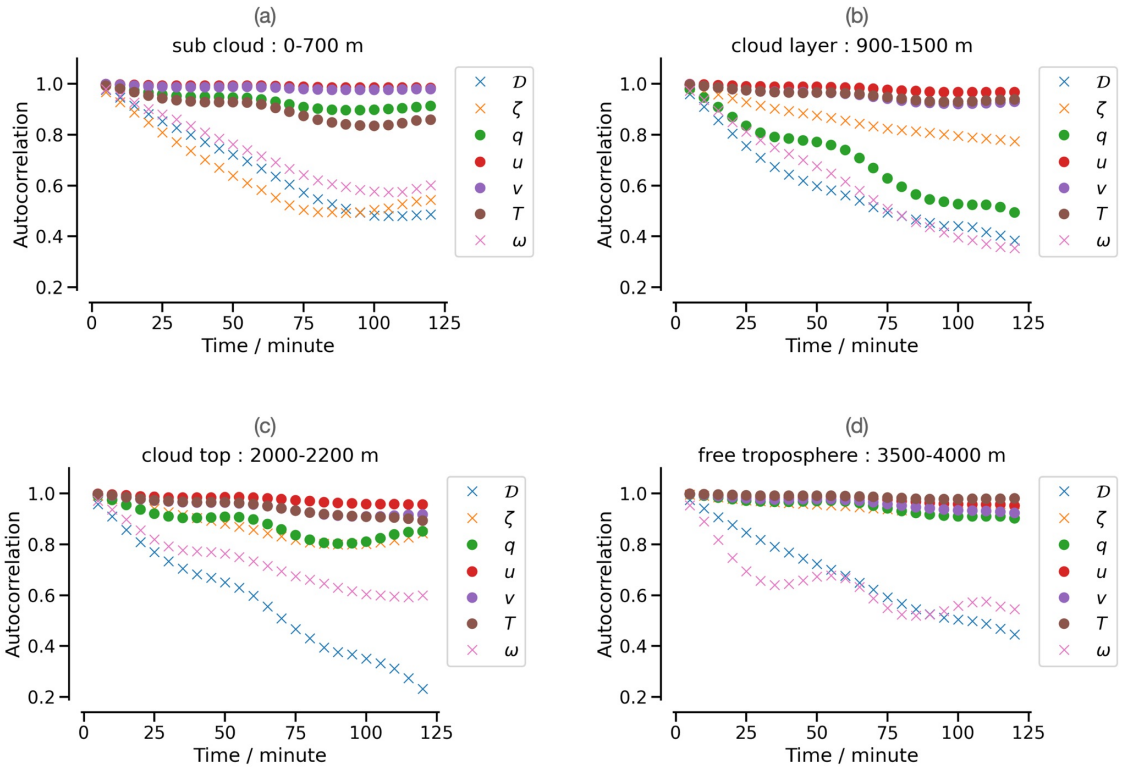

Figure C.6: Autocorrelation estimates of state variables from the staggered circles are shown over 2 hours for different levels in the atmosphere, as indicated by the titles of the sub-plots.

the time scale at which quantities vary. We grouped the staggered circle estimates in to five minute intervals, based on a restrained nearest neighbour method, and estimated the auto-correlation coefficients. Fig. C.6 shows the autocorrelation coefficients for the area-averaged quantities (marked as crosses) $\mathcal{D}$, ζ, ω along with other quantities (marked as circles) q, θ, u and v. The divergence is the most rapidly decorrelating variable with values of autocorrelation reaching e-folding values within two hours, except in the sub-cloud layer (or mixed layer). The variability of divergence is highest at the cloud top (or the inversion level). Since ω is derived from $\mathcal{D}$, it also shows similar extents of decorrelation. All other quantities show relatively little decorrelation within two hours, with two notable exceptions – vorticity in the sub-cloud layer and humidity in the cloud layer. Thus, the time-scale of variability is much smaller for $\mathcal{D}$ compared to those of thermodynamic quantities such as θ or q, with the one exception noted above. The horizontal winds are also remarkably steady over such a short time-scale compared to $\mathcal{D}$.

C.5 SHALLOW CIRCULATION HYPOTHESIS

C.5.1 *Evident associations*

A quick glance at the divergence anomalies in Fig. C.3 shows that very often, divergence values have opposite signs in the sub-cloud layer and cloud layer. This also becomes evident in Fig. C.7a, which shows how mean divergence anomaly in the sub-cloud layer varies with that in the cloud layer. The green-coloured points indicate mean values for circles flown over a single day. This captures typically 7-8 hours of a day, and does not

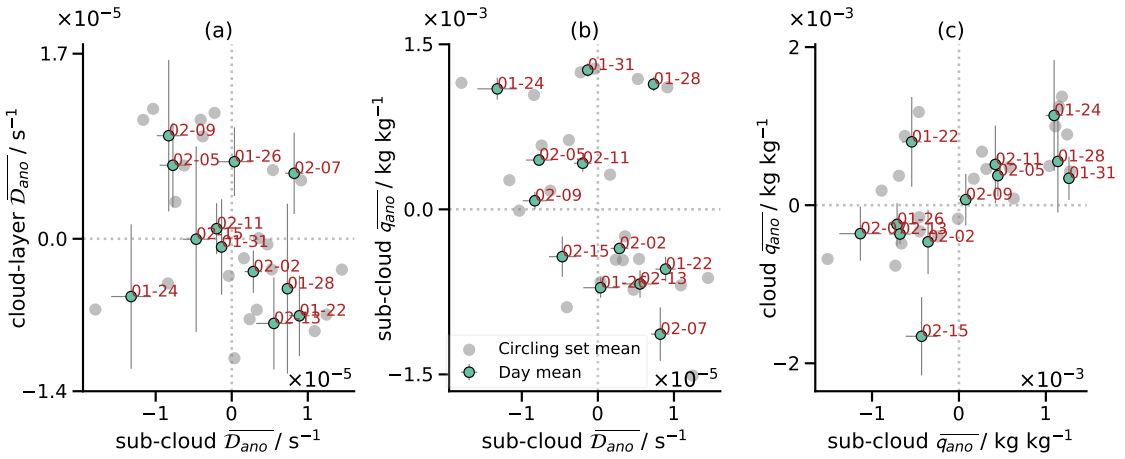

Figure C.7: (a) Mean sub-cloud layer anomaly of $\mathcal{D}$ from time-mean plotted against that in the cloud layer, (b) Mean sub-cloud layer anomaly of $\mathcal{D}$ from time-mean plotted against mean sub-cloud anomaly of q and (c) Mean sub-cloud layer anomaly of q from time-mean plotted against that in the cloud layer. Day means are shown by green markers and circling set means by grey markers. Error bars show the standard deviation in the mean along altitude.

represent a "daily" mean. Grey points indicate mean values for circling sets, which are typically 3 circles, as explained earlier.

We interpret the negative association between $\mathcal{D}$ in the sub-cloud and cloud layer as the presence of shallow circulations within the moist layer, such as shown in the schematic in Fig. C.8. The measurements across different flight days sample both the converging and diverging branches with no particular bias towards either. Thus, we do not suspect this association to be of a shallow circulation between the moist convergence zones and the trade-wind regions, but rather that of local circulations in the trade-wind regions.

The clear outlier is the flight on 24th January, when both the sub-cloud and cloud layers experienced strong convergence. This flight was with persistent, and strong cold-pool activity as also identified by Touzé-Peiffer et al. (2021), and hence, we would not expect a steady low-circulation feature.

The flight-days with a mean converging sub-cloud layer tend to show greater mean sub-cloud q anomaly values. Fig. C.7b shows anomalies of q and ω averaged over the sub-cloud layer plotted against each other. The negative association between q and ω is more distinct with the day-means rather than circling set means and single circle values (latter not shown). Thus, the relationship likely holds strong only over longer averaging periods, indicating that the process driving this is of a temporal scale greater than an hour or more.

A similar association of q and $\mathcal{D}$ in the sub-cloud layer has also been observed in the summertime trade-wind measurements from the *Next Generation Remote Sensing for Validation Studies* campaign (NARVAL2). Although NARVAL2 had a limited sample size of eight circles, the only two circles with converging sub-clouds also showed the moistest sub-cloud and cloud layers (George et al., 2021a).

C.5.2 *Proposed Mechanism*

We hypothesise that shallow circulations within the moist layer explain the associations discussed in section C.5.1. A schematic for our proposed mechanism is shown in Fig. C.8.

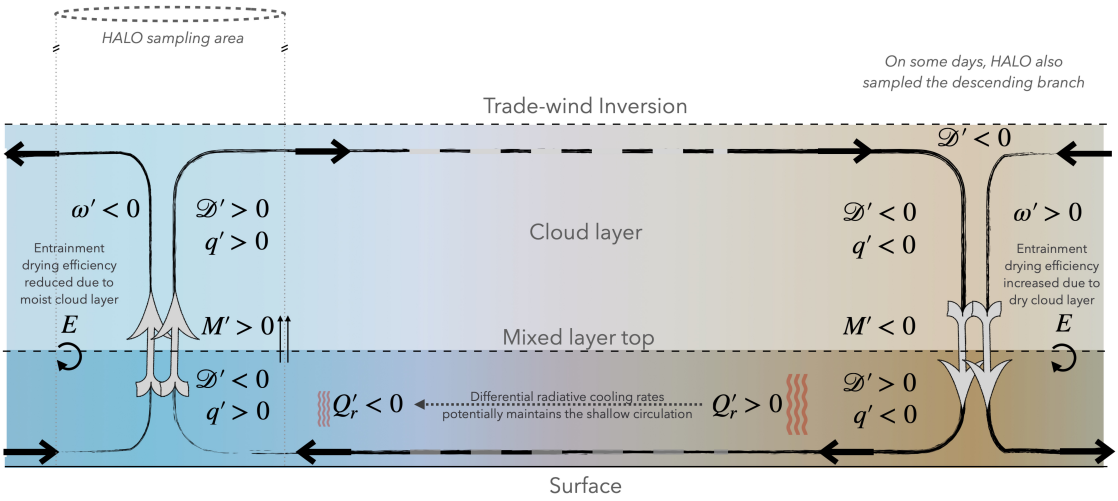

Figure C.8: Schematic of the shallow circulation discussed in section C.5 is shown. The marker ′ against any parameter indicates the parameter's anomaly from its long-term mean. E stands for entrainment rate, M for shallow convective mass flux and Q_r for radiative cooling rate. The remaining symbols have the same meaning as in the text.

In the rising branch of the circulation, with convergence in the mixed layer, an increase in mass flux is observed as a result of the rising air. Considering constant turbulent fluxes and entrainment, this moistens the cloud layer, since the mixed layer contains more absolute moisture than the cloud layer. The moistened cloud layer reduces the drying efficiency of entrainment and hence, the mixed layer does not dry as rapidly, causing it to remain moist.

Conversely, on the other branch of the circulation with divergence in the mixed layer, air descends from the cloud layer to the mixed layer. The air in the cloud layer being drier than that in the mixed layer increases entrainment efficiency. The subsidence also means that mass flux is reduced. Thus, the cloud layer gets drier and the drying of the mixed layer by the entrainment is amplified. Thus, these mechanisms in the rising and descending branch of the circulation maintain the anomalous moistness and dryness, respectively. The time required to moisten the cloud layer enough to reduce entrainment drying efficiency also explains why the associations we see in section C.5.1 are stronger over longer time-scales.

The maintenance of the moistness and dryness in their respective branches of the circulation will cause differential radiative cooling rates between the branches, because of the difference in the moisture fields. This could thus be a factor in maintaining the shallow circulation, causing converging areas to get moister and moister areas to cool slower than the surroundings. This would cause surrounding air to converge to the area and thus, the cycle continues. The converse argument can be made with the descending branch and how divergence and dryness feed each other. The differential radiative cooling rate has also been attributed as a factor in driving and maintaining shallow circulations by Schulz and Stevens (2018) and Naumann et al. (2019). Such an auto-maintenance of these shallow circulations also explains their longevity through the sampling period of a day.

This hypothesis also ties in with the observation that a moister sub-cloud layer is most often associated with a moister cloud-layer (see Fig. C.7c), and conversely, a drier sub-cloud layer tends to show a dry anomaly in the cloud layer. The only notable exception here are measurements from the flight on 22nd January, where the sub-cloud and cloud layers show dry and wet anomalies, respectively. This case is discussed later.

Based on the above reasoning, we hypothesise that on different days, HALO sampled one of the branches of these local, shallow circulations. Further analyses of understanding their effects on clouds can be carried out by taking advantage of colocated measurements of clouds from the remote-sensing data taken by the HALO, ATR-42 and Meteor platforms.

Despite the mixed layer and cloud layer $\mathcal{D}$ being inversely coupled, the mean $\mathcal{D}$ for the campaign shows positive values, i.e. diverging airmasses in both. Therefore, we assert that these hypothesised shallow circulations are embedded within the large-scale mean flow. This indicates that over long term means, there is a continuity in the sub-cloud and cloud layer, but in a non-intuitive way in short term variability due to the shallow circulations.

C.5.2.1 *Circle measurements in the wake of a fish*

The circle measurements for the flight on 22nd January were made in the cloud-free, subsiding regions of a large fish pattern in the south. Compared to usual wintertime trade-wind conditions, fish – likely features of extratropical disturbances – have anomalously strong low-level convergence and moist cloud layers (Schulz et al., 2021). The detrainment from the fish's anamolously moist cloud-layer could be why the cloud-layer in the EUREC^{4}A-circle is also anomalously high.

C.5.2.2 *Circle measurements amidst cold pools*

A notable exception from the observed vertical structure of $\mathcal{D}$ in all days, is that on the 24th of January, wherein convergence was found to be present throughout the moist layer, as also indicated by Fig. C.7a. The circle region on this day was marked by constant cold-pool activity during the sampling period, and we believe could have broken down any structure of shallow circulations that may have been present. The soundings made in the cold-pool could also have affected the estimates of divergence, as shown by Touzé-Peiffer et al. (2021).

C.6 SUMMARY AND CONCLUSION

We use measurements taken during the EUREC^{4}A campaign to characterise the meso scale circulation parameters in the wintertime trade-wind conditions in the tropical north Atlantic. For this, we use the dropsonde measurements from the circles flown by HALO during the campaign. We use the following quantities to describe the state of the atmosphere and subsequently characterise their mean vertical structure and variability: specific humidity (q), potential temperature (θ), horizontal winds (u and v), horizontal mass divergence ($\mathcal{D}$), relative vorticity (ζ) and pressure velocity or subsidence rate (ω).

Using measurements from the HALO-EUREC^{4}A circles, we describe the mean vertical structure of $\mathcal{D}$, ζ and ω. Mean positive divergence is observed in both the mixed and cloud layer, with a local minimum in the values between the two layers, indicating consistent conditions in both layers over long-time averages. Other interesting features in the vertical structure such as sign change in mean divergence is observed to be co-located at altitudes of interest in the trade-wind region, i.e. mixed-layer top, inversion height and the triple-point isotherm. The mean profile of ω shows a completely subsiding profile, and a mean value of $\sim$0.028 Pa s^{-1} in the free troposphere, thus also being in agreement with the climatological radiative cooling rate in the region. The mean ζ throughout the

moist layer is negative, indicative of anti-cyclonic rotation which is expected from regions experiencing divergence.

Over flight-day means, we find negative associations between anomalies of mixed-layer $\mathcal{D}$ and cloud-layer $\mathcal{D}$. Further, the anomalies of mixed-layer $\mathcal{D}$ and mixed-layer q are also negatively associated. We hypothesise that these are in fact, evidences of shallow circulations in the moist layer of the trades. In the ascending branch, with convergence in the mixed layer, the moist layer is anomalously moist, whereas in the descending branch, the divergence in the mixed layer keeps the moist layer anomalously dry. Since the drying and moistening is linked to the increased and reduced drying efficiency of the entrainment, respectively, this process occurs over longer time-periods than just an hour, and therefore, the evidences are clearer in the day means of circling set means, compared to individual circle values. If our hypothesis is true, it means that HALO sampled different branches of shallow circulations during the different flight-days.

Our hypothesised mechanism is a rather simplistic view not accounting for several complexities in nature, such as varying entrainment rates and turbulent fluxes. Conditions on the synoptic scale also potentially interfere with such shallow circulations, reducing their clarity in EUREC^{4}A observations. But the evidence we find in most flight-days is a mark of the persistence of these shallow circulations and their regulation of other environmental parameters such as humidity, temperature, and plausibly, the cloudiness. Shallow circulations such as these can explain the aggregation of moisture and cloudiness (as also shown by Bony et al., 2017; Bretherton and Blossey, 2017), thus furthering areas for the investigation of persistent organisation patterns in shallow clouds (Schulz et al., 2021).

The EUREC^{4}A-circle measurements were unbiased toward any meteorological state and despite that, a large range of variability was sampled during the EUREC^{4}A period. Overall, thermodynamic quantities show little variability compared to the kinematic ones. An analysis of the coefficient of variation for the variables shows that ω varies by almost four times the mean value. Moreover, a look into the day-to-day variability shows that values of $\mathcal{D}$ and ω vary by an order of magnitude compared to the mean.

The large variability seen in $\mathcal{D}$ and ω, compared to the other thermodynamic quantities, highlight the importance of prescribing accurate forcings to models. If climatological mean values are input to models as forcings, it rests on the assumption that the influence of the meso scale averages out. But even minor non-linearities in meso scale processes will mean that the model outputs will deviate greatly from results if models had been provided meso-scale forcings instead, because of the large difference between the magnitudes of meso-scale and climatological values of divergence and subsidence.

Further investigations are planned into understanding how the different components of the budgets of mass, moisture and thermal energy regulate the conditions in the meso scale. The colocated measurements of clouds from EUREC^{4}A are also planned to be studied with these divergence measurements as a step towards understanding clouds-circulation coupling.

BIBLIOGRAPHY

Albright, A. L., B. Fildier, L. Touzé-Peiffer, R. Pincus, J. Vial, and C. Muller (2021). "Atmospheric radiative profiles during EUREC^{4}A". *Earth System Science Data* 13.2, pp. 617–630. DOI: 10.5194/essd-13-617-2021. URL: https://essd.copernicus.org/articles/13/617/2021/.

Augstein, Ernst, Heiner Schmidt, and Feodor Ostapoff (Mar. 1974). "The vertical structure of the atmospheric planetary boundary layer in undisturbed trade winds over the Atlantic Ocean". *Boundary-layer meteorology* 6.1-2, pp. 129–150. ISSN: 0006-8314. DOI: 10.1007/{BF00232480}. URL: http://link.springer.com/10.1007/%7BBF00232480%7D (visited on 10/01/2020).

Bach, Richard (1981). *Illusions : the adventures of a reluctant Messiah*. Dell/E. Friede. ISBN: 0440343194. URL: https://cmc.marmot.org/Record/.b10778780 (visited on 05/26/2021).

Becker, Sebastian, André Ehrlich, Johannes Stapf, Christof Lüpkes, Mario Mech, Susanne Crewell, and Manfred Wendisch (2020). *Meteorological measurements by dropsondes released from POLAR 5 during AFLUX 2019*. data set. DOI: 10.1594/PANGAEA.921996. URL: https://doi.org/10.1594/PANGAEA.921996.

Benner, Timothy C. and Judith A. Curry (Nov. 1998). "Characteristics of small tropical cumulus clouds and their impact on the environment". *Journal of Geophysical Research* 103.D22, pp. 28753–28767. ISSN: 01480227. DOI: 10.1029/{98JD02579}. URL: http://doi.wiley.com/10.1029/%7B98JD02579%7D (visited on 06/24/2020).

Bolton, David (July 1980). "The computation of equivalent potential temperature". *Monthly Weather Review* 108.7, pp. 1046–1053. ISSN: 0027-0644. DOI: 10.1175/1520-0493(1980)108\textless1046:{TCOEPT\textgreater2}.0.{CO};2. URL: http://journals.ametsoc.org/doi/abs/10.1175/1520-0493%5C%281980%5C%29108%5C%%7B3C1046%5C%7D%%7B3ATCOEPT%5C%7D%%7B3E2%7D.0.%7BCO%5C%7D%%7B3B2%7D (visited on 07/06/2020).

Bony, S., J.-L. Dufresne, H. Le Treut, J.-J. Morcrette, and C. Senior (Mar. 2004). "On dynamic and thermodynamic components of cloud changes". *Climate dynamics* 22.2-3, pp. 71–86. ISSN: 0930-7575. DOI: 10.1007/s00382-003-0369-6. URL: http://link.springer.com/10.1007/s00382-003-0369-6 (visited on 12/03/2019).

Bony, Sandrine and Jean-Louis Dufresne (2005). "Marine boundary layer clouds at the heart of tropical cloud feedback uncertainties in climate models". *Geophysical Research Letters* 32.20. ISSN: 0094-8276. DOI: 10.1029/{2005GL023851}. URL: http://doi.wiley.com/10.1029/%7B2005GL023851%7D (visited on 12/03/2019).

Bony, Sandrine and Bjorn Stevens (Mar. 2019). "Measuring Area-Averaged Vertical Motions with Dropsondes". *Journal of the Atmospheric Sciences* 76.3, pp. 767–783. ISSN: 0022-4928. DOI: 10.1175/{JAS}-D-18-0141.1.

Bony, Sandrine, Bjorn Stevens, Felix Ament, Sebastien Bigorre, Patrick Chazette, Susanne Crewell, et al. (Sept. 2017). "EUREC4A: A field campaign to elucidate the couplings between clouds, convection and circulation". *Surveys in Geophysics*, pp. 1–40. ISSN: 0169-3298. DOI: 10.1007/s10712-017-9428-0.

Bony, Sandrine, Bjorn Stevens, Dargan M. W. Frierson, Christian Jakob, Masa Kageyama, Robert Pincus, et al. (Mar. 2015). "Clouds, circulation and climate sensitivity". *Nature*

Geoscience 8.4, pp. 261–268. ISSN: 1752-0894. DOI: 10.1038/ngeo2398. URL: http://www.nature.com/doifinder/10.1038/ngeo2398 (visited on 12/03/2019).

Bretherton, C. S. and P. N. Blossey (2017). "Understanding Mesoscale Aggregation of Shallow Cumulus Convection Using Large-Eddy Simulation". *Journal of Advances in Modeling Earth Systems* 9.8, pp. 2798–2821. DOI: https://doi.org/10.1002/2017MS000981. eprint: https://agupubs.onlinelibrary.wiley.com/doi/pdf/10.1002/2017MS000981. URL: https://agupubs.onlinelibrary.wiley.com/doi/abs/10.1002/2017MS000981.

Brueck, Matthias, Louise Nuijens, and Bjorn Stevens (Apr. 2015). "On the Seasonal and Synoptic Time-Scale Variability of the North Atlantic Trade Wind Region and Its Low-Level Clouds". *Journal of the Atmospheric Sciences* 72.4, pp. 1428–1446. ISSN: 0022-4928. DOI: 10.1175/{JAS}-D-14-0054.1. URL: http://journals.ametsoc.org/doi/10.1175/%7BJAS%7D-D-14-0054.1 (visited on 12/03/2019).

CDS (2017). *ERA5: Fifth generation of ECMWF atmospheric reanalyses of the global climate*. SOFTWARE.COMPUTER_SOFTWARE. URL: https://cds.climate.copernicus.eu/cdsapp%5C#!/home (visited on 06/29/2020).

Dussen, J. J. van der, S. R. de Roode, and A. P. Siebesma (2016). "How large-scale subsidence affects stratocumulus transitions". *Atmospheric Chemistry and Physics* 16.2, pp. 691–701. DOI: 10.5194/acp-16-691-2016. URL: https://acp.copernicus.org/articles/16/691/2016/.

Edson, James B., Venkata Jampana, Robert A. Weller, Sebastien P. Bigorre, Albert J. Plueddemann, Christopher W. Fairall, Scott D. Miller, Larry Mahrt, Dean Vickers, and Hans Hersbach (Aug. 2013). "On the Exchange of Momentum over the Open Ocean". *Journal of physical oceanography* 43.8, pp. 1589–1610. ISSN: 0022-3670. DOI: 10.1175/{JPO}-D-12-0173.1. URL: https://journals.ametsoc.org/jpo/article/43/8/1589/12011/On-the-Exchange-of-Momentum-over-the-Open-Ocean (visited on 07/04/2020).

Fairall, C. W., E. F. Bradley, J. E. Hare, A. A. Grachev, and J. B. Edson (Feb. 2003). "Bulk parameterization of air–sea fluxes: updates and verification for the COARE algorithm". *Journal of climate* 16.4, pp. 571–591. ISSN: 0894-8755. DOI: 10.1175/1520-0442(2003)016\textless0571:{BPOASF\textgreater2}.0.{CO};2. URL: http://journals.ametsoc.org/doi/abs/10.1175/1520-0442%5C%282003%5C%29016%5C%%7B3C0571%5C%7D%%7B3ABPOASF%5C%7D%%7B3E2%7D.0.%7BCO%5C%7D%%7B3B2%7D (visited on 07/04/2020).

Fleming, James Rodger (2020). *First woman: Joanne Simpson and the tropical atmosphere*. Oxford University Press. ISBN: 9780191895340. DOI: 10.1093/oso/9780198862734.001.0001.

George, Geet (2021). *JOANNE (Joint dropsonde Observations of the Atmosphere in tropical North atlaNtic meso-scale Environments) software*. Version v1.0.0. DOI: 10.5281/zenodo.4746313.

George, Geet, Bjorn Stevens, Sandrine Bony, Marcus Klingebiel, and Raphaela Vogel (2021a). "Observed impact of meso-scale vertical motion on cloudiness". *Journal of the Atmospheric Sciences*. ISSN: 0022-4928. DOI: 10.1175/{JAS}-D-20-0335.1.

George, Geet, Bjorn Stevens, Sandrine Bony, Robert Pincus, Chris Fairall, Hauke Schulz, et al. (2021b). *JOANNE : Joint dropsonde Observations of the Atmosphere in tropical North atlaNtic meso-scale Environments*. Version v1.0.0. DOI: 10.25326/221.

George, Geet, Bjorn Stevens, Sandrine Bony, Robert Pincus, Chris Fairall, Hauke Schulz, Tobias Kölling, Quinn T. Kalen, Marcus Klingebiel, Heike Konow, Ashley Lundry, Marc Prange, and Jule Radtke (2021c). "JOANNE : Joint dropsonde Observations of the Atmosphere in tropical North atlaNtic meso-scale Environments". *Earth System Science Data*. in review, pp. 1–33. DOI: 10.5194/essd-2021-162.

Gleick, James (1987). *Chaos: Making a New Science*. USA: Penguin Books. ISBN: 0140092501. DOI: 10.5555/62026.

Gutleben, Manuel, Silke Groß, and Martin Wirth (Aug. 2019). "Cloud macro-physical properties in Saharan-dust-laden and dust-free North Atlantic trade wind regimes: a lidar case study". *Atmospheric Chemistry and Physics* 19.16, pp. 10659–10673. ISSN: 1680-7324. DOI: 10.5194/acp-19-10659-2019. URL: https://www.atmos-chem-phys.net/19/10659/2019/ (visited on 06/24/2020).

Hardy, Bob (1998). "ITS-90 Formulations for Vapor Pressure, Frostpoint Temperature, Dewpoint Temperature, and Enhancement Factors in the Range –100 to +100 C". *Proceedings of the Third International Symposium on Humidity and Moisture*. (Visited on 03/20/2021).

Hartmann, Dennis L. and Kristin Larson (Oct. 2002). "An important constraint on tropical cloud - climate feedback". *Geophysical Research Letters* 29.20, pp. 12-1-12–4. ISSN: 00948276. DOI: 10.1029/{2002GL015835}. URL: http://doi.wiley.com/10.1029/%7B2002GL015835%7D (visited on 12/03/2019).

Hersbach, Hans, Bill Bell, Paul Berrisford, Shoji Hirahara, András Horányi, Joaquín Muñoz-Sabater, et al. (June 2020). "The ERA5 global reanalysis". *Quarterly Journal of the Royal Meteorological Society*. ISSN: 0035-9009. DOI: 10.1002/qj.3803. URL: https://onlinelibrary.wiley.com/doi/abs/10.1002/qj.3803 (visited on 02/25/2021).

Holland, Joshua Z. (Sept. 1970). "Preliminary Report on the BOMEX Sea-Air Interaction Program". *Bulletin of the American Meteorological Society* 51.9, pp. 809–820. ISSN: 0003-0007. DOI: 10.1175/1520-0477(1970)051\textless0809:{PROTBS\textgreater2}.0.{CO};2. URL: http://journals.ametsoc.org/doi/abs/10.1175/1520-0477%5C%281970%5C%29051%5C%%7B3C0809%5C%7D%%7B3APROTBS%5C%7D%%7B3E2%7D.0.%7BCO%5C%7D%%7B3B2%7D (visited on 10/01/2020).

Jacob, Marek, Felix Ament, Manuel Gutleben, Heike Konow, Mario Mech, Martin Wirth, and Susanne Crewell (June 2019). "Investigating the liquid water path over the tropical Atlantic with synergistic airborne measurements". *Atmospheric measurement techniques* 12.6, pp. 3237–3254. ISSN: 1867-8548. DOI: 10.5194/amt-12-3237-2019. URL: https://www.atmos-meas-tech.net/12/3237/2019/ (visited on 12/03/2019).

Jacob, Marek, Pavlos Kollias, Felix Ament, Vera Schemann, and Susanne Crewell (Mar. 2020). "Multi-layer Cloud Conditions in Trade Wind Shallow Cumulus – Confronting Models with Airborne Observations". DOI: 10.5194/gmd-2020-14. URL: https://www.geosci-model-dev-discuss.net/gmd-2020-14/ (visited on 07/05/2020).

Jansson, Fredrik, Wouter Edeling, Jisk Attema, and Daan Crommelin (May 2021). "Assessing uncertainties from physical parameters and modelling choices in an atmospheric large eddy simulation model." *Philosophical Transactions. Series A, Mathematical, Physical, and Engineering Sciences* 379.2197, p. 20200073. DOI: 10.1098/rsta.2020.0073. URL: http://dx.doi.org/10.1098/rsta.2020.0073 (visited on 06/07/2021).

Johnson, D. E., W-K. Tao, J. Simpson, and C-H. Sui (2002). "A Study of the Response of Deep Tropical Clouds to Large-Scale Thermodynamic Forcings. Part I: Modeling Strategies and Simulations of TOGA COARE Convective Systems". *Journal of the Atmospheric Sciences* 59.24, pp. 3492–3518. DOI: 10.1175/1520-0469(2002)059<3492:ASOTRO>2.0.CO;2. URL: https://journals.ametsoc.org/view/journals/atsc/59/24/1520-0469_2002_059_3492_asotro_2.0.co_2.xml.

Klein, Stephen A. (Aug. 1997). "Synoptic Variability of Low-Cloud Properties and Meteorological Parameters in the Subtropical Trade Wind Boundary Layer". *Journal of Climate* 10, pp. 2018–2039. URL: https://journals.ametsoc.org/doi/pdf/10.1175/1520-044

2%5C%281997%5C%29010%5C%%7B3C2018%5C%7D%%7B3ASVOLCP%5C%7D%%7B3E2%7D.0.%7BCO%5C%7D%%7B3B2%7D (visited on 06/06/2020).

Klein, Stephen A., Alex Hall, Joel R. Norris, and Robert Pincus (Nov. 2017). "Low-Cloud Feedbacks from Cloud-Controlling Factors: A Review". *Surveys in Geophysics* 38.6, pp. 1307–1329. ISSN: 0169-3298. DOI: 10.1007/s10712-017-9433-3. URL: http://link.springer.com/10.1007/s10712-017-9433-3 (visited on 12/03/2019).

Klein, Stephen A. and Dennis L. Hartmann (Aug. 1993). "The seasonal cycle of low stratiform clouds". *Journal of climate* 6.8, pp. 1587–1606. ISSN: 0894-8755. DOI: 10.1175/1520-0442(1993)006\textless1587:{TSCOLS\textgreater2}.0.{CO};2. URL: http://journals.ametsoc.org/doi/abs/10.1175/1520-0442%5C%281993%5C%2900 6%5C%%7B3C1587%5C%7D%%7B3ATSCOLS%5C%7D%%7B3E2%7D.0.%7BCO%5C%7D%%7B3B2%7D (visited on 12/03/2019).

Klein, Stephen A., Dennis L. Hartmann, and Joel R. Norris (1995). "On the Relationships among Low-Cloud Structure, Sea Surface Temperature, and Atmospheric Circulation in the Summertime Northeast Pacific". *Journal of Climate* 8.May1995. (Visited on 12/03/2019).

Knapp, Kenneth R. (2017). *Gridded Satellite GOES Coverage Data (GridSat-GOES) Western Hemisphere v01. NOAA National Centers for Environmental Information. doi:10.7289/V5HM56GM*. SOFTWARE.COMPUTER_SOFTWARE. (Visited on 12/03/2019).

Konow, Heike, Florian Ewald, Geet George, Marek Jacob, Marcus Klingebiel, Tobias Kölling, et al. (2021). "EUREC^{4}A's HALO". to be submitted.

Konow, Heike, Marek Jacob, Felix Ament, Susanne Crewell, Florian Ewald, Martin Hagen, Lutz Hirsch, Friedhelm Jansen, Mario Mech, and Bjorn Stevens (July 2019). "A unified data set of airborne cloud remote sensing using the HALO Microwave Package (HAMP)". *Earth System Science Data* 11.2, pp. 921–934. ISSN: 1866-3516. DOI: 10.5194/essd-11-921-2019. URL: https://www.earth-syst-sci-data.net/11/921/2019/ (visited on 12/03/2019).

Lenschow, Donald H., Paul B. Krummel, and Steven T. Siems (Oct. 1999). "Measuring Entrainment, Divergence, and Vorticity on the Mesoscale from Aircraft". *Journal of Atmospheric and Oceanic Technology* 16.10, pp. 1384–1400. ISSN: 0739-0572. DOI: 10.1175/1520-0426(1999)016\textless1384:{MEDAVO\textgreater2}.0.{CO};2.

Lenschow, Donald H., Verica Savic-Jovcic, and Bjorn Stevens (Dec. 2007). "Divergence and Vorticity from Aircraft Air Motion Measurements". *Journal of Atmospheric and Oceanic Technology* 24.12, pp. 2062–2072. ISSN: 0739-0572. DOI: 10.1175/{2007JTECHA940}.1.

Li, Xiang-Yu, Hailong Wang, Jingyi Chen, Satoshi Endo, Geet George, Seethala Cairns Brianand Chellappan, et al. (2021). "Large-eddy simulations of marine boundary-layer clouds associated with cold air outbreaks during the ACTIVATE campaign– part 1: Case setup and sensitivities to large-scale forcings". *Journal of the Atmospheric Sciences*. submitted.

Lorenz, Edward N (1967). *The nature and theory of the general circulation of the atmosphere*. Vol. 218. World Meteorological Organization Geneva.

Malkus, Joanne Starr (1958). *On the structure of the trade wind moist layer*. Cambridge, MA: Massachusetts Institute of Technology and Woods Hole Oceanographic Institution. DOI: 10.1575/1912/1065.

Mapes, Brian E., Eui Seok Chung, Walter M. Hannah, Hirohiko Masunaga, Anthony J. Wimmers, and Christopher S. Velden (Jan. 2018). "The meandering margin of the meteorological moist tropics". *Geophysical Research Letters* 45.2, pp. 1177–1184. ISSN:

00948276. DOI: 10.1002/{2017GL076440}. URL: http://doi.wiley.com/10.1002/%7B2017GL076440%7D (visited on 12/03/2019).

Martin, C. and I. Suhr (2021). *NCAR/EOL Atmospheric Sounding Processing ENvironment (ASPEN) software. Version 3.4.3*. URL: https://www.eol.ucar.edu/content/aspen (visited on 03/09/2021).

Mauger, Guillaume S. and Joel R. Norris (June 2010). "Assessing the impact of meteorological history on subtropical cloud fraction". *Journal of climate* 23.11, pp. 2926–2940. ISSN: 0894-8755. DOI: 10.1175/{2010JCLI3272}.1. URL: http://journals.ametsoc.org/doi/abs/10.1175/%7B2010JCLI3272%7D.1 (visited on 12/03/2019).

McFarlane, Sally A., James H. Mather, and Thomas P. Ackerman (2007). "Analysis of tropical radiative heating profiles: A comparison of models and observations". *Journal of Geophysical Research: Atmospheres* 112.D14. DOI: https://doi.org/10.1029/2006JD008290. eprint: https://agupubs.onlinelibrary.wiley.com/doi/pdf/10.1029/2006JD008290. URL: https://agupubs.onlinelibrary.wiley.com/doi/abs/10.1029/2006JD008290.

Mech, M., E. Orlandi, S. Crewell, F. Ament, L. Hirsch, M. Hagen, G. Peters, and B. Stevens (Dec. 2014). "HAMP – the microwave package on the High Altitude and LOng range research aircraft (HALO)". *Atmospheric measurement techniques* 7.12, pp. 4539–4553. ISSN: 1867-8548. DOI: 10.5194/amt-7-4539-2014. URL: https://www.atmos-meas-tech.net/7/4539/2014/ (visited on 06/08/2020).

Medeiros, Brian and Bjorn Stevens (Jan. 2009). "Revealing differences in GCM representations of low clouds". *Climate dynamics* 36.1-2, pp. 385–399. ISSN: 0930-7575. DOI: 10.1007/s00382-009-0694-5. URL: http://link.springer.com/10.1007/s00382-009-0694-5 (visited on 07/04/2020).

Myers, Timothy A. and Joel R. Norris (Oct. 2013). "Observational evidence that enhanced subsidence reduces subtropical marine boundary layer cloudiness". *Journal of climate* 26.19, pp. 7507–7524. ISSN: 0894-8755. DOI: 10.1175/{JCLI}-D-12-00736.1. URL: http://journals.ametsoc.org/doi/abs/10.1175/%7BJCLI%7D-D-12-00736.1 (visited on 12/03/2019).

Naumann, Ann Kristin, Bjorn Stevens, and Cathy Hohenegger (May 2019). "A moist conceptual model for the boundary layer structure and radiatively driven shallow circulations in the trades". *Journal of the Atmospheric Sciences* 76.5, pp. 1289–1306. ISSN: 0022-4928. DOI: 10.1175/{JAS}-D-18-0226.1. URL: http://journals.ametsoc.org/doi/10.1175/%7BJAS%7D-D-18-0226.1 (visited on 12/03/2019).

Neggers, Roel, Bjorn Stevens, and J. David. Neelin (Oct. 2006). "A simple equilibrium model for shallow-cumulus-topped mixed layers". *Theoretical and Computational Fluid Dynamics* 20.5-6, pp. 305–322. ISSN: 0935-4964. DOI: 10.1007/s00162-006-0030-1. URL: http://link.springer.com/10.1007/s00162-006-0030-1 (visited on 12/03/2019).

Nuijens, Louise, Brian Medeiros, Irina Sandu, and Maike Ahlgrimm (Dec. 2015a). "Observed and modeled patterns of covariability between low-level cloudiness and the structure of the trade-wind layer". *Journal of Advances in Modeling Earth Systems* 7.4, pp. 1741–1764. ISSN: 19422466. DOI: 10.1002/{2015MS000483}. URL: http://doi.wiley.com/10.1002/%7B2015MS000483%7D (visited on 06/07/2020).

Nuijens, Louise, Brian Medeiros, Irina Sandu, and Maike Ahlgrimm (June 2015b). "The behavior of trade-wind cloudiness in observations and models: The major cloud components and their variability". *Journal of Advances in Modeling Earth Systems* 7.2, pp. 600–616. ISSN: 19422466. DOI: 10.1002/{2014MS000390}. URL: http://doi.wiley.com/10.1002/%7B2014MS000390%7D (visited on 06/07/2020).

Nuijens, Louise, Alessandro Savazzi, Geet George, and other contributors (2021). *The momentum budget and wind stress profiles during EUREC4A*. in preparation.

Orlanski, Isidoro (May 1975). "A Rational Subdivision of Scales for Atmospheric Processes". *Bulletin of the American Meteorological Society* 56.5, pp. 527–530. URL: https://www.jstor.org/stable/26216020?seq=1%5C#metadata%5C_info%5C_tab%5C_contents (visited on 07/01/2020).

Pincus, R., C. W. Fairall, A. Bailey, H. Chen, P. Y. Chuang, G. de Boer, et al. (2021). "Observations from the NOAA P-3 aircraft during ATOMIC". *Earth System Science Data Discussions*, pp. 1–25. DOI: 10.5194/essd-2021-11.

Planck, M (Sept. 1949). "The meaning and limits of exact science." *Science* 110.2857, pp. 319–327. DOI: 10.1126/science.110.2857.319. URL: http://dx.doi.org/10.1126/science.110.2857.319 (visited on 05/26/2021).

Qu, Xin, Alex Hall, Stephen A. Klein, and Anthony M. DeAngelis (Sept. 2015). "Positive tropical marine low-cloud cover feedback inferred from cloud-controlling factors". *Geophysical Research Letters* 42.18, pp. 7767–7775. ISSN: 00948276. DOI: 10.1002/{2015GL065627}. URL: http://doi.wiley.com/10.1002/%7B2015GL065627%7D (visited on 12/03/2019).

Romps, David M. (2012). "Weak Pressure Gradient Approximation and Its Analytical Solutions". *Journal of the Atmospheric Sciences* 69.9, pp. 2835–2845. DOI: 10.1175/JAS-D-11-0336.1. URL: https://journals.ametsoc.org/view/journals/atsc/69/9/jas-d-11-0336.1.xml.

Sakradzija, Mirjana and Marcus Klingebiel (Jan. 2020). "Comparing ground-based observations and a large-eddy simulation of shallow cumuli by isolating the main controlling factors of the mass flux distribution". *Quarterly journal of the Royal Meteorological Society. Royal Meteorological Society (Great Britain)* 146.726, pp. 254–266. ISSN: 0035-9009. DOI: 10.1002/qj.3671. URL: https://onlinelibrary.wiley.com/doi/abs/10.1002/qj.3671 (visited on 12/03/2019).

Savazzi, Alessandro, Irina Sandu, Lousie Nuijens, and Geet George (2021). *IFS wind bias in the lower troposphere during the EUREC4A field campaign*. in preparation.

Schulz, Hauke, Ryan M Eastman, and Bjorn Stevens (2021). "Characterization and Evolution of Organized Shallow Convection in the Trades". *Earth and Space Science Open Archive*, p. 34. DOI: 10.1002/essoar.10505836.1. URL: https://doi.org/10.1002/essoar.10505836.1.

Schulz, Hauke and Bjorn Stevens (Oct. 2018). "Observing the tropical atmosphere in moisture space". *Journal of the Atmospheric Sciences* 75.10, pp. 3313–3330. ISSN: 0022-4928. DOI: 10.1175/{JAS}-D-17-0375.1. URL: http://journals.ametsoc.org/doi/10.1175/%7BJAS%7D-D-17-0375.1 (visited on 12/03/2019).

Siebesma, A. Pier, Christopher S. Bretherton, Andrew Brown, Andreas Chlond, Joan Cuxart, Peter G. Duynkerke, et al. (May 2003). "A large eddy simulation intercomparison study of shallow cumulus convection". *Journal of the Atmospheric Sciences* 60.10, pp. 1201–1219. ISSN: 0022-4928. DOI: 10.1175/1520-0469(2003)60\textless1201:{ALESIS\textgreater2}.0.{CO};2. URL: http://journals.ametsoc.org/doi/abs/10.1175/1520-0469%5C%282003%5C%2960%5C%%7B%7B1201%5C%7D%%7B%7BAALESIS%5C%7D%%7B%7BE2%7D.0.%7BCO%5C%7D%%7B%7BB2%7D (visited on 02/25/2021).

Simpson, Joanne (1976). "The GATE aircraft program: A personal view". *Bulletin of the American Meteorological Society* 57.1, pp. 27–30.

Slingo, J. M. (1987). "The development and verification of a cloud prediction scheme for the ECMWF model". *Quarterly Journal of the Royal Meteorological Society* 113.477, pp. 899–

927. ISSN: 00359009. DOI: 10.1002/qj.49711347710. URL: http://doi.wiley.com/10.1002/qj.49711347710 (visited on 12/03/2019).

Slingo, Julia M. (Oct. 1980). "A cloud parametrization scheme derived from GATE data for use with a numerical model". *Quarterly Journal of the Royal Meteorological Society* 106.450, pp. 747–770. ISSN: 00359009. DOI: 10.1002/qj.49710645008. URL: http://doi.wiley.com/10.1002/qj.49710645008 (visited on 12/03/2019).

Sobel, Adam H., Johan Nilsson, and Lorenzo M. Polvani (2001). "The Weak Temperature Gradient Approximation and Balanced Tropical Moisture Waves". *Journal of the Atmospheric Sciences* 58.23, pp. 3650–3665. DOI: 10.1175/1520-0469(2001)058<3650:TWTGAA>2.0.CO;2. URL: https://journals.ametsoc.org/view/journals/atsc/58/23/1520-0469_2001_058_3650_twtgaa_2.0.co_2.xml.

Sobel, Adam H and Christopher S Bretherton (2000). "Modeling tropical precipitation in a single column". *Journal of climate* 13.24, pp. 4378–4392.

Sommeria, G. and J. W. Deardorff (Feb. 1977). "Subgrid-Scale Condensation in Models of Nonprecipitating Clouds". *Journal of the Atmospheric Sciences* 34.2, pp. 344–355. ISSN: 0022-4928. DOI: 10.1175/1520-0469(1977)034\textless0344:{\SSCIMO\textgreater2}.0.{CO};2. URL: http://journals.ametsoc.org/doi/abs/10.1175/1520-0469%5C%281977%5C%29034%5C%%7B3C0344%5C%7D%%7B3A%5CSSCIMO%5C%7D%%7B3E2%7D.0.%7BCO%5C%7D%%7B3B2%7D (visited on 10/13/2020).

Stephan, C. C. and A. Mariaccia (2021). "The signature of the tropospheric gravity wave background in observed mesoscale motion". *Weather and Climate Dynamics* 2.2, pp. 359–372. DOI: 10.5194/wcd-2-359-2021. URL: https://wcd.copernicus.org/articles/2/359/2021/.

Stephan, Claudia Christine, Sabrina Schnitt, Hauke Schulz, Hugo Bellenger, Simon P. de Szoeke, Claudia Acquistapace, et al. (Aug. 2020). "Ship- and island-based atmospheric soundings from the 2020 EUREC4A field campaign". *Earth System Science Data Discussions*. DOI: 10.5194/essd-2020-174.

Stevens, B., S. Bony, D. Farrell, F. Ament, A. Blyth, C. Fairall, et al. (2021). "EUREC^{4}A". *Earth System Science Data Discussions*, pp. 1–78. DOI: 10.5194/essd-2021-18.

Stevens, Bjorn, Felix Ament, Sandrine Bony, Susanne Crewell, Florian Ewald, Silke Gross, et al. (Jan. 2019a). "A high-altitude long-range aircraft configured as a cloud observatory–the NARVAL expeditions". *Bulletin of the American Meteorological Society*. ISSN: 0003-0007. DOI: 10.1175/{BAMS}-D-18-0198.1. URL: http://journals.ametsoc.org/doi/10.1175/%7BBAMS%7D-D-18-0198.1 (visited on 12/03/2019).

Stevens, Bjorn, Anton Beljaars, Simona Bordoni, Christopher Holloway, Martin Köhler, Steven Krueger, Verica Savic-Jovcic, and Yunyan Zhang (Mar. 2007). "On the structure of the lower troposphere in the summertime stratocumulus regime of the northeast pacific". *Monthly Weather Review* 135.3, pp. 985–1005. ISSN: 0027-0644. DOI: 10.1175/{MWR3427}.1. URL: http://journals.ametsoc.org/doi/abs/10.1175/%7BMWR3427%7D.1 (visited on 12/03/2019).

Stevens, Bjorn and Sandrine Bony (2013). "Water in the atmosphere". *Physics today* 66.6, p. 29. ISSN: 00319228. DOI: 10.1063/{PT}.3.2009. URL: http://scitation.aip.org/content/aip/magazine/physicstoday/article/66/6/10.1063/%7BPT%7D.3.2009 (visited on 06/06/2020).

Stevens, Bjorn, Sandrine Bony, Hélène Brogniez, Laureline Hentgen, Cathy Hohenegger, Christoph Kiemle, et al. (Nov. 2019b). "Sugar, gravel, fish and flowers: Mesoscale cloud patterns in the trade winds". *Quarterly journal of the Royal Meteorological Society. Royal Meteorological Society (Great Britain)*. ISSN: 0035-9009. DOI: 10.1002/qj.3662. URL: https://onlinelibrary.wiley.com/doi/abs/10.1002/qj.3662 (visited on 10/13/2020).

Stevens, Bjorn and Jean-Louis Brenguier (2009). *Cloud-controlling factors: low clouds*. MIT Press. ISBN: 978-0-262-01287-4. URL: https://pure.mpg.de/pubman/faces/%7BViewItemOverviewPage%7D.jsp?%7BitemId%7D=item%5C_994033 (visited on 06/04/2020).

Stevens, Bjorn, Hélène Brogniez, Christoph Kiemle, Jean-Lionel Lacour, Cyril Crevoisier, and Johannes Kiliani (July 2017). "Structure and dynamical influence of water vapor in the lower tropical troposphere". *Surveys in Geophysics*, pp. 1–27. ISSN: 0169-3298. DOI: 10.1007/s10712-017-9420-8.

Stevens, Bjorn, David Farrell, Lutz Hirsch, Friedhelm Jansen, Louise Nuijens, Ilya Serikov, et al. (May 2016). "The barbados cloud observatory: anchoring investigations of clouds and circulation on the edge of the ITCZ". *Bulletin of the American Meteorological Society* 97.5, pp. 787–801. ISSN: 0003-0007. DOI: 10.1175/{BAMS}-D-14-00247.1.

Stratum, Bart J. H. van, Jordi Vilá-Guerau de Arellano, Chiel C. van Heerwaarden, and Huug G. Ouwersloot (Mar. 2014). "Subcloud-Layer Feedbacks Driven by the Mass Flux of Shallow Cumulus Convection over Land". *Journal of the Atmospheric Sciences* 71.3, pp. 881–895. ISSN: 0022-4928. DOI: 10.1175/{JAS}-D-13-0192.1. URL: http://journals.ametsoc.org/doi/abs/10.1175/%7BJAS%7D-D-13-0192.1 (visited on 12/03/2019).

Szoeke, Simon P. de, Kathryn L. Verlinden, Sandra E. Yuter, and David B. Mechem (Sept. 2016). "The time scales of variability of marine low clouds". *Journal of climate* 29.18, pp. 6463–6481. ISSN: 0894-8755. DOI: 10.1175/{JCLI}-D-15-0460.1. URL: http://journals.ametsoc.org/doi/10.1175/%7BJCLI%7D-D-15-0460.1 (visited on 02/28/2021).

Touzé-Peiffer, Ludovic, Raphaela Vogel, and Nicolas Rochetin (2021). *Detecting cold pools from soundings during EUREC4A*. arXiv: 2104.09146 [physics.ao-ph].

UCAR/NCAR, Earth Observing Laboratory (1993). "NCAR Airborne Vertical Atmospheric Profiling System (AVAPS)". *UCAR/NCAR - Earth Observing Laboratory*. DOI: 10.5065/d66w9848.

Vaisala (2020a). *Vaisala Radiosonde RD41 datasheet in English, B211706EN-B*. Tech. rep. Vaisala. URL: https://www.vaisala.com/sites/default/files/documents/%7BRD41%7D-Datasheet-%7BB211706EN%7D.pdf (visited on 01/04/2021).

Vaisala (2020b). *Vaisala Radiosonde RS41G datasheet in English, B211321EN-K*. Tech. rep. Vaisala. URL: https://www.vaisala.com/sites/default/files/documents/%7BRS41%7D-%7BSG%7D-Datasheet-%7BB211321EN%7D.pdf (visited on 01/05/2021).

VanZanten, Margreet C, Bjorn Stevens, Louise Nuijens, A Pier Siebesma, AS Ackerman, F Burnet, A Cheng, F Couvreux, H Jiang, M Khairoutdinov, et al. (2011). "Controls on precipitation and cloudiness in simulations of trade-wind cumulus as observed during RICO". *Journal of Advances in Modeling Earth Systems* 3.2.

Vial, Jessica, Sandrine Bony, Jean-Louis Dufresne, and Romain Roehrig (Dec. 2016). "Coupling between lower-tropospheric convective mixing and low-level clouds: Physical mechanisms and dependence on convection scheme." *Journal of Advances in Modeling Earth Systems* 8.4, pp. 1892–1911. DOI: 10.1002/{2016MS000740}. URL: http://dx.doi.org/10.1002/%7B2016MS000740%7D (visited on 12/03/2019).

Vial, Jessica, Sandrine Bony, Bjorn Stevens, and Raphaela Vogel (July 2017). "Mechanisms and Model Diversity of Trade-Wind Shallow Cumulus Cloud Feedbacks: A Review." *Surveys in Geophysics* 38.6, pp. 1331–1353. ISSN: 0169-3298. DOI: 10.1007/s10712-017-9418-2. URL: http://link.springer.com/10.1007/s10712-017-9418-2 (visited on 12/03/2019).

Vogel, Raphaela, Sandrine Bony, and Bjorn Stevens (May 2020). "Estimating the Shallow Convective Mass Flux from the Subcloud-Layer Mass Budget". *Journal of the Atmospheric Sciences* 77.5, pp. 1559–1574. ISSN: 0022-4928. DOI: 10.1175/{JAS}-D-19-0135.1.

URL: http://journals.ametsoc.org/doi/10.1175/%7BJAS%7D-D-19-0135.1 (visited on 06/24/2020).

Wang, Junhong (June), Kate Young, Terry Hock, Dean Lauritsen, Dalton Behringer, Michael Black, et al. (June 2015). "A Long-Term, High-Quality, High-Vertical-Resolution GPS Dropsonde Dataset for Hurricane and Other Studies". *Bulletin of the American Meteorological Society* 96.6, pp. 961–973. ISSN: 0003-0007. DOI: 10.1175/{BAMS}-D-13-00203.1. URL: http://journals.ametsoc.org/doi/10.1175/%7BBAMS%7D-D-13-00203.1 (visited on 06/30/2020).

Webb, Mark J, Adrian P Lock, Christopher S Bretherton, Sandrine Bony, Jason N S Cole, Abderrahmane Idelkadi, et al. (Nov. 2015). "The impact of parametrized convection on cloud feedback." *Philosophical Transactions. Series A, Mathematical, Physical, and Engineering Sciences* 373.2054. DOI: 10.1098/rsta.2014.0414. URL: http://dx.doi.org/10.1098/rsta.2014.0414 (visited on 07/06/2020).

Wengel, Christian, Florian Ziemen, Helmuth Haak, Peter Korn, Monika Esch, Jiawei Bao, et al. (2021). *DYAMOND Winter Analysis*. in preparation.

Wirth, M., A. Fix, P. Mahnke, H. Schwarzer, F. Schrandt, and G. Ehret (July 2009). "The airborne multi-wavelength water vapor differential absorption lidar WALES: system design and performance". *Applied Physics B* 96.1, pp. 201–213. ISSN: 0946-2171. DOI: 10.1007/s00340-009-3365-7. URL: http://link.springer.com/10.1007/s00340-009-3365-7 (visited on 07/02/2020).

Yanai, Michio, Steven Esbensen, and Jan-Hwa Chu (May 1973). "Determination of Bulk Properties of Tropical Cloud Clusters from Large-Scale Heat and Moisture Budgets". *Journal of the Atmospheric Sciences* 30.4, pp. 611–627. ISSN: 0022-4928. DOI: 10.1175/1520-0469(1973)030\textless0611:{DOBPOT\textgreater2}.0.{CO};2. URL: http://journals.ametsoc.org/doi/abs/10.1175/1520-0469%5C%281973%5C%29030%5C%%7B3C0611%5C%7D%%7B3ADOBPOT%5C%7D%%7B3E2%7D.0.%7BCO%5C%7D%%7B3B2%7D (visited on 07/17/2013).

Zelinka, Mark D., Timothy A. Myers, Daniel T. McCoy, Stephen Po-Chedley, Peter M. Caldwell, Paulo Ceppi, Stephen A. Klein, and Karl E. Taylor (Jan. 2020). "Causes of higher climate sensitivity in CMIP6 models". *Geophysical Research Letters*. ISSN: 0094-8276. DOI: 10.1029/{2019GL085782}. URL: https://onlinelibrary.wiley.com/doi/abs/10.1029/%7B2019GL085782%7D (visited on 06/05/2020).

Zheng, Youtong (May 2019). "Theoretical understanding of the linear relationship between convective updrafts and cloud-base height for shallow cumulus clouds. Part I: Maritime conditions". *Journal of the Atmospheric Sciences*. ISSN: 0022-4928. DOI: 10.1175/{JAS}-D-18-0323.1. URL: http://journals.ametsoc.org/doi/10.1175/%7BJAS%7D-D-18-0323.1 (visited on 03/04/2021).

Zheng, Youtong and Daniel Rosenfeld (Aug. 2015). "Linear relation between convective cloud base height and updrafts and application to satellite retrievals". *Geophysical Research Letters* 42.15, pp. 6485–6491. ISSN: 00948276. DOI: 10.1002/{2015GL064809}. URL: http://doi.wiley.com/10.1002/%7B2015GL064809%7D (visited on 03/04/2021).

VERSICHERUNG AN EIDES STATT

Hiermit erkläre ich an Eides statt, dass ich die vorliegende Dissertationsschrift selbst verfasst und keine anderen als die angegebenen Quellen und Hilfsmittel benutzt habe

Hamburg, June 2021

Geet George